SYNTHESIS, CHARACTERIZATION AND APPLICATION OF TUNGSTEN TRIOXIDE-MAGNESIUM OXIDE NANOCOMPOSITE FOR THE TREATMENT OF LOCAL DYEING WASTEWATER

BY

UKO, Christopher Agida
MENG/SEET/2017/6720

A THESIS SUBMITTED TO THE POSTGRADUATE SCHOOL FEDERAL UNIVERSITY OF TECHNOLOGY, MINNA, NIGER STATE, NIGERIA
IN PARTIAL FULFILMENT OF THE REQUIREMENT FOR THE AWARD OF THE MASTERS DEGREE IN CHEMICAL ENGINEERING

MAY, 2021

ABSTRACT

This study focused on the synthesis, characterization and application of tungsten trioxide/magnesium oxide (MgO/WO_3) nanocomposite for the treatment of local dyeing wastewater. The individual nanoparticles (MgO and WO_3) were prepared by green process and their composites, formulated by mixing the nanoparticles at different ratios using wet impregnation method. The adsorptive capacity of MgO, WO_3 and MgO/WO_3 nanoadsorbents were evaluated for the removal of selected heavy metals and other water quality indicator parameters from dyeing wastewater via batch adsorption mode. The synthesised nanoparticles and their nanocomposites were characterised using X-ray diffraction (XRD), High resolution electron microscopy (HRSEM), High resolution transmission electron microscopy (HRTEM), energy dispersive spectroscopy (EDX), selected area electron diffraction (SAED) and Brunauer-Emette-Teller (BET) for their phase identification and crystallite size, morphologies, particle size distribution and dispersion, elemental composition, crystallinity and specific surface area, respectively. The XRD analysis of pure WO_3 and MgO nanoparticles confirmed the formation of monoclinic phase and face centered cubic phase. The variations in the mixing ratios of MgO and WO_3 nanoparticles showed the existence of chemical reaction between the nanoparticles to form magnesium tungstate ($MgWO_4$). The EDX results showed that the synthesised nanocomposites composed of O, Mg and W which confirmed the pure formations of oxide of Mg and W. The specific surface areas of the MgO/WO_3 nanocomposites at 1:1, 1:2, 2:1, 4:1 and 1:4 were 29.97, 45.28, 60.42, 104.16 and 93.58 m^2/g, respectively which revealed that composite with highest surface area is MgO/WO_3 (4:1) which is greater than WO_3 alone with surface area (22.49 m^2/g). The addition of MgO nanoparticles enhanced the surface area of WO_3 nanoparticles. The adsorption studies at different contact times, adsorbent dosages and temperatures showed that adsorbent dosage and temperature are the most influential factors. The maximum removal efficiency of Cu(II), Fe(II) and Cr(VI) at optimum conditions are 98.1 %, 100 % and 100 %, respectively. The adsorption isotherms were evaluated using Langmuir, Freundlich and Elovich models and the experimental data followed Langmuir model and the adsorption kinetic conformed to the pseudo-second-order. Thermodynamic study demonstrated that the adsorption process is endothermic and spontaneous in nature. The regeneration study of the MgO, WO_3 and MgO/WO_3 nanoadsorbents showed that the percentage adsorption of Fe(II), Cu(II) and Cr(III) ions were high even after 4, 4 and 5 cycles, respectively. The study showed that, among the nanoadsorbents, MgO/WO_3 (4:1) with highest surface area and adsorption efficiency was found most suitable for the treatment of dyeing wastewater.

TABLE OF CONTENTS

LIST OF TABLES

LIST OF FIGURES

LIST OF PLATES

GLOSSARY

B_T	Tempkin isotherm constant
C_e	Equilibrium concentration (mg/L)
C_i	Initial concentration of adsorbate (mg/L),
C_s	Adsorbate monolayer saturation concentration (mg/L)
k_1	Rate constant for the pseudo-first-order sorption (min^{-1})
k_2	Rate constant of the pseudo-second-order kinetic equation ($g/mgmin^{-1}$)
K_d	Distribution coefficient
K_F	Freundlich isotherm constant (mg/g)
K_{id}	Rate constant for intraparticle diffusion
q_e	Amount of adsorbate in the adsorbent at equilibrium (mg/g)
Q_m	Maximum monolayer adsorption capacity (mg/g)
q_t	Quantity of adsorbate adsorbed at time t (mg/g)
ΔG	Change in Gibbs free energy (kJ/mol)
ΔH	Change in enthalpy (kJ/mol)
ΔS	Change in entropy (J/molK)
M	Mass of adsorbent (g)
n	Adsorption intensity
R	Universal gas constant (8.314 J/molK)
T	Temperature (K)
t	Time (min)
V	Volume of solution (L)

CHAPTER ONE

1.0 INTRODUCTION

1.1 Background to the Study

The environment is under stress due to the rapid development of industrialization and urbanization. One of the global problems is environmental pollution linked to the release of untreated wastewater from industries; thereby making water bodies unhygienic for the human race (Weerasooriya *et al.,* 2021). The rapid population growth and urbanization keep more pressure on the water resources and clean water demand-supply for domestic, agricultural and industrial activities. According to Yang *et al.* (2019), water is known as an essential natural resource which is paramount to human survival and their development but its consumption rate continues to intensify. The need for improvements in safe drinking water worldwide has been a paramount health concern.

A report by the World Health Organization (2020) proclaimed that 2.6 billion people have gained access to improved drinking water since 1990, but regions like the Caucasus and Central Asia, North Africa, Oceanic and sub-Sahara Africa did not meet the drinking water target. For instance, in Nigeria alone, approximately 60 million and 80 million Nigerians still lack access to safe water and sanitation facilities (Yaya *et al*., 2018). The limited clean water quality are continuously compromised due to release of toxic substances from industries. In fact, the release of toxic pollutants from dyeing industries in particular into the environment is worrisome because about 80 % of indigenous people lack the required treatment skills and as such discharge their wastewater into the environment without any form of pre-treatment (Durotoye *et al.,* 2018).

The local dyeing wastewater is highly coloured and contained several organic and inorganic pollutants especially heavy metals (Abdullah *et al.,* 2021). The number of indigenous dyeing cottage industries continue to increase due to the total collapse of the

textile industries in the country. Local dyeing involves mixing of plain fabric with different organic dyes for a predetermined period of time. As at today, the market for dyes and their acceptance among the citizens continue to increase. Water contaminants/pollutants, especially potential toxic heavy metal pollution originating from wastewater have become a global trending environmental problem. These toxic metals are released into water bodies mainly via other sources like electroplating, agriculture, mining, dye and tanning, metallurgy wastes among others (Mishra *et al.,* 2019). These heavy metals even at low concentrations pose severe threats to human and other organisms, causing damage to kidney and liver, brain and haematopoietic system which leads to nausea, anemia, hepatitis, gastric ulcer, dermatitis, respiratory disorder, kidney and liver dysfunction (Stidworthy and Denk, 2018). In view of the toxic effect of wastewater on fauna and flora, it is imperative that the wastewater is treated before eventual release into the environment.

Over the past decades, numerous detoxification strategies for the removal of heavy metals and dyestuff from wastewater which include flotation and sedimentation, ion exchange, chemical precipitation, separation membrane, electro-dialysis, photodegradation and adsorption has been used (Maharana *et al.,* 2021). Among these aforementioned methods, adsorption is an extensive and widely used technique owing to its simple operation, high efficacy, convenience and cost-effectiveness (Karimi-Maleh *et al.,* 2020). Several studies have demonstrated the efficacy of nanomaterials in the adsorption of contaminants from wastewater. The application of nanoparticles with a size smaller than 100 nm have received enormous attention due to their unique properties (physical, chemical and mechanical) over bulk materials. Several materials such as zinc oxide, titanium oxide, nickel oxide, cadmium sulphide, cerium oxide, iron oxide and copper oxide have been used as nanoadsorbents (Ismail *et al.,* 2019). These nanomaterials have shown some

properties which include high reactivity, low-cost of production, high surface area, and high adsorption capacity. As such, nanomaterials serve as good adsorbents material. For example, WO_3 and MgO nanoparticles are non-toxic, have high large surface area and high photocatalytic/adsorption activity (Yemmireddy and Hung, 2017). These nanoparticles are synthesised using physical and chemical methods such as co-precipitation, hydrothermal, vapour deposition, solvothermal, microwave assisted reduction, photodeposition and photoreduction, chemical vapour deposition, spray pyrolysis, sol-gel and so on. The physical and chemical methods have certain shortcomings such as complex synthesis procedure, long synthesis time, generation of toxic byproduct among others. (Thiagarajan *et al.,* 2017).

Nowadays, research attention have shifted to the synthesis of metal oxide nanoparticles using green chemistry protocol due to its simplicity, cost effectiveness and environmental friendliness. Green synthesis or biosynthesis involves replacement of toxic chemicals with plant extracts or microorganism (Salem and Fouda, 2021). Plant extracts act as a stabilizing, capping and reducing agent. For instance, Aziz and Karim (2019) synthesised MgO nanoparticles using direct precipitation for photodegradation of methylene blue and photodegradation efficiency under direct sunlight was 96.7 %. Photocatalytic activity of graphene/WO_3 for degradation of methylene blue under the irradiation light investigated by Hossain *et al.* (2018) showed that with the addition of WO_3 to graphene, there was better photocatalytic performance. This aroused the great interest in the development of nanocomposites in the environmental remediation of pollutants from wastewater. In another survey, MgO nanoparticles were immobilized on concrete for the photocatalytic degradation of diazinon and maximum pollutant removal was 99.56 % (Ahmadifard *et al.,* 2019). Magnesium oxide/carbon nitride (MgO/C_3N_4) nanocomposites were used to remove reactive orange 16 under visible light and maximum removal was 82 % (Fathi *et*

al., 2020). Chen *et al.* (2018) prepared carbon nanocomposites from a natural biomass for the adsorption of some heavy metals in dye effluent. Degradation of textile effluent using crude *Ganoderma lucidum* was used and decolourization efficiency of 87 % was obtained. Even though research efforts focused more on the photocatalytic degradation of pollutants in dyeing effluents, there is still a need to investigate the adsorptive potential of the binary nanocomposites of MgO/WO_3 for the treatment of local dyeing wastewater. Herein, the study focused on the adsorption of some heavy metals and dyestuff in a local dyeing wastewater using WO_3, MgO and MgO/WO_3.

1.2 Statement of the Problem

Indigenous dyeing wastewater is highly coloured, turbid, have odiferous smell, high Chemical Oxygen Demand (COD), Biochemical Oxygen Demand (BOD), Total Organic Carbon (TOC), Dissolved Oxygen (DO), high suspended matters and contain considerable amount of toxic heavy metals (Abdullah *et al.,* 2021). Human health and Environmental related effects due to the presence of pollutants in dye effluents caused carcinogenic and mutagenic derivatives along with the allergic reactions, skin degeneration, asthma, nausea, dysfunction of kidney and liver (Stidworthy and Denk, 2018). Heavy metals present in local dyeing wastewater affects the agriculture products and human. Aquatic systems get contaminated and the effluents discharged in that blocked the sunlight penetration to the organisms present.

Dye reduction technologies mostly employed includes membrane filtration, ozonation, coagulation, reverse osmosis, filtration, precipitation, enzymatic decomposition, active sludge and biochemical processes most of which have complex operation procedures, consume time, have high energy requirement, and expensive toxic chemicals (Thiagarajan *et al.,* 2017). WO_3 nanoparticles alone has low surface area responsible for its low

adsorptive efficiency. Similarly, conventional adsorbents possess limited active sites, small surface area and low adsorption efficiency compared to nanoadsorbents

1.3 Justification of the Study

Adsorption technology platform with nanomaterial is simple to operate with no special skills required compared to other conventional methods and have been identified as viable method of treating dyeing wastewater containing complex organic and inorganic constituents.

Green method is a simple, cost effective and ecofriendly approach for the synthesis of nanomaterials with high adsorption kinetics. The doping of WO_3 with MgO nanoparticles will help to increase surface area and sorption sites of the composite materials, hence enhance its adsorptive capacity. For these reasons, these nano-sized metal oxides are suitable materials to be used as nanoadsorbents, produce superoxide anions which have high performance for the removal of contaminants and could serve as important purifier in the water/wastewater industry. Application of MgO/WO_3 nanocomposite as nanoadsorbent remove colours, odifereous smell, lower the COD, BOD, TOC level, and heavy metals in the range of 1-100 mg/L.

1.4 Aim and Objectives of the Study

This research work aimed to synthesise and characterise tungsten oxide/magnesium oxide nanocomposite for the treatment of local dyeing effluent. The aim of the study was achieved through the following objectives:

i) Synthesis of WO_3, MgO nanoparticles by green method and MgO/WO_3 nanocomposites via wet impregnation.

ii) Characterisation of WO_3 and MgO nanoparticles, MgO/WO_3 nanocomposites to determine their surface areas, elemental composition, microstructure, morphologies, phase structures using different analytical tools.

iii) Determination of physicochemical parameters of the local dye wastewater obtained from No 23, Chawai Street, Unguwan Sanusi, Kaduna State, before and after batch adsorption process.

iv) Application of WO_3, MgO and MgO/WO_3 nanoadsorbents for the removal of selected heavy metals (Cr (VI), Fe(II), and Cu(II)) and lowering of TOC, BOD, COD from local dyeing wastewater via batch adsorption process.

v) Evaluation of experimental data using adsorption isotherms and kinetic models

vi) Regeneration study of the synthesised WO_3, MgO and MgO/WO_3 nanoadsorbents.

CHAPTER TWO

2.0 LITERATURE REVIEW

2.1 Water and Its Environment

Water is one of the basic necessity for the survival and growth of human, however, availability of safe drinking water has become a problem of global concern nowadays. According to Inyinbor *et al.* (2018), it was estimated that contaminated water killed more people yearly than the total number of people dying of all sorts of violence combined. In its World Water Development Report (2016), it was reported that more than 8 % of the total world population will live in water-scarce areas; but, by 2025, the world population is expected to reach nearly 8.1 billion and as high as 38 % of it will suffer from freshwater scarcity. Regarding this impending global water crisis, nature has highlighted in its web focus as: "more than one billion people in the world lack access to clean water, and things may get worse, if urgent steps are not taken (Reid, 2018). Over the next two decades, the average supply of water per person will drop by a third, possibly exposing millions of people to an avoidable premature death". One of the fundamental problems accounting for the reduction in the quality of drinking water is environmental pollution via different point and non-point sources. One of the most widely released substances into water bodies is liquid organic dyes.

2.2 Dye Synopsis

According to Durotoye (2018), dyes are deeply coloured soluble substances which can be applied in solutions or dispersions to fabrics, paper or gelatin layer in photographic film and leather fur to give a coloured material substantial fastness. Dyes can be classified according to their constituents, colours and applications. However, application is the most frequently used method for dyes classification. Azo dyes, anthraquinone dyes, phthalocyanine, indigoid dyes, nitroso dyes, nitro dyes and triarylmethane dyes are

classified based on their chemical structure as presented in Table 2.1. Azo, anthraquinone and triarylmethane dyes are the most important groups among these dyes. Similarly, Figure 2.1 depicts dye classification according to their ionic charges as reported by Ruan et al., (2019).

Table 2.1 Types of Dyes, Their Application and Toxicity (Ruan et al., 2019)

Dyes	*Examples*	*Application*	*Toxicity*
Acid	*Sunset yellow, methyl orange*	Wool, silk, paper, leather	Carcinogenic (benign and malignant tumors)
Cationic	Methylene blue, Rhodamine 6G	Paper, modified polyester	Carcinogenic (benign and malignant tumors)
Disperse	Disperse orange 3, Disperse red	Nylon, acrylic fibers	Allergenic (skin), carcinogenic
Direct	*Congo red, Direct red 23*	Cotton, paper, leather	Bladder cancer
Reactive	Reactive 120, Reactive 198	Cotton, wool, nylon	Dermatitis, allergic conjunctivitis
Vat	Vat orange 15, Vat orange 28	Cellulosic fibers	-

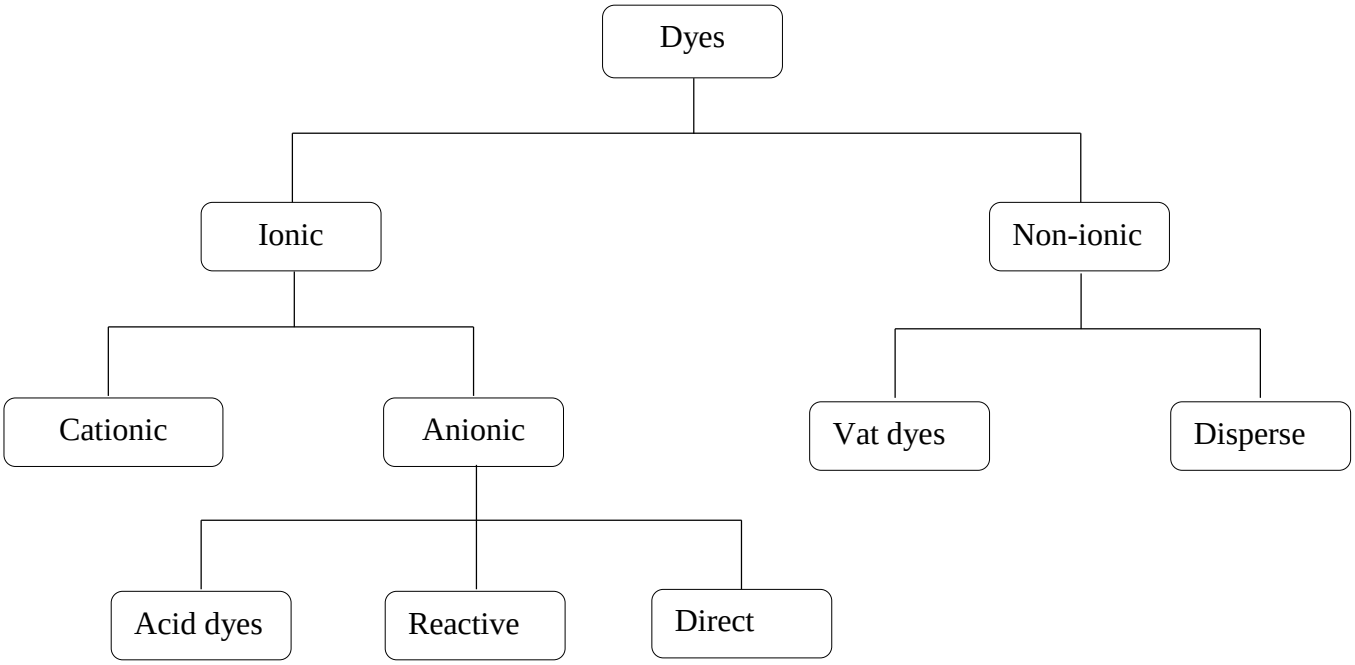

Figure 2.1: Classification of dye according to the ionic charge (Ruan et al., 2019)

2.3 Water Pollution

One of the major challenges facing the entire globe is provision of clean and affordable water that can keep up with the demands of rapidly growing population. Population growth, global climate change, and water pollution are the highest challenges that increase the scuffles faced by water supply systems (Sharma and Bhattacharya, 2017). In both developing and industrialized countries, water scarcity is exacerbated by human activities that play the greatest role in contaminating the natural water resources through the release of energy, chemicals, and other pollutants that deteriorate the water quality for other users (Edokpayi *et al.*, 2017). Also, nature itself can be one of the contamination sources such as water storm runoff, animal wastes, etc. Water pollution is classified into: (1) plant nutrients, (2) biodegradable waste, (3) heat, (4) sediment, (5) hazardous and toxic chemicals, and (6) radioactive pollutants (Ibrahim *et al.*, 2016). Thus, water pollutants include organic pollutants, pathogens, industrial discharge containing heavy metals and

different anions. These are pollutants added to the water either directly or indirectly and cannot be naturally broken down completely and they tend to change the properties of the water body (Masindi and Muedi, 2018).

2.3.1 Dyeing wastewater

Local dyeing firms as well as textile industries affect economic development worldwide, leading to unacceptable effluent, especially dyestuffs, which are difficult to degrade (Yaseen and Scholz, 2019). The classification of dye handling industries depends on the type of fabrics they produce, including cellulosic materials obtained from plants (cotton, rayon and linen), protein fabrics, which come from animals (wool, silk and mohair), and synthetic fabrics produced artificially (nylon, polyester and acrylic) (Ghaly *et al.*, 2014). Fibre production in textile factories includes dry and wet processes. The wet process uses large amount of water and releases highly contaminated wastewater. This process consists of sizing, desizing, sourcing, bleaching, mercerising, dyeing, printing and finishing techniques (Madhav *et al.,* 2018). Figure. 2.2 presents the major pollutants in the wastewater discharge from various steps, as portrayed by Holkar *et al.* (2016). The dyeing process is a paramount step in textile manufacturing. During this stage, the colour is added to the fibres, and chemicals are used to improve the adsorption process between colour and fibres. When the final product is ready after the finishing process, some of these dyes and chemicals become part of the residual dyeing effluents (Markandeya *et al.*, 2017). These dyes and chemicals, in addition to their unacceptable appearance and toxic effect after their breakdown, may contaminate the nearby soil, sediment and surface water, becoming a major global environmental pollution challenge (Yaseen *et al.,* 2019). The treatment of dyeing wastewater is necessary to protect the ecosystem and enable subsequent recycling of the treated wastewater for farming purposes or reuse (Kumar *et al.,* 2019).

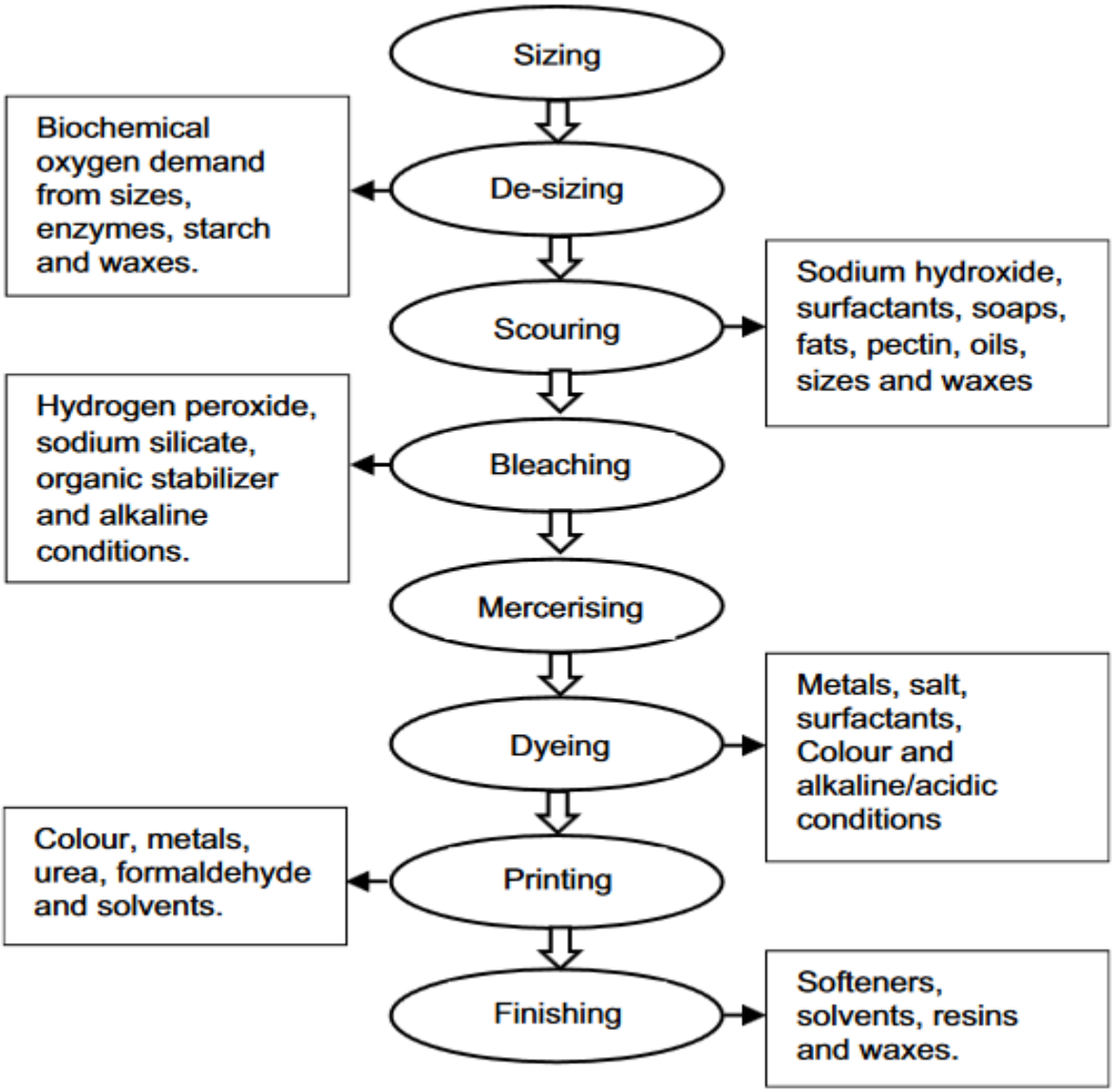

Figure 2.2: The main pollutants discharged from each step of textile wet processing (Holkar *et al.*, 2016).

2.4 Environmental and health implication of dye wastewater

The environmental issues associated with residual dye content in dyeing wastewater are always a concern for each operator that directly discharges, untreated effluent into water sources (Awwad *et al.,* 2020). Water pollution caused by industrial effluent discharges has become a worrisome phenomenon due to its impact on environmental health and safety. Textile industries and local dyeing firms contribute immensely to surface water deterioration and are categorized among the most polluting of all industrial sectors. Wastewater from dye applying industries are complex mixtures of chemicals varying in

quantity and quality (Fenta, 2014). These industries can generate both inorganic and organic waste mixed with wastewaters from the production processes, which leads to change in both biological and chemical parameters of the receiving water bodies (Ahmad *et al.,* 2019).

Globally, more than 100,000 dyes are commercially available, in which some are resistant to chemical and microbial attacks and remains stable in light and during washing (Chockalingam *et al.,* 2019). The main issue of wastewater from local dyeing industries is the increase of biochemical oxygen demand (BOD), chemical oxygen demand (COD), pH, suspended solids in water bodies (Bhatia *et al.,* 2018). The treatment of dye wastewater prior to its release into water bodies is a must as pollution traits such as solids, oils, metal complexes, high organics, complex synthetic dyes and residues from various pre-processing steps for fabric preparation and colouring have far-reaching environmental consequences (Hossain *et al.,* 2018).

2.4.1 Environmental issues

One of the most critical problems of developing countries is improper management of the vast amount of wastes generated by various anthropogenic activities. More challenging is the unsafe disposal of these wastes into the ambient environment. The key environmental issues associated with the dyeing industry are water use, treatment, and disposal of aqueous effluent (Toprak and Anis, 2017). The environmental risk is a function of environmental exposure (concentration and duration) and polluting potential (hazard characteristics or toxicity). Hence, reducing the emissions into the various environmental pathways can reduce environmental risk (Lellis, *et al.,* 2019). The wastewaters generated from different stages of dye application processes contain huge amounts of pollutants that are very harmful to the environment if released without proper treatment. The extent of environmental pollution due to dye bath water is very high. There are large numbers of

mechanical and chemical processes involved in the dyeing industry and each process has a different impact on the environment. The presence of sulphur, naphthol, vat dyes, nitrates, acetic acid, soaps, chromium compounds, heavy metals such as copper, arsenic, lead, cadmium, mercury, nickel, and cobalt, and certain auxiliary chemicals contributed to high toxicity of effluent (Sivaram *et al.,* 2019). The mill effluent is also often of high temperature and pH, both of which are extremely damaging. Also, the accumulation of colour hinders sunlight penetration, disturbed the ecosystem of the receiving water (Methneni *et al.,* 2021). In addition, when this wastewater is allowed to flow in the fields, it clogs the pores of the soil resulting in loss of soil fertility and productivity. The texture of soil gets hardened and penetration of roots is prevented (Khan and Malik, 2014). The wastewater that flows in the drains corrodes the sewerage pipes. If wastewater is allowed to flow in drains and rivers, it affects the quality of drinking water in hand pumps making it unfit for human consumption. The colour in water courses is accepted as an aesthetic problem rather than an eco-toxic hazard. Therefore, the public seems to accept the blue, green, or brown colour of rivers but a "non-natural" colour such as red and purple usually raised serious concern (Awwad *et al.,* 2020). Wastewater also leads to leakage in drains increasing their maintenance cost. Other environmental issues of equal importance are air emission, notably volatile organic compounds (VOCs), and excessive noise or odour as well as workspace safety (Methneni *et al.,* 2021). Most processes performed in dye handling mills produce atmospheric emissions.

Local dyeing mills as well as textile mills usually generate nitrogen and sulphur oxides from boilers. Other significant sources of air emissions in dyeing operations include resin finishing and drying operations, printing, dyeing, fabric preparation, and wastewater treatment plants (Mani *et al.,* 2019). Hydrocarbons are emitted from drying ovens and

from mineral oils in high-temperature drying/curing. These processes can emit formaldehyde, acids, softeners, and other volatile compounds (Khan and Malik, 2014).

2.4.2 Health problems

The direct discharge of local dyeing wastewater into water bodies like rivers amongst other pollutes the water and affects the flora and fauna. Depending on the exposure time and dye concentration, dyes can have acute and/or chronic effects on exposed organisms (Hassaan and El Nemr, 2017). Depletion of dissolved oxygen in water is the most serious effect of dyeing wastewater as dissolved oxygen is very essential for marine life. This also hinders the self-purification process of water. The dyes used in textile industries are potential health hazards as they may be converted to toxic and/or carcinogenic products under anaerobic conditions (Girish, 2019).

Many dyes are toxic to fish and mammalian life; they inhibit the growth of microorganisms and affect flora and fauna. Apart from this, several dyes and their decomposition derivatives have proved toxic to aquatic life (aquatic plants, microorganisms, fish, and mammals). They are also carcinogenic and can cause intestinal cancer and cerebral abnormalities in the fetus (Jamee and Siddique, 2019). Dyes can cause allergies such as contact dermatitis and respiratory diseases, allergic reaction in the eyes, skin irritation, and irritation to mucous membrane and the upper respiratory tract. It is assumed that, in the same way, reactive dyes can bind with $–NH_2$ and –SH groups of proteins in living organisms (Srivastava and Sofi, 2020). Additionally, fairly intensive studies have inferred that such coloured allergens may undergo chemical and biological assimilations, cause eutrophication, consume dissolved oxygen, prevent re-oxygenation in receiving streams, and have a tendency to sequester metal ions accelerating genotoxicity and microtoxicity (Welegerima, 2018). A high potential health risk is caused by adsorption of dyes and their breakdown products (toxic amines) through the

gastrointestinal tract, skin, lungs and also formation of haemoglobin adducts and disturbance of blood formation. Most dyes cause damage to DNA that can lead to the genesis of malignant tumours (Gürses *et al.,* 2016). Today, byssinosis is among one of the most significant health problems in the entire textile industry. The use of dye-stuffs and pigments may cause several adverse effects on health. Health effects may be exerted directly at the site of application (affecting the workers) and later in the life cycle (affecting the consumers) (Khattab *et al.,* 2020). Because clothing comes into prolonged contact with skin, toxic chemicals are absorbed through the skin, especially when the human body is warm and skin pores have opened to permit perspiration (Markandeya *et al.,* 2017). Once absorbed by humans, heavy metals tend to accumulate in the liver, kidney, bones, heart, and brain. The effects on health can be significant when high levels of accumulation are reached. The effect is particularly serious in children because toxic dye and/or heavy metal accumulation may negatively affect their growth and maybe their life as well (Rehman *et al.,* 2018).

2.5 Wastewater Treatment

The wastewater treatment involves physical, chemical, and biological technologies and it usually occurs in four stages: (1) preliminary, (2) primary, (3) secondary, and (4) tertiary advanced treatment (Samer, 2015). The technologies that are commonly used for water purification include coagulation and flocculation, sedimentation, dissolved air flotation, filtration, steam distillation, ion exchange, deionization, reverse osmosis and irradiation with ultraviolet light (Amrane *et al.,* 2020). Materials usually used in these technologies are sediment filters, activated carbon, coagulants, ion exchangers, ceramics, activated alumina, organic polymers, and many hybrid materials (Padmaja et al., 2014). Most of these methods employed for the removal of pollutants present in wastewater are not cost-

effective for the elimination of trace contaminants and also release secondary toxic contaminants into the environment (Rathi *et al.*, 2021).

2.5.1 Nanotechnology in water and wastewater treatment

Groundbreaking progress in the area of nanoscience and nanotechnology over the last couple of decades has motivated the scientific community to explore this highly potential area of research, where, the unique and advantageous properties of novel nanostructured materials could be exploited to deliver more efficient and sustainable solutions to the prevailing water-related problems (Wang, 2018). Nanomaterials have dimensions between 1 and 100 nm. Due to their smaller size, they contain relatively lesser number of particles which give rise to their different properties compared to the bulk materials (Jeevanandam *et al.*, 2018). Owing to their small size, nanomaterials possess high surface area, which leads to more surface dependent properties. This has been found that, due to their advantageous physicochemical properties, nanomaterials are excellent adsorbents for different water pollutants (Homaeigohar, 2020). Several nanotechnology-based pathways for wastewater treatment have been developed and most commonly used techniques are classified into following broad categories:

a) Adsorption based technology
b) Membrane-based technology
c) Anti-microbial nanomaterials based technology
d) Photocatalytic water treatment technology
e) Sensing and monitoring technology

2.5.2 Metal oxide-based Nanomaterials

Metal oxide-based nanomaterials are inorganic nanomaterials, which are widely used to remove heavy metal ions, dyes and other pollutants (Lu and Astruc, 2020). Nanosized metal oxides have high surface area and specific affinity and possess minimal environmental impact, low solubility, and are not involved in secondary pollution formation (Wang *et al.,* 2020). They have also been accepted as adsorbents to remove heavy metals and dyes (Yang *et al.,* 2019).

Nanocrystalline metal oxide, MgO, is an interesting functional material due to its low heat capacity, chemical inertness, optical transparency and high thermal stability (Moustafa *et al.,* 2017). Due to its high surface area, it is used as an efficient adsorbent for numerous toxic chemicals and acid gases. Lately, MgO nanoparticles have shown promise for application in tumour treatment and also have considerable potential as an antibacterial agent (Moustafa *et al.,* 2017). Magnesium oxide (MgO) has found extensive important applications in the field of photocatalysis, electronics, refractory materials, pharmaceuticals, and wastewater degradation (Abinaya *et al.,* 2021). MgO has attracted major interest in biological applications due to its non-toxic nature (Karthik *et al.,* 2019).

Therefore, considerable effort has been focused toward the growth of visible-light active materials and two strategies have been proposed regarding it. The first approach is the coupling of wide bandgap material with narrow bandgap material to form heterostructures, which has been proven an effective strategy, and the second approach is the investigation and growth of innovative semiconductor materials with narrow bandgap (Tahir *et al.,* 2017). Apart from MgO nanoparticles, WO_3 has attracted significant scientific interest due to its unique chemical, functional, physical properties, small bandgap energy (2.4-2.8 eV), stable physicochemical properties, deeper valence band (3.1 eV) and strong photo corrosion stability in aqueous solution as well as stable recyclability performance (Lai, 2015). However, WO_3 is still far from becoming a practical

nanoadsorbents applications due to its low surface area. Since the process of electrons transfer to the conduction band of the oxide is a surface phenomenon, it is anticipated that the larger the specific surface area of the semiconductor is, the better the adsorption efficiency (Tahir *et al.*, 2017).

2.6 Nanomaterials Synthesis Methods

Several techniques such as microemulsion, chemical co-precipitation, sol-gel and hydrothermal are used to synthesise nanomaterials. Brief of commonly used techniques are presented.

2.6.1. Microemulsion method

Microemulsion (including oil, surfactant and water) is used to make particular sized nanoparticles. All these synthesised nanoparticles have the properties including single-phase, thermodynamically stable and isotropic transparent solution (Simonazzi *et al.*, 2018). The reacting mixtures are extant in nano water droplets enclosed by surfactant molecule. It is a costly method with a low yield of production. Moreover, monodispersed nano-sized particles of dissimilar morphologies and sizes can be made via this method (Tahir *et al.*, 2017).

2.6.2 Chemical co-precipitation

Chemical co-precipitation is a facile, precise and appropriate technique, which yield at a lesser temperature than any other synthesis technique to prepare nanomaterials. During this method, several soluble salts solutions are diverse for explicit ratio and co-precipitated with a base solution (Mourdikoudis *et al.*, 2018). Solutions are dissolved in water, mixed and co-precipitated with alkali very slowly. Subsequently, the solution was

stirred and the precipitates formed were sieved, washed, dried and sintered at a certain temperature.

2.6.3 Sol-gel technique

The sol-gel method is the most practical and simplest method that can control the morphology, grain size and particle size by systematic observing of reaction parameters (Arya *et al.,* 2021). It is the most popular technique in which the formation of an oxide network takes place through polycondensation reactions of a molecular precursor in a liquid (Esposito, 2019). The formed precipitates are washed, dried and calcined at elevated temperatures to form nanocrystals of metal oxides (Mustapha *et al.,* 2020).

2.6.4 Hydrothermal method

Hydrothermal is a single step, cost-effective and easy method used for the synthesis and preparation of nanomaterials and is also known as solvothermal technique. Teflon-lined stainless steel autoclave is used for the reaction at high pressure and temperature (Colpani *et al.,* 2018). Reaction kinetics may be controlled by microwave heating during this technique. Nanoparticles synthesised via this technique show much better crystallinity and grain size (Zhou *et al.,* 2017). Calcination is a very effective technique that is sustainable at high temperature in which reaction achieved lower the melting points. An explosive fraction is detached, and phase-transition and thermal putrefaction take place in this method (Gnanamuthu *et al.,* 2019).

2.7 Factors affecting the interaction of nanomaterials in aqueous media

The physical and chemical properties of flow can strongly affect the retention and transport of nanomaterials in porous media. The physical properties mainly refer to hydrodynamic conditions of flow in porous media including velocity and direction, which affect the advective and dispersive transport of the nanomaterials. The chemical properties

mainly refer to solution ionic strength (IS), ion valence, and pH, which can alter the interactions between nanomaterials and the surrounding environment (Wang *et al.,* 2016).

2.7.1 Solution pH

Solution pH can change the zeta potential of synthesised nanomaterials and affects their fate and transport in porous media (Rawat *et al.,* 2018). As the pH increases, the zeta potential of nanomaterials may reduce gradually. When pH is around the point of zero charges (pzc), where the surface potential is approximately zero, the nanomaterials are in an extremely unstable state. The repulsive force between nanomaterials hardly exists, so it is easy for nanomaterials to aggregate and deposition results (Pasinszki and Krebsz, 2020). When solution pH is below the pzc, the nanomaterials surfaces are positively charged; when pH is over the pzc, the surfaces are negatively charged. The greater the absolute difference between eluent pH and pzc, the higher the repulsion between nanomaterials is and the more stable they are (Wang *et al.,* 2016). It has been demonstrated that nanomaterials transport in porous media is low when the solution pH is near the pzc, promoting their aggregation. When nanomaterials aggregate size is larger than a threshold, pore straining and gravitation sedimentation may increase their deposition in porous media. Solution pH can also alter the surface charges of the porous media to affect material transport (Farner *et al.,* 2020). Where solution pH is over the pzc values of both nanomaterials and collectors, electrostatic double-layer repulsive forces are induced, which reduces the deposition of nanomaterials in the porous media (Ma *et al.,* 2018).

2.8 Adsorption Technology

The adsorption process is a surface phenomenon in which the adsorbate is accumulated on the adsorbent surface (Crini *et al.,* 2019). When a solution containing absorbable solute

comes into contact with a highly porous solid surface structure, liquid-solid intermolecular forces of attraction cause some of the solute molecules from the solution to be concentrated or deposited on the solid surface (Kandisa *et al.,* 2016). In the case of bulk materials, all the bonding requirements (ionic, covalent, or metallic) of the material constituent atoms are filled by other atoms in the material. However, the atoms on the surface of the adsorbent are not wholly surrounded by other adsorbent atoms, therefore they can attract adsorbates (Sadegh *et al.,* 2017). The exact nature of the bonding depends on the species involved, but the adsorption process is generally classified as physisorption (an adsorbate bound to the surface by weak van der Waals forces), or chemisorption (an adsorbate tethered through covalent bonding or due to electrostatic attraction (Dobrota *et al.,* 2020).

The limited active site, surface area and low efficiency of the conventional adsorbents in comparison to nanoadsorbents offer a considerable advancement with their high adsorption kinetics (Chai *et al.,* 2021). This was demonstrated by their extremely high specific surface area and associated sorption sites, short intraparticle diffusion distance, and tunable pore size and surface chemistry that provide useful features for effective adsorption (Zare *et al.*, 2015). Their great adsorption capacity is mainly because of their high specific surface area and the highly active adsorption sites that are created by high surface energy and size-dependent surface structure at the nanoscale (Sadegh *et al.*, 2017). The nanoadsorbents are effectively used in the removal of organic compounds, and metal ions and their selectivity toward particular pollutants can be increased by functionalization.

Nanoscale metal oxides, such as magnesium oxide and tungsten oxide, zinc oxides, alumina, among others have been explored as a low-cost, effective adsorbent for water treatment offering a more cost-efficient remediation technology due to their size and

adsorption efficiency (Cañas-Carrell *et al.,* 2014). The adsorption is controlled by forming a complex with the surface of nanoscale metal oxides and undergoing ion-exchange mechamism. These nanoparticles have drawn a considerable concern because of their potential application in wastewater treatment (Islam *et al.,* 2017).

2.8.1 Factors affecting adsorption

The factors affecting dye adsorption include contact time, solution pH, temperature, competing ions and initial dye concentration. The effects of these parameters are to be taken into account and the optimization of such conditions help in the development of industrial-scale dye removal treatment process. Some of the factors affecting adsorption of dyes are discussed as follows:

2.8.1.1 *Contact time*

It is an important factor in adsorption study because it depends on the type of adsorbate and adsorbent used. In most of the investigated cases, it was reported that as the contact time increase, the percentage of adsorption also increase until the equilibrium is reached and further attain desorption (Daneshvar *et al.,* 2019).

2.8.1.2 *Effect of solution pH*

One of the most important factors affecting the capacity of adsorbent in wastewater treatment is solution pH. The efficiency of adsorption is dependent on the solution pH since variation in pH leads to the variation in the degree of ionization of the adsorptive molecule and the surface properties of adsorbent (Joshi and Srivastava, 2019).

The adsorption ability of the surface and the type of surface-active centres are indicated by the significant factor that is the point of zero charges (pHpzc). The pH at which the surface charge is zero is called the point of zero charges (pzc) and is typically used to quantify or define the electrokinetic properties of a surface (Homagai, 2018). The value of

pH is used to describe pzc only for systems in which H^+/OH^- are the potential determining ions. Many researchers studied the point of zero charges (pHpzc) of various adsorbents prepared from agricultural solid wastes; to understand the adsorption mechanism (El-Gendy and Nassar, 2020). Due to the presence of functional groups such as OH^- group, cationic dye adsorption is favoured at pH > pHpzc, whereas, anionic dye adsorption is favoured at pH < pHpzc where the surface becomes positively charged (Stavrinou *et al.*, 2018).

2.8.1.3 *Effect of amount of adsorbent*

Adsorbent dosage is an important process parameter to determine the capacity of an adsorbent for a given amount of the adsorbent at the operating conditions. Generally, the percentage of dye removal increases with increasing adsorbent dosage, where the number of sorption sites at the surface of adsorbent will increase by increasing the amount of the adsorbent (khamis-Soliman *et al.,* 2019). The effect of adsorbent dosage gives an idea for the ability of dye adsorption to be adsorbed with the smallest amount of adsorbent, to recognize the capability of a dye from an economical point of view (Azari *et al.*, 2020).

2.8.1.4 *Competing ions*

The capacity of the adsorbent was revealed to be affected by the presence of foreign ions in the pollutant solution. The adsorption process in multicomponent systems was found to be complex and could be a function of parameters such as pH, ionic radius, the presence of free active sites on the adsorbent and the electronegativity. This is due to the ion-ion competition and ion-surface interactions taking place at the active sites of adsorption (Taka *et al.,* 2018).

2.8.2 Adsorption isotherm models

The adsorption isotherm models depict the amount of solute adsorbed per unit weight of adsorbent as a function of the equilibrium concentration in the bulk solution at a constant temperature. These isotherms include Langmuir and Freundlich, Temkin, Harkin-Jura and Dubinin–Radushkevich (Girish *et al.,* 2017). Among them, Langmuir and Freundlich models are commonly used for the description of adsorption data. Langmuir isotherm refer to the homogeneous adsorption on the surface of adsorbent.

On the other hand, Freundlich isotherm describes heterogeneous surface adsorption. The energy distribution for adsorptive sites (in Freundlich isotherm) follows an exponential type function which is close to the real situation. The rate of adsorption/desorption varies with the strength of the energy at the adsorptive sites (Kumar *et al.,* 2019).

2.8.2.1 *Langmuir model*

The Langmuir model was developed on the assumption that all adsorption processes happens on a homogeneous surface and that all binding sites have equivalent affinity for the adsorbate, thus leading to the formation of a monolayer of the adsorbates (Munagapati and Kim, 2017). The Langmuir adsorption isotherm is represented mathematically using Equation 2.1:

$$q_e = \frac{q_m K_L C_e}{1+K_L C_e} \quad (2.1)$$

Equation 2.1 can be linearized to obtain Equation 2.2:

$$\frac{1}{q_e} = \frac{1}{q_m} + \frac{1}{K_L q_m}\frac{1}{C_e} \quad (2.2)$$

where q_m (mg/g) is the maximum adsorption capacity with complete monolayer coverage on the adsorbent surface, C_e is the metal concentration at equilibrium (mg/g) and k_L is the Langmuir constant (L mg^{-1}). The Langmuir constants K_L and q_m can be determined from linear plot of $\frac{1}{C_e}$ versus $\frac{1}{q_e}$.

where C_0 is the initial concentration and K_L is the constant related to the Langmuir constant (energy of adsorption). The Langmuir isotherm assumes that metal ions are chemically adsorbed, where each site can hold only one adsorbate and all sites are energetically equivalent and that there is no interaction between ions.

2.8.2.2 *Freundlich model*

Freundlich isotherm is a significant adsorption isotherm, which is specifically for heterogeneous surface.., it has been used extensively to study heavy metal adsorption which assumes the adsorption process to be multilayer, thereby showing the heterogeneity of the adsorbent surface (Zhou *et al*., 2017). The slope of the isotherm ranges between 0 and 1, which is a measure of the adsorption intensity or surface heterogeneity. As the value gets closer to zero, the adsorbent becomes more heterogeneous (Monte Blanco *et al*., 2017). Meanwhile, a value below unity indicates chemisorption process where 1/n above one shows cooperative adsorption (Chaudhry *et al*., 2016). Freudlich isotherm model is described by Equation 2.3 (Monte Blanco *et al*., 2017):

$$q_e = K_F C_e^{1/n} \tag{2.3}$$

Equation 2.3 can be rearranged to obtain the linear form by taking the logarithms:

$$\log q_e = \log K_F + \frac{1}{n} \log C_e \tag{2.4}$$

where q_e (mg/g) is the quantity of heavy metal adsorbed per unit of the adsorbent at equilibrium, C_e (mg/L) is the concentration of heavy metal solution at equilibrium, K_F [(mg/g)(L/mg)1/n] is the Freundlich adsorption isotherm constant denoting the adsorption capacity, while $1/n$ is a function of intensity and strength of the adsorption process. K_F and $\frac{1}{n}$ values can be calculated from the intercept and slope of the linear plot between $\log q_e$ and $\log C_e$.

2.8.2.3 *Temkin isotherm model*

Temkin isotherm assumes that the drop in the heat of adsorption is linear, not logarithmic as proposed by Freundlich isotherm (Subramani and Thinakaran, 2017). The isotherm comprises of an explicit factor that considers the interactions of the adsorbate and adsorbent (Abdelnaeim *et al*., 2016). Consequently, Temkin isotherm is established on the assumption that interactions between adsorbate and the adsorbent results in the linear decrease of the heat of adsorption (function of temperature) of adsorbing ions with the coverage of adsorbent surface (Chaudhry *et al*., 2017). The derivation of Temkin equation is categorized by even distribution of binding energies up to high energetic sites (Subramani and Thinakaran, 2017). Temkin isotherm model equation is represented in Equation 2.5:

$$q_e = \frac{RT}{b_T} \ln (A_T C_e) \quad (2.5)$$

The linearized form of Equation 2.5 is shown in Equation 2.6:

$$q_e = \frac{RT}{b_T} \ln A_T + \left(\frac{RT}{b_T}\right) \ln C_e \quad (2.6)$$

where A_T (L/g) and b_T (kJ/mol) are Temkin constants that are related to maximum binding energy and heat of adsorption. The A_T and b_T constants are calculated from the slope and intercept of the plot of q_e aganist $\ln C_e$. R (8.314 J/mol.K) is the universal gas constant and T is the temperature (K).

2.8.3 Kinetic models

An applicable kinetic model is used to analyze the rate and the mechanism of adsorption processes such as mass transfer and chemical reaction. Several kinetic models such as simple-first-order, pseudo-first-order, pseudo-second-order and intra-particle diffusion

models have been applied to disclose the adsorbate-adsorption phenomenon (Kajjumba *et al.*, 2018).

2.8.3.1 *Pseudo-first order kinetic model*

This kinetic model was the first to be utilized to study adsorption in liquid-solid system. It was proposed by Lagergren, but was modified by Ho (Ho, 2016). It is used extensively to investigate the adsorption of an adsorbate from aqueous solution. This model was established on the assumption that the rate of change of solute adsorption with time is proportional to the saturation concentration difference and the quantity of solid adsorption with time (Zhou *et al*., 2017).

The linearized mathematical form of the model is given by the following Equation:

$$\frac{dq_t}{dt} = k_1(q_e - q_t) \quad (2.7)$$

If q_t = 0 at t = 0, Equation 2.7 can be integrated to obtain Equation 2.8

$$\log(q_e - q_t) = \log q_e - \frac{k_1 t}{2.303} \quad (2.8)$$

where q_e and q_t are the quantity of heavy metal uptake per unit of adsorbent (mg/g) at time t and at equilibrium, k_1 is the pseudo-first order rate constant (min^{-1}) for adsorption process and t is the contact time (min). The adsorption rate constant is calculated from the straight line plot of $\log(q_e - q_t)$ against t.

2.8.3.2 *Pseudo-second order kinetic model*

The pseudo-second order kinetic model was established to describe most of the adsorption systems for the whole range of adsorption period (Shi and Zhang, 2018). This kinetics recommends that the number of adsorption sites on the surface of the adsorbent and the number of heavy metal ions in the solution collectively determine the kinetics (Bouabidi *et al*., 2018). Moreover, the rate-limiting step in pseudo-second order kinetic model is the

formation of chemical bond between the adsorbate and adsorbent at the appropriate sites (Sherlala *et al*., 2018). The pseudo-second order kinetic model is presented in Equation 2.9:

$$\frac{dq_t}{dt} = k_2(q_e - q_t)^2 \quad (2.9)$$

Noting that q_t = 0 at t = 0. The obtained Equation 2.9 can be rearranged into a linear form:

$$\frac{t}{q_t} = \frac{1}{k_2 q_e^2} + \frac{1}{q_e} t \quad (2.10)$$

where k_2 is the pseudo-second order adsorption rate constant (g/mg.min). The values for h, k_2 and q_e are obtained through the linear plot of $\frac{t}{q_t}$ against t.

2.9. Factors Affecting the Synthesis of Nanoparticles

Several factors affect the synthesis, characterisation, and application of nanoparticles. These factors that affect the synthesis of nanoparticles include pH of the solution, temperature and concentration of the raw materials used, size. Some dominant factors that affect nanoparticle are as follows:

2.9.1 pH

pH is an important factor that influences the synthesis of nanoparticles. Researchers have discovered that the pH of the solution influences the size and texture of the synthesised nanoparticle. Therefore, nanoparticle size can be controlled by altering the pH of the solution media (Rao *et al.*, 2017).

2.9.2 Temperature

Temperature is another important parameter that affects the synthesis of nanoparticles. The physical method requires the highest temperature (>350°C), whereas chemical methods require a temperature of less than 350°C. The temperature of the reaction medium determines the nature of the nanoparticle formed (Roy *et al.,* 2018).

2.10 Characterisation Techniques of Synthesised Nanoparticles

The synthesis of nanoparticles is broadly classified into top-down approach and bottom-up approach. The top-down approach deals with material size reduction of particles through the physical and chemical process to produce nanoparticles (Khan *et al.,* 2019). The size, shape, overall physicochemical properties and surface structure are processed throughout the process. The bottom-up approach deals with engineering at the atomic, molecular level (Kumar *et al.,* 2018). Nanoparticles of different size, shape, surface area are characterised by various techniques like UV-visible spectroscopy (UV-vis), powder X-ray diffraction (XRD), Fourier transform infrared spectroscopy (FT-IR), energy dispersive spectroscopy (EDS), dynamic light scattering (DLS), Zeta potential, scanning electron microscopy (SEM), transmission electron microscopy (TEM) and atomic force microscopy. Composition, size, structure, crystal phase is also determined from spectroscopy technique like UV-vis, XRD, FT-IR, DLS, EDS and Raman. DLS analysis estimates the size distribution and quantifies the surface charges of nanoparticles. Element composition is the determination by EDAX analysis. XRD identifies the crystallite size. FTIR spectroscopy identifies the surface residues and functional groups which are attached to the surface of nanoparticles during their synthesis for their efficient reduction and stabilization.

2.10.1 High resolution scanning microscopy (HRSEM)

HRSEM is the technique of choice for analysis of specimen surfaces. The typical layout of an SEM, which encompasses the electron gun (electron source and accelerating anode),

electromagnetic lenses focus on the electrons, a vacuum chamber housing the specimen stage, and a selection of detectors to collect the signals emitted from the specimen (Inkson, 2016). The electron beam is focused to a spot, and is scanned sequentially across the specimen. At each location, signals are emitted from the specimen and collected by detectors. The detector signal is synchronized with known location of the beam on the specimen, and the signal intensity is used to modulate the corresponding image pixel. The signals collected in series are combined to form an image whose dimensions/pixel distribution depends on the scan pattern chosen. Typical electron energies are 1-30 keV (Inkson, 2016).

2.10.2 High resolution transmission electron microscopy (HRTEM)

TEM is the technique of choice for analysis of specimen internal microstructure, evaluation of nanostructures such as particles, fibers, and thin films, and imaging of atoms. The key components of a TEM microscope, which comprises the electron gun, electrostatic lenses focus on the electrons before and after the specimen, and a transmitted electron detection system (Inkson, 2016). TEM microscopes are sensitive characters, requiring installation in vibration-free environments, free of stray electromagnetic fields and at constant temperature. There is much more control of the electron beam required in TEM than SEM, because of the sensitivity of electron scattering to beam profile parameters including angular spread of the electrons and diameter of the electron spot. Methodology for optimization of the electron gun parameters, alignment of multiple lenses, and alignment of apertures which partially block the electron beam at different points, must be determined for each microscope. Alignment of the instrument may take upwards of 30 min at the beginning of the working day, and may need to be periodically adjusted (Inkson, 2016).

2.10.3 X-ray diffraction spectroscopy (XRD)

X-rays are high-energy electromagnetic waves with a wavelength between 10^{-3} and 10^{1} nm. The generation of X-rays is generally achieved by the use of sealed tubes, rotating anodes or synchrotron radiation sources. Sealed tubes and rotating anodes, which are used in laboratory equipment, both produce X-rays by the same principle. Electrons generated by heating a tungsten filament in a vacuum are accelerated through a high potential field and then directed to a target which then emits X-rays (Epp, 2016).

The incident electrons induce two effects leading to the generation of X-rays: the first is the deceleration of the electrons leading to the emission of X-ray photons with a broad continuous distribution of wavelength, also called Bremsstrahlung. The second is the ionization of the impinged atoms by ejecting electrons from the inner shells. In order to get a more stable state, electrons from outer shells "jump" into these gaps. The difference between the electron energies of the inner shell and of the incoming electron is emitted in the form of photons, with a characteristic energy depending on the initial and final shell position of the electrons and on the material. The characteristic radiation requires minimum excitation potential of the electrons to be emitted, which depends on the target material (Epp, 2016).

2.11 Review of Previous Related Works

Lidocaine (LDC) is a prevalent positional drug of anaesthetic and found in aqueous environments as a pollutant due to its widespread use. The indiscriminate use of the chemicals leads to its release into the environment and it is a crucial ecological problem. The removal of pharmaceutical pollutants from industrial effluent is a difficult task. Many biological and physical techniques are being routinely used for removal of these pharmaceutical pollutants. The use of tungsten trioxide (WO_3) nanoparticles for the removal of Lidocaine (LDC) was reported by Fakhr z, (201 nanoparticles were synthesised and characterised by scann croscop

0.2 M

Solution

transmission electron microscope (TEM), X-ray diffraction (XRD), UV–Visible (UV–Vis) spectroscopy and Brunauer-Emmett-Teller (BET) techniques. The nanoparticles showed a maximum removal efficiency effect at pH 6 and it degraded 95.48 % and 97.5% of LDC within 1 h under visible and sunlight, respectively.

In the study investigated by Fathi *et al.* (2019), MgO/C_3N_4 nanocomposite was synthesised via facile and characterised by Fourier-transform infrared spectroscopy, X-ray diffraction, Field emission scanning electron microscopy, Energy-dispersive X-ray spectroscopy and Dot mapping. Then the efficiency of synthesised MgO/C_3N_4 nanocomposite was investigated in removal of Reactive Orange 16 (RO16) dye from aqueous solutions in a batch system. The results obtained showed that the removal percentage of RO16 dye decreases by increasing RO16 dye concentration and increasing MgO/C_3N_4 nanocomposite dosage. The optimum pH for the removal of RO16 was pH 6. The maximum removal of RO16 dye was obtained 82 % under 39.6 W visible light radiation, 2 mg/L of RO16 dye concentration, 0.2 g/500 mL of MgO/C_3N_4 nanocomposite dosage, pH 6 and 30 min contact time.

The results showed that the removal efficiency of WO_3/Graphene oxide was enhanced when WO_3 was mixed with graphite and suggested that 15 wt % of graphite was the optimal level in the composite thin film. The adsorption data followed pseudo-first-order kinetics. Repeatability determines the feasibility of thin films using real applications. Here, all the thin films showed good stability for up to five cycles (Hossain *et al.*, 2019).

The synthesised nanostructured MgO from different organic precursors, by a facile precipitation method as catalysts for the decontamination of Malathion and orange as organic pollutants, was studied by Moustafa *et al.* (2017). The as-prepared nanoparticles were obtained by thermal decomposition of the oxalate, tartrate, citrate, succinate, malate, malonate and glycinate precursors at 650°C and characterised by thermal analysis, FTIR,

X-ray diffraction, high-resolution transmission electron microscope (HRTEM) and absorption spectra. The morphology and crystal sizes were found to be highly affected by the starting organic precursors. The results revealed that the prepared nanoparticles have high potential as nano catalysts for removal of both Malathion and orange G from water samples.

The CdO/MgO nanocomposites were synthesised and investigated by XRD, FESEM with EDS and FTIR. XRD shows a cubic structure with an average crystallite size of 44 nm (CdO), 37 nm (MgO) and 32 nm (CdO/MgO). The adsorptive removal study of ultrasonic-assisted CdO and MgO nanoparticles and CdO/MgO nanocomposite showed high percentage removal of alizarin red S dye under the applied conditions (Karthik *et al.*, 2019).

2.12 Identified Research Gap

This section reviewed the use of WO_3 and MgO nanoparticles and their composites as well as various wastewater treatment technologies used in recent times for the removal of different pollutants/contaminants in dyeing wastewater. The review further identified the characterisation techniques and gaps which are being filled by this study.

S/N	Author	Title	Findings	Gap Analysis
1.	Salem, A. N. M., Ahmed, M. A., & El-Shahat, M. F. (2016)	Selective adsorption of amaranth dye on Fe_3O_4/MgO nanoparticles	Investigation of removal amaranth food stuff dye on magnetic Fe_3O_4/MgO nanoparticles synthesised by facile sol-gel route. XRD, FESEM and HRTEM analysis showed existence of rod-like structure MgO nanoparticles of average size of about 14 nm in diameter and 22 nm in length. The adsorption capacity is 37.98 mg/g. The enthalpy change is17.03 kJ/mol which indicates that the removal process is endothermic. The kinetic process follows pseudo-second order rate equation and the negative values of standard free energy ($\Delta G°$) demonstrated that the adsorption process is spontaneous.	- Biosynthesis route was not followed. - The nanocomposite material was not characterised using EDX, BET and SAED. - Error functions such as sum of square error and chi square error were not used to validate the fitness of the adsorption isotherms and kinetic models.
2	Azeem, Abdul, *et al* (2016).	Synthesis of Tungsten Oxide Nanorod, Its Application on Textile Material, and Study of Its Functional Properties	-Nanorods were synthesised by hydrothermal method. -The nanostructures were grown on polyester fabric as it withstands curing temperature easily. -Results revealed that although the seeded solution is perfect, the conductivity of tungsten trioxide cannot be achieved on textiles.	- Green synthesis technique was not employed in this study. - The synthesised tungsten oxide nanorod was not incorporated with metallic or nonmetallic oxide. - Characterisation techniques such as XRD, HRTEM,

				EDX, SEAD and BET were not carried out in this study. - Regeneration study was not carried out.
3	Ghasemi, L., & Jafari, H. (2017).	Morphological characterisation of tungsten trioxide nanopowders synthesised by sol-gel modified Pechini's method	Synthesised WO_3 nanopowders Sol-gel modified Pechini's method. The results revealed that the as-prepared WO_3 nanopowders through different amounts of chelating agent and polyethylene glycol, crystallized in monoclinic phase. presence of the complexing agent and Morphological evolution indicated that the nanopowders evolved from rod-like to regular and spherical shapes, depending on complexing agent and polyethylene glycol amounts.	- Green synthesis method was not used - WO_3 was not incorporated with MgO - HRTEM, SEAD and BET were not employed in this study. - Performance evaluation of the developed nanoadsorbent on local dyeing wastewater was not done. - Regeneration study was not carried out.
4	Ama, O. M. (2017).	Exfoliated graphite/tungsten trioxide nanocomposite electrode for the photoelectrochemical degradation of eosin yellow and methylene blue in wastewater.	Synthesised EG-WO_3 - Photoelectrochemical degradation of Eosin yellowish and methylene blue dyes in water using simulated sunlight. -The EG-WO_3 photoanode showed a significant decrease in the dye concentration (20 ppm). This illustrates that the WO_3 nanoparticle in the EG-WO_3 composite enhanced the degradation efficiency of the eosin yellow.	- Green synthesis method was not used - Adsorption technology was not employed in this study. - Performance evaluation of the developed nanocomposite material on local dyeing wastewater was not carried out.
5	Fakhri, A.,	Comparison studies of	The adsorption measure of linezolid antibiotic onto	- Nanodsorbents

	& Behrouz, S. (2015)	adsorption properties of MgO nanoparticles and ZnO–MgO nanocomposites for linezolid antibiotic removal from aqueous solution using response surface methodology	MgO nanoparticles and ZnO–MgO nanocomposites were performed. The adsorbents were characterised by different techniques such as XRD, SEM, TEM and BET Performing adsorption tests at optimal conditions set as 0.5 g L^{-1} of adsorbent, pH 10 and 308 K make admit to obtain high adsorption turnover (123.45 and 140.28 mg g^{-1} for MgO nanoparticles and ZnO–MgO nanocomposites, respectively)	regeneration and reusability studies were not performed.
6	Fakhri, A., & Behrouz, S. (2015)	Photocatalytic properties of tungsten trioxide (WO_3) nanoparticles for degradation of Lidocaine under visible and sunlight irradiation.	The present study reports on the use of tungsten trioxide (WO_3) nanoparticles for the degradation of LDC by making use of the photocatalytic property of NPs. WO_3 NPs was synthesised and characterised by SEM, TEM, XRD, UV–Vis spectroscopy and BET techniques. WO_3 NPs showed a maximum photocatalytic effect at pH 6 and it degraded 95.48% and 97.5% of LDC within 1 h under visible and sunlight, respectively.	- Adsorption potential of the as-prepared WO_3 nanoparticles was not tested. - Regeneration study was not carried out
7	Fathi, E., Derakhshan fard, F., Gharbani, P., & Tabatabaei, Z. G. (2020)	Facile Synthesis of MgO/C_3N_4 Nanocomposite for Removal of Reactive Orange 16 Under Visible Light.	In this research, MgO/C_3N_4 nanocomposite was synthesised via facile and economical method and was characterised by FTIR, XRD, FESEM, EDS and Dot mapping. Then efficiency of synthesised MgO/C_3N_4 nanocomposite was investigated in removal of Reactive Orange 16 (RO16) dye from aqueous solutions under visible light in a batch system. Results obtained from photocatalytic removal	- Wet impregnation method was not used for the doping of C_3N_4 on MgO nanoparticle. - Adsorption technology was not used in this study. - Recoverability and reusability study for the

			showed that removal percentage of RO16 dye decreases by increasing RO16 dye concentration and increasing MgO/C_3N_4 nanocomposite dosage. The optimum pH for the removal of RO16 was pH 6. As results, maximum removal of RO16 dye was obtained about 82% in following conditions: Visible light radiation = 39.6 w, RO16 dye concentration = 2 mg/L, MgO/C_3N_4 nanocomposite, dosage = 0.2 g/500 mL, pH 6, time = 30 min. Accordingly, it can be concluded that the synthesised MgO/C_3N_4 nanocomposite can be used as an efficient photocatalyst under visible light for the removal of RO16 dye.	nanocomposite material was not carried out.
8	Dursun, S., Koyuncu, S. N., Kaya, İ. C., Kaya, G. G., Kalem, V., & Akyildiz, H. (2020)	Production of CuO–WO_3 hybrids and their dye removal capacity/performance from wastewater by adsorption/**photocatalysis**	WO_3 nanofibers were combined with different amounts of CuO particles by a simple dispersion dropping technique. Structural, morphological and optical properties of the samples were characterised by XRD, Raman, FT-IR, XPS, SEM, TEM, UV–vis, and Mott-Schottky measurements. Experimental results have shown that the hybrid samples containing only 0.75 wt.% CuO could adsorb 38.4% higher and degraded 25.7% faster the methylene blue dye compared to pure WO_3 nanofibers.	- Wet impregnation method was not used for the doping of CuO on WO_3 nanoparticle. - Recoverability and reusability study for the nanocomposite material was not carried out.

CHAPTER THREE

3.0 MATERIALS AND METHODS

3.1 Equipment/Reagents

This chapter provides detail of the materials, experimental procedures, and characterisation techniques used to achieve the aim and objectives of the study.

All chemicals and reagents used for this study are provided in Table 3.1 and were of analytical grade and were used without further purification, while Table 3.2 represent the list of different analytical tools used to characterised the prepared nanomaterial and analyzed the raw and treated local dyeing wastewater.

Table 3.1: List of chemicals

S/ N	CHEMICAL	PURITY (%)	SUPPLIER
1	$Na_2WO_4.2H_2O$	99.6	Sigma-Aldrich
2	HCl	36.5	Sigma-Aldrich
3	$Mg(NO_3)_2.6(H_2O)$	98.0	Sigma-Aldrich
4	NaOH	80.0	Sigma-Aldrich
5	HNO_3	69.50	BDH Chemicals England
6	H_2SO_4	97.9	BDH Chemicals England
7	Na_2CO_3	98.5	Kermel China
8	Na_2SO_4	99.5	Sigma-Aldrich
9	$(K_2Cr_2O_7)$,	99.8	Sigma-Aldrich

Table 3.2: List of Equipment

S/N	Equipment	Model	Location
1	UV – Visible Spectrophotometer	Shimadzu UV-1800	STEP B FUT, Minna
2	HRSEM (High Resolution Scanning Electron Microscope)	Zeiss Auriga	University of the Western Cape South-Africa
3	HRTEM (High Resolution Transmission Electron Microscope)	Zeiss Auriga	University of the Western Cape South-Africa
4	XRD (X-RAY Diffractometer)	Bruker AxS D8 radiation	Themba Laboratory Cape Town, South-Africa
5	BET (Brunauer Emmett Teller)	NOVA 2400e	STEP B, FUT Minna
6	AAS (Atomic absorption spectroscopy)	Varian AAn240 FS	Multi-User Science Research Laboratory, Zaria
7	Analytical balance weighing balance	Weight Measurement	STEP B, FUT Minna
8	pH meter		STEP B, FUT Minna
9	Ultra-pure water system		STEP B, FUT Minna
10	Water bath Shaker	Gallenkamp	STEP B, FUT Minna
11	Magnetic stirrer	JENWAY 1000	STEP B, FUT Minna
12	Vacuum evaporator	Gallenkamp	STEP B, FUT Minna
13	Furnace		STEP B, FUT Minna
14	Ultrasonicator	Gallenkamp	STEP B, FUT Minna
15	Conductivity Meter	Kent EIL 5013	Niger State River Basin
16	Turbidity Meter	WT3020	Niger State River Basin
17	Dissolved Oxygen Meter	Multi 3420	Niger State River Basin

3.2 Methods

3.2.1 Collection of plants

Fresh leaves of *Polyathia longifelia* (Masquerade tree), *Ficus benjamina* and *Terminelia catappa* (Satellite tree) were collected from Trade Fair Centre in Chanchaga Local Government Area of Niger State in the North Central region of Nigeria. The leaves were first stripped from their stems, thoroughly washed with de-ionized water and then dried for 5 days under sunlight to remove water content. The dried samples were then milled into powder using an electric blender and carefully sieved with 2 μm diameter mesh to obtain the homogeneous size products.

3.2.2 Wastewater sample collection and pretreatment

Local dyeing wastewater was collected in a cleaned plastic container from No 23, Chawai Street, Unguwan Sanusi, Kaduna South, Kaduna State in the North-Western region of Nigeria on 21st February, 2020. The plastic container was pre-washed with 10 % dilute HCl and thoroughly rinsed with de-ionized water before the sample was collected. The wastewater was taken to the laboratory and preserved at 4 ^{o}C in the refrigerator. This was to ensure there were no changes in the physicochemical parameters of the wastewater before batch adsorption study.

3.3 Methodology

The experimental approach followed for the preparation of plant extract, synthesis of WO_3 and MgO nanoparticles, incorporation of WO_3 with MgO to form a bimetallic oxide nanocomposite and the physicochemical analysis carried out are detailed in the next section.

3.3.1 Preparation of plant extract

Approximately 20.0 g of the powdered plant samples of (*Polyathia longifelia, Ficus benjamina* and *Terminalia catappa*) were weighed into a separate 500 cm^3 beakers containing 200 cm^3 of distilled water in the ratio of 1:10 (w/v). The mixtures were kept under continuous stirring condition on a hot plate and stirred for 45 min at 120 rpm and 80 ^oC. The resultant light brownish mixtures were then allowed to cool at room temperature condition before filteration with Whatman No 42 filter paper. The aqueous leave extracts obtained were then transferred into already washed plastic bottles and then taken for quantitative phytochemical screening.

3.3.2 Quantitative phytochemical screening of plant extracts

The quantities of bioactive compounds such as flavonoids, total phenolic contents and tannins present in the selected plant extracts were determined using standard methods described by Roghini and Vijayalakshmi, (2021).

3.3.2.1 *Total flavonoids content determination*

Aluminum chloride colorimetric method was used for flavonoids determination. Each plant extract (0.5 cm^3) was separately mixed with 1.5 cm^3 of methanol, 0.1 cm^3 of 10 % aluminum chloride, 0.1 cm^3 of 1 M sodium acetate and 2.8 cm^3 of de-ionized water. The mixture was maintained at room temperature for 30 min; the absorbance of the reaction mixture was measured at 415 nm with a double beam spectrophotometer (USA). The calibration curve was prepared by preparing quercetin solution. The total flavonoids content (mg/g) in the plant sample was then calculated using Equation 3.1:

$$C = \frac{xV}{w} \qquad (3.1)$$

where x = concentration of the standard obtained from absorbance using Beer-Lambert's Law, C = the total Flavonoids content (mg/g), V= volume of plant extract taken in cm^3, w = weight of plant extract in g.

3.3.2.2 Determination of total phenols content

Appropriate dilutions of the extracts (0.5 cm^3) were oxidized with 2.5 cm^3 of 10 % Folin–Ciocalteau's reagent (v/v) and neutralized by 2.0 cm^3 of 7.5 % sodium carbonate. The reaction mixtures were incubated for 40 min at 45 ^oC and the absorbance was measured at 765 nm in the spectrophotometer. The total phenols content were subsequently calculated as shown in Equation 3.2 using gallic acid as standard.

$$C = \frac{cV}{m} \qquad (3.2)$$

where C = total phenolic content mg/g dry extract, c = amount of gallic acid in mg/cm^3 obtained from calibration curve, V = volume of extract in cm^3, m = mass of plant extract in gram.

3.3.2.3 Total tannins content determination

About 0.2 g of each powdered plant sample was measured into separate 50 cm^3 beakers followed by addition of 20 cm^3 of 50 % methanol. The mixture were then added and covered with para film and placed in a water bath maintained at 77-80 ^oC for 1 h in each case. The mixtures were then shaken thoroughly to ensure a uniform mixing then filtered into 100 cm^3 volumetric flasks using a double layered Whatman No 42 filter paper. Also, 20 cm^3 of distilled water, 2.5 cm^3 folin-Ciocalteu reagent and 10 cm^3 of 17 % Na_2CO_3 were added and mixed properly. The mixtures were made up to mark with distilled water and allowed to stand for 20 min. A bluish-green colour developed at the end of range 0-10 ppm. The absorbance of tannin acid standard solution and the sample were read after colour development on a spectrophotometer at wavelength of 760 nm. The amount of tannin was subsequently calculated using tannic acid as standard. The amount of tannin was calculated using the formula shown in Equation 3.3.

$$\text{Amount of tannin } \left(\frac{\text{mg}}{100\text{g}}\right) = \frac{\text{C x extract volume x 100}}{\text{aliquot volume x weight of sample}} \quad (3.3)$$

where C = concentration of tannic acid.

3.4 Green Synthesis of Tungsten Trioxide Nanoparticles

Sodium tungstate dihydrate, $Na_2WO_4.2H_2O$, was used as a precursor salt in the preparation of WO_3 nanoparticles via biosynthesis route. The choice of *Terminalia catappa* leave extract over the extracts of *Ficus benjamina* and *Polyathia longifelia* leaves was guided by the higher content of secondary metabolites in it than its counterparts. Thus, approximately 10 cm^3 of aqueous leaf extract of *Terminalia catappa* was added in drops to the solution of 0.12 M $Na_2WO_4.2H_2O$ and the mixture was gently heated to 120 ^oC under continuous stirring at 150 rpm for 30 min. Subsequently, 10 % HCl was added in drops to obtain acidic pH 1 considered to be the optimal pH (after attempting pH 3, 4 and 7) due to the maximum yield, stability and extremely higher formation at this pH value. The solution was further stirred for 50 min and allowed to age for 24 h after which the yellowish-brown WO_3 nanoparticles precipitate formed was separated from the aqueous extract, first by decantation and then washed copiously with de-ionized water to remove impurities or residual aqueous extract.

3.4.1 Calcination of the synthesised tungsten trioxide nanomaterial

To obtain the stable monoclinic form of WO_3, the product obtained from the synthesis steps above was first crushed into fine power using motar and pestle and calcined in the furnace at different temperature (75 ^oC, 150 ^oC, 250 ^oC, 350 ^oC, 450 ^oC and 550 ^oC) for 3 h. The route to the formation of WO_3 nanoparticles is displayed in Plate I.

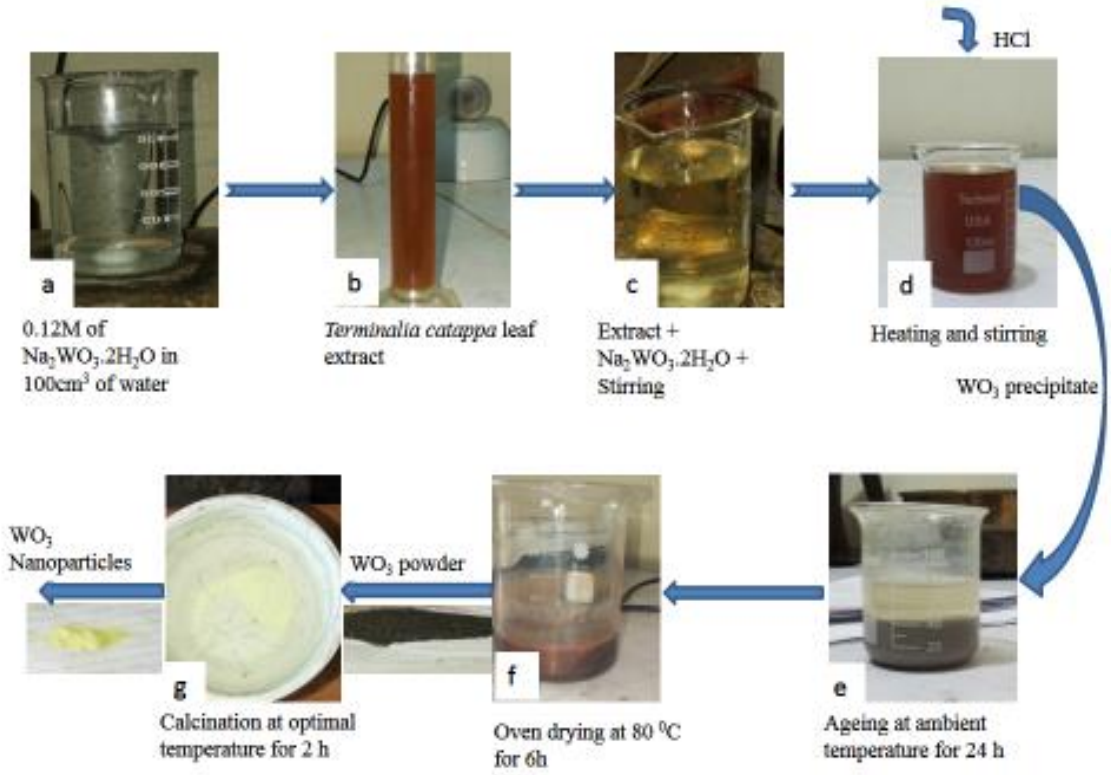

Plate 3.1: Procedure for green synthesis of WO_3 nanoparticles

3.5 Synthesis of Magnesium oxide Nanoparticles

The synthesis of MgO nanoparticle followed the method reported by Agrawal *et al.*, (2015) with a slight modification. Firstly, 5.21 g (0.2 M) of magnesium nitrate hexahydrade was dissolved in 100 cm^3 of de-ionized water in a 500 cm^3 beaker and kept under continuous stirring condition at 150 rpm and 100 ^oC for 30 min and a visibly clear solution was obtained. Secondly, 10 cm^3 of aqueous leave extract of *Terminalia catappa* was added to the solution of the precursor salt in drops using a glass rod and the mixture was further stirred for 30 min under the same conditions. Thirdly, a homogenous solution of 8.0 g (2.0 M) NaOH in 100 cm^3 de-ionized water was prepared and added to the mixture of $Mg(NO_3)_2.6H_2O$ and plant extract in drop-wise in beakers using glass rod until desire pH of 8, 9, 10 and 11 were achieved. A visible colour change from light yellow to dark yellowish-brown accompanying the formation of MgO nanoparticles were observed.

Finally, the mixtures were further stirred on a magnetic stirrer for 2 h followed by filtration and washing severally with de-ionized water so as to get the final products as depicted in Plate II. The final products were then kept in a vacuum oven at 80 ^{o}C for 4 h to remove moisture and dry the product. These dried nanomaterials were first crushed to fine powder using mortal pestle then calcined at 450 ^{o}C for 2 h and the white coloured crystalline MgO nanoparticles were obtained.

The flow chart of procedure is shown below in Figure 3.1, while the pictorial representation of the step by step synthesis of MgO nanoparticles is shown in Plate II.

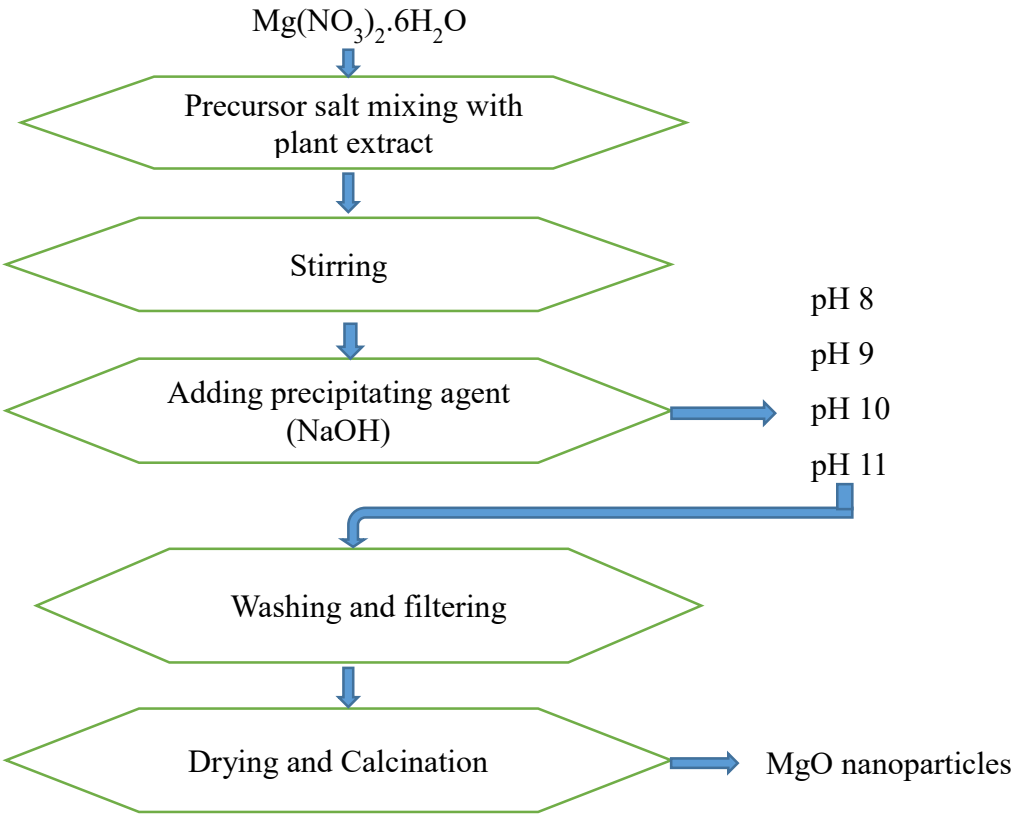

Figure 3.1: Flow chart of procedure for synthesizing MgO nanoparticles (Agrawal *et al.*, 2015)

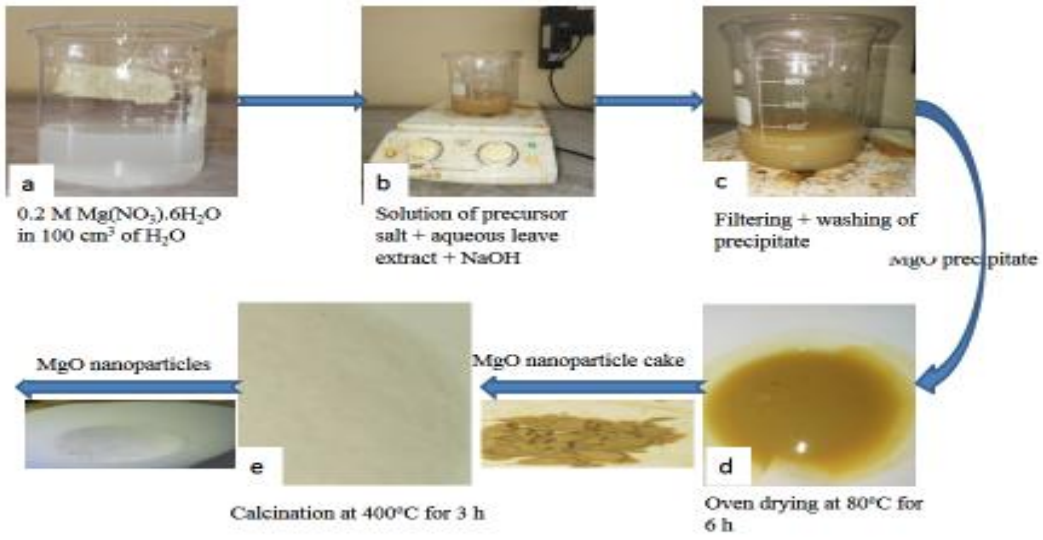

Plate 3.2: Pictorial representation for green synthesis of MgO nanoparticles

3.6 Synthesis of Tungsten trioxide/Magnesium oxide (MgO/WO_3) Nanocomposite

Wet impregnation method was used for the synthesis of MgO/WO_3 nanocomposite. Firstly, known mass (2g, 4g and 8g) of as-synthesised WO_3 powder was dispersed in 30 cm^3 of distilled water and mixed homogenously using ultrasonicator bath operated at room temperature for 30 min. Secondly, known mass (2g, 4g and 8g) of MgO nanoparticles was added to the above mixture and sonicated for another 30 min to obtain various MgO/WO_3 solutions at respective ratios of 1:1, 1:2, 2:1, 1:4 and 4:1. The resultant mixtures were poured into a 50 cm^3 Teflon lined autoclave and heated at 120 ^oC for 3 h. The products obtained were centrifuged, thoroughly washed with de-ionized water, oven dried at 80 ^0C for 6 hrs and calcined at 450 ^oC for 3 h.

3.7 Characterisation Techniques

The WO_3 nanoparticles, MgO nanoparticles and MgO/WO_3 nanocomposites were characterised using HRTEM for particle size microstructure analysis, HRSEM for their morphology, EDS for elemental composition, XRD for the determination of mineralogical phase and BET for their surface-textural properties.

3.7.1 High resolution transmission electron microscopy

The microstructure of the synthesised materials were determined by Ziess Auriga high resolution transmission electron microscopy (HRTEM) couple with energy dispersive spectroscopy (EDS). 0.02 g of the sample was placed in a tube and subjected to ultra-sonication in 10 cm^3 methanol until complete dispersion was obtained. Two drops of the slurry were spread on a holey carbon grid with the aid of a micropipette and subsequently dried by exposure to photo light prior to analysis.

3.7.2 High resolution scanning electron microscopy

The morphologies of the synthesised samples were investigated using a Ziess Auriga HRSEM. Sample (0.05 g) was sprinkled onto carbon adhesives tape and sputter coated with Au-Pd using a Quorum T15OT for 5 min in order to enhance the conductivity of the sample. The microscope was operated with electron high tension at 5 kv to examine the image.

3.7.3 X-ray diffraction

The samples were characterised with the aid of a Bruker D8 Advance X-ray diffractometer with CuKα radiation to determine their crystal phases and crystallite sizes. The powdered sample was placed on the de-greased glass side sample holder and diffractograms were recorded in 2θ range of 20^o to 90^o.

3.8 Characterisation of Wastewater

The water quality parameters such as turbidity, conductivity, dissolved oxygen, biochemical oxygen demand, chemical oxygen demand, nitrate, phosphate, total organic carbon, chloride, sulphate, colour, and selected heavy metals (Cr, Fe and Cu) were determined before and after treatment of the local dye wastewater using the standard methods as described by the American Public Health Association (APHA) (2017).

3.8.1 Determination of temperature and pH

Temperature of wastewater sample was determined by glass-in-mercury thermometer. Immediately after collection of the samples, the pH was determined with an electric pH meter (pH Hanna Instrument Ltd., UK). Prior to the pH determination, the pH meter was calibrated with buffer 4, 7 and 11.

3.8.2 Determination of TDS

TDS in the effluent samples were determined by filtering 100 cm^3 sample through a Whatman No. 42 filter paper to retain fine crystalline particles. The filtrate was transferred onto the evaporating dish and placed on water bath at 100 °C until all the liquid had evaporated, leaving behind on the solid remains. The dish was then placed in an oven at 100 °C for 2 h, and then cooled in desiccators for 30 min. The process of drying and cooling was carried out repeatedly, in the same manner, until a constant weight was acquired. The TDS of a given sample was calculated from the following equation:

$$\text{Total dissolved solids } \left(\frac{\text{mg}}{\text{L}}\right) = \frac{(W_2 - W_1)}{V} \times 1000 \qquad (3.4)$$

where, W_1= weight of the empty dish (mg) W_2= weight of the dish with filtrate residue after evaporation (mg) V= volume of the sample

3.8.3 Determination of TSS

Exactly 100 cm^3 of the wastewater sample was filtered through Whattman No. 42 filter paper. After filtration, the filter paper was dried at 100 °C until a constant weight was achieved. The following formula was used to calculate the TSS in the effluent sample:

$$\text{Total suspended solids } \left(\frac{\text{mg}}{\text{L}}\right) = \frac{(W_2 - W_1)}{V} \times 1000 \qquad (3.5)$$

where, W_1= weight of the filter paper (mg) W_2 = weight of the filter paper and effluent residue after drying (mg) V= volume of the sample

3.8.4 Determination of BOD

BOD of the effluent samples was determined by Winkler method. The assay was carried out by the measurement of dissolved oxygen content of the samples before and after 5 days of incubation at 20 °C. The water sample was freed from residual chlorine using Na_2SO_4 solution. Four times dilution of the sample were made in order to get the depletion in the range of 40 % to 70 %. The dilution water was prepared by aerating (bubbling compressed air) for 1-2 days to attain dissolved oxygen saturation. The formula for calculating BOD is stated below:

$$\text{BOD } \left(\frac{\text{mg}}{\text{L}}\right) = \frac{D_1 - D_2}{V} \qquad (3.6)$$

where, D_1 = DO of diluted sample immediately after preparation (mg/L) D_2 = DO of diluted sample after 5 day of incubation at 20°C (in mg/L) P = Decimal volumetric fraction of sample used.

3.8.5 Determination of COD

COD of the water was determined by the open reflux method. After refluxing the wastewater sample with a known amount of standard potassium dichromate ($K_2Cr_2O_7$), the amount of dichromate consumed was found out by back titration with standard ferrous ammonium sulfate [$(Fe(NH_4)_2(SO_4)2.6H_2O)$] (Mohr salt) and sulpuric acid (H_2SO_4),

respectively in the presence of silver sulfate as catalyst. A blank was also run simultaneously. COD was calculated using the following formula**:**

$$\text{COD}\left(\frac{\text{mg}}{\text{dm}^3}\right) = \frac{(\text{B} - \text{A}) \times \text{N} \times \text{F} \times 1000}{\text{Volume of the sample taken}} \qquad (3.7)$$

3.8.6 Determination of chlorides

A known volume of filtered water sample (50.0 cm^3) was measured in a conical flask, to which about 0.5 cm^3 of potassium chromate indicator was added and titrated against standard (0.014 M) silver trioxonitrate (V) till silver dichromate ($AgCrO_4$) started precipitating and the level of chloride was determined using Equation 3.8.

$$\text{Chloride}\ (\text{mg/dm}^3) = \frac{(\text{A} - \text{B}) \times 35.457 \times \text{N}}{\text{S}} \qquad (3.8)$$

where A = Volume of silver trioxonitrate (V) consumed by the sample (cm^3), B = Volume of silver nitrate consumed by the blank, N = Normality of titrant and S = Volume of the sample (cm^3).

3.8.7 Determination of nitrate (NO_3^-)

A known volume (50.0 cm^3) of the water sample was pipetted into a porcelain dish and evaporated to dryness on a hot water bath. To this, 2.0 cm^3 of phenol disulphonic acid was added to dissolve the residue by constant stirring with a glass rod. A concentrated solution of sodium hydroxide and distilled water was added under continuous stirring to make the solution alkaline. The mixture was filtered into a Nessler's tube and the filtrate was made up to 50 cm^3 with de-ionized water. The absorbance was read at 410 nm using a spectrophotometer after the development of colour. A standard graph was plotted by taking the concentration along X-axis and the spectrophotometric readings (absorbance)

along Y-axis. The level of nitrate was found by comparing absorbance of the sample with the standard curve and expressed in mg/dm^3 and determined using Equation 3.9.

$$\text{Nitrates} = \frac{\text{Absorbance of sample} \times \text{Conc. of Standard} \times 1000}{\text{Absorbance of Standard} \times \text{sample taken}} \qquad (3.9)$$

3.8.8 Determination of sulphate

About 250 cm^3 of the wastewater sample was evaporated to dryness using an evaporating dish on a steam bath. The residue was moistened with a few drops of conc. HCl and 30 cm^3 de-ionized water was added, boiled for 30 min and then filtered using Whatman filter paper No 42. The dish and the Whatman filter paper were rinsed with several portions of de-ionized water. The filtrate was heated to boiling and then 10 cm^3 of 10 % $BaCl_2$ solution was added, drop by drop with constant stirring at 150 rpm. The mixture was digested for about 30 minutes, filtered, and then the filter paper was washed with warm deionized water. Thereafter, ignited, cooled and weighed in an already weighed crucible. The sulphate content was then determined using equation 3.10.

$$\frac{\text{mg}}{\text{dm}^3}\,SO_4^{2-} = \frac{\text{mg } BaSO_4 \times 411.5}{\text{volume of water sample}} \qquad (3.10)$$

3.8.9 Determination of phosphates

About 50.0 cm^3 of the filtered wastewater sample, 4 cm^3 of ammonium molybdate reagent and about 4-5 drops of stannous chloride reagent were mixed together in a 250 cm^3 beaker. After 10 to 12 min, the colour developed was measured on the spectrophotometer at 690 nm. A blank was run with the same treatment with de-ionized water as a sample. The value of phosphate was obtained by comparing absorbance of wastewater sample with the standard curve and expressed in mg/dm^3 using Equation 3.11.

$$\text{Phosphate } \left(\frac{\text{mg}}{\text{dm}^3}\right) = \frac{\text{Absorbance of sample } \times \text{Conc. of Standard} \times 100}{\text{Absorbance of Standard} \times \text{Sample taken}} \qquad (3.11)$$

3.8.10 Determination of heavy metals

The Atomic absorption spectrophotometer (Perkin Elmer 200) was used to determine the concentration of the heavy metals in the local dyeing wastewater such as chromium, iron, and copper in wastewater before and after treatment.

3.9 Adsorption Experiment

Batch adsorption experiments were performed in order to evaluate the equilibrium time, adsorption kinetics, adsorption isotherm and adsorption thermodynamic data. The removal efficiency (% removal) and the adsorption capacity (q_e, mg/g) of some heavy metals in local dye wastewater solution using MgO nanoparticles, WO_3 nanoparticles and MgO/WO_3 nanocomposites were determined.

The adsorption capacities of the nanoadsorbents were determined as follows:

$$\% \text{ removal} = \frac{C_0 - C_e}{C_e} \times 100 \tag{3.12}$$

$$q_e = \frac{(C_0 - C_e)}{M} V \tag{3.13}$$

where C_0 (mg/dm^3) and C_e (mg/dm^3) are the initial and equilibrium liquid phase concentration, respectively; V (dm^3) the volume of the solution and M (g) the mass of the adsorbent.

3.9.1 Optimization of adsorption parameters

3.9.1.1 *Effect of contact time*

The effect of contact time (0-20 min) on adsorption of some heavy metals onto MgO, WO_3 and MgO/WO_3 nanoadsorbents were investigated at constant pH value of 9.98 of wastewater, initial concentration of metal ions in the wastewater and adsorbent dosage of 0.1 g. The amount of adsorbent dosage was added to 40 cm^3 of wastewater solution in a corked 250 cm^3 Erlenmeyer flask, agitated on an orbital shaker at respective time. The solution was filtered with Whatman No 42 and analysed for residual concentrations of

heavy metals. The optimum contact time for each metal analysed was used in this study for the next experiment.

3.9.1.2 *Effect of nanoadsorbent dosage*

The effect of nanoadsorbent dosage on the uptake of some heavy metals from wastewater solution was investigated using adsorbent doses of 0.2, 0.3, 0.4, 0.5 and 0.6 g. doses of specified nanoadsorbent were added to 40 cm^3 of wastewater solution in a corked 250 cm^3 Erlenmeyer flask, agitated at 150 rpm at the optimum contact time of respective heavy metal while the temperature and pH of the solution remain constant. At the end of the shaking period, the flasks were removed from the orbital shaker and then filtered through Whatman No 42. The filtrates were analysed for their residual metal ion concentrations.

3.9.1.3 *Effect of temperature*

The effect of temperature on the metal ion uptake from local dyeing wastewater solution by the nanoadsorbents at temperatures of 30, 35, 40, 45, 50, 55 and 60 ^oC were investigated. The experiments were performed by adding 0.1 g of the nanoadsorbent to 40 cm^3 of dye wastewater in a corked 250 cm^3 Erlenmeyer flask. The resultant mixtures were shaken in a water bath at respective temperature for the optimum contact time. The residual metal ion concentrations in the wastewater samples were filtered and the filtrates were analysed using AAS.

3.10 Adsorption Isotherm

The adsorption equilibrium isotherms describe the interaction between sorbate and sorbent which are established when the amount of solute being adsorbed onto the adsorbent are equal to the amount being desorbed. The Freundlich, Langmuir and Temkin isotherm models are the often used to describe the experimental adsorption data.

3.10.1 *Langmuir isotherm*

Langmuir isotherm assumes the homogeneous adsorption on the surface of adsorbent. The equation of the isotherm is given by:

$$\frac{C_e}{q_e} = \frac{1}{Q_m K_L} + \frac{1}{Q_m} C_e \qquad (3.14)$$

where C_e is the equilibrium concentration of the pollutants in the solution (mg/dm^3), q_e represents the equilibrium adsorption capacity (mg/g), Q_m is the maximum adsorption capacity (mg/g) and K_L denotes Langmuir constant that signifies the affinity between adsorbate and adsorbent (L/mg). A plot of $\frac{Ce}{qe}$ against Ce usually give a straight line with $\frac{1}{Qm}$ and $\frac{1}{Qmkl}$ as slope and intercept respectively.

3.10.2 *Freundlich isotherm*

Freundlich isotherms represents multilayer adsorption adsorbent surface and it is described by the Equation 3.15.

$$\ln q_e = \frac{1}{n} \ln C_e + \ln K_f \qquad (3.15)$$

where K_f and n are Freundlich constants that are related to adsorption capacity and adsorption intensity, respectively. A plot of $\ln q_e$ against $\ln C_e$ gives a straight line graph with $\frac{1}{n}$ and $\ln K_f$ as slope and intercepts repectively.

3.10.3 *Temkin isotherm model*

The Temkin isotherm model assumes that the heat of sorption decreases with the coverage as a result of adsorbate-adsorbent interaction and the linearised form is given in Equations 3.16 and 3.17.

$$\text{Temkin equation: } q_e = B_T \ln a + B_T \ln C_e \qquad (3.16)$$

$$B_T = \frac{RT}{b_T} \qquad (3.17)$$

A plot of q_e versus ln C_e enables the determination of the isotherm constants a and b_T. a is the Temkin isotherm constant known to be the equilibrium binding constant (L/g)

corresponding to the maximum binding energy and b_T (J/mol) is related to the heat of biosorption. The slope and intercept were calculated from the plot of q_e against $\ln C_e$.

3.11 Adsorption Kinetic Models

3.11.1 *Pseudo-first order model*

The pseudo-first order kinetic model assumes that the rate of sorption is proportional to the active adsorbent sites. The equation of Lagergren pseudo-first order is given by Equation (3.18)

$$\ln(q_e - q_t) = \ln q_e - k_1 t \qquad (3.18)$$

where q_e and q_t denote the amount of metals adsorbed (mg/g) at equilibrium and at time, t, respectively and k_1 is the rate constant of pseudo-first order adsorption (min^{-1}).

3.11.2 *Pseudo-second order model*

The pseudo-second order assumes that rate of adsorption sites is proportional to the square of the number of unoccupied adsorbent sites. The equation of pseudo-second order is describe as follows;

$$\frac{t}{q_t} = \frac{1}{k_2 q_e^2} + \frac{t}{q_e} \qquad (3.19)$$

where q_e and q_t are the amount of metals adsorbed at equilibrium and at time, t, respectively and k_2 is the rate constant of pseudo-second order adsorption kinetic (g/mg/min).

3.11.3 *Intra-particle diffusion model*

The basic assumption with intra-particle diffusion model is that film diffusion is negligible and intraparticle diffusion is the only rate-controlling step. According to Weber and Morris (1963), if the rate limiting step is the intra-particle diffusion, then the amount adsorbed at any time t should be directly proportional to the square root of contact time, t and shall pass through the origin. This is defined mathematically as:

$$q_t = K_{id} t^{0.5} + I \tag{3.20}$$

where q_t (mg/g) is the amount adsorbed at time t (min) and K_{id} (mg/gmin$^{0.5}$) is the intra-particle rate constant. The plot of q_t against t determines the K_{id}.

3.12 Thermodynamics Studies

The thermodynamic parameters of the adsorption process such as the standard Gibbs free energy ΔG^{θ} (kJ/mol), standard enthalpy ΔH^{θ} (kJ/mol) and entropy ΔS^{θ} (J/molK), were computed from the Vant Hoff equation using the equilibrium adsorption data from temperature study:

$$\Delta H = -RT\ln K \tag{3.21}$$

$$\ln K = -\frac{\Delta H}{RT} + \frac{\Delta S}{R} \tag{3.22}$$

where the slope and intercept of the plot of $\ln K$ versus $\frac{1}{T}$ were used to determine the ΔH and ΔS. R is the gas constants (8.314 J/mol K) and T (K) is the absolute temperature.

3.13 Regeneration Study

The regeneration was carried out in order to check the reuseability of the nanoadsorbents (MgO, WO_3 and MgO/WO_3). This study was done by treating the used nanoadsorbents with 0.5 M HNO_3. The mixture (HNO_3 and adsorbent) in a corked 250 cm^3 Erlenmeyer flask was kept for 30 min in an orbital shaker at 150 rpm and room temperature. The mixture was completely dried in an oven at 105 ^{o}C. The adsorbed metal ions react with the acid to form their nitrate. The nanoadsorbents were washed severally with de-ionized

water until pH of 7 is attained. Afterward, the nanoadsorbents were oven dried at 105 ^{o}C for 2 days and further calcined in a furnace at 450 ^{o}C for 3 h. The resultant nanoadsorbents were further used in adsorption-desorption cycles. The same adsorbent was re-used for the removal of selected heavy metals in the local dyeing wastewater following the same procedure described in section 3.9.1 under the optimized conditions.

CHAPTER FOUR

4.0 RESULTS AND DISCUSSION

4.1 Qualitative Phytochemical Screening of Plant Extract

The results of the qualitative analysis of the secondary metabolites present in the three leave extracts of *Terminalia catappa* (TC), *Polyalthia longifelia* (PL) and *Ficus benjamina* (FB) leaves are displayed on Table 4.1.

Table 4:1: Qualitative phytochemical screening of *Terminalia catappa* (TC), *Polyalthia longifelia* (PL) and *Ficus benjamina* (FB) leaves

Sample	Phytochemical		
	Tannins (mg/g)	Flavonoid (mg/g)	Total phenol (mg/g)
TC	9.18±0.20	2.73±0.31	6.94±0.22
PL	8.56±0.32	3.75±0.13	4.12±0.40
FB	8.87±0.10	2.80±0.30	4.28±0.32

The tannins, flavonoids and total phenolic contents in the plant samples ranged from 8.56 to 9.18 mg/g, 2.73 to 3.75 mg/g and 4.12 to 6.94 mg/g, respectively. The results of abundance of phytochemical constituents in plant extracts follow this order; TC>FB>PL. From the phytochemical results shown on table 4.1, the components responsible for the reduction of nanoparticles which also serve as capping and stabilizing agents were identified as tannins and phenolic compound. This is agreement with the finding of Asha *et al.* (2017). Among the plant extract analysed in this study, TC had highest tannins and

phenolic compound. Therefore, the choice of plant extract used in this study was *Terminalia catappa*.

4.2 XRD Analysis

4.2.1 WO_3 nanoparticles

The crystal phase of WO_3 nanoparticles prepared at pH 1 and calcined at different temperatures of 75 ^oC, 150 ^oC, 250 ^oC, 350 ^oC, 450 ^oC and 550 ^oC were determined from the XRD patterns as presented in Figure. 4.1. Herein, the observed diffraction peaks of WO_3 nanoparticles (as seen in Figure. 4.1) at 2θ value of 22.72^o, 24.33^o, 28.17^o, 33.58^o, 36.57^o, 42.85^o, 46.46^o, 49.96^o, 55.51^o and 63.49^o correspond to the (001), (110), (200), (111), (201), (300), (002), (220), (221) and (401) planes of WO_3 (JCPDS File no. 033-1387).

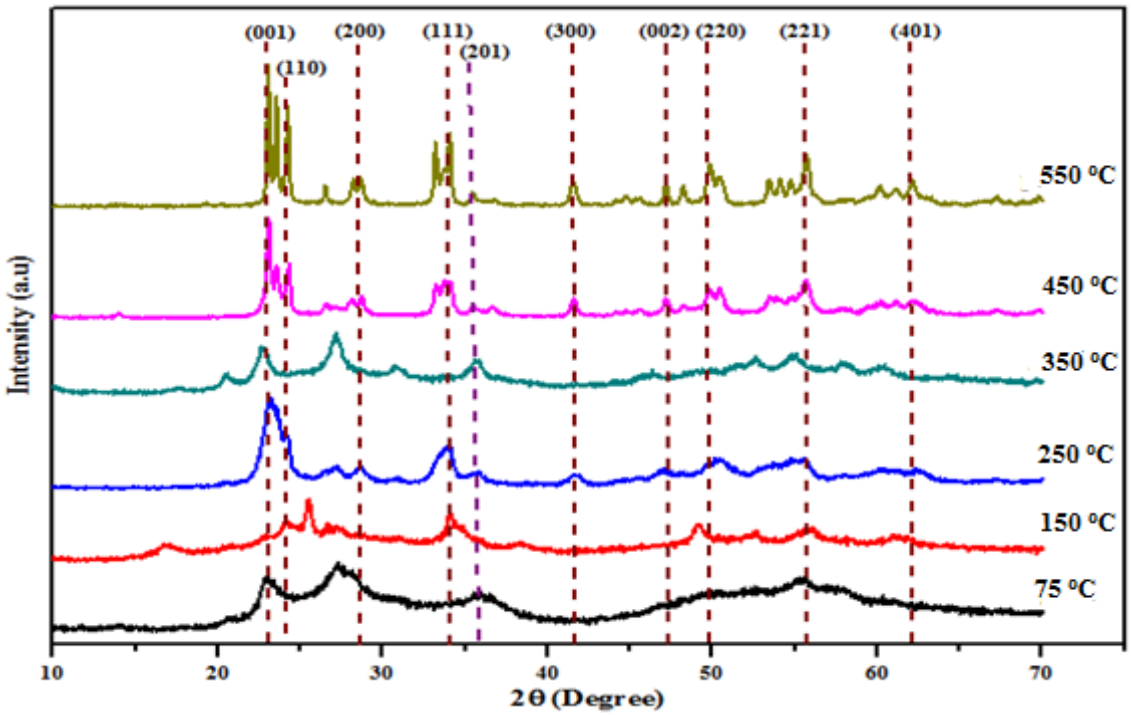

Figure 4.1: XRD results of WO_3 nanoparticles at different calcination temperature

The detected peaks are indexed to pure monoclinic crystalline phase of WO_3 with lattice constants of a = 7.30 Å and c = 3.70 Å. At lower temperatures (75 and 150 ^oC), the peaks were found to be broad and overlapping, indicating that oxide of tungsten calcined during

this stage is in amorphous state. However, at high temperature, the peaks became sharp and the crystallinity increased except at 350 ^{o}C. These observations are in harmony with the sol-gel synthesis of nano-crystalline WO_3 reported by Nagarjuna *et al.* (2017). The average crystallite size of 6.4 nm, 8.9 nm, 9 nm, 13.01 nm, 15.7 nm and 17.4 nm for WO_3 nanoparticles at 75 ^{o}C, 150 ^{o}C, 250 ^{o}C, 350 ^{o}C 450 ^{o}C and 550 ^{o}C, respectively was calculated by Debye Scherrer's equation as shown in Equation 4.1.

$$D = \frac{K\lambda}{\beta Cos\theta} \qquad (4.1)$$

where D is average crystallite size, K is Debye Scherrer's constant (0.94), λ is the Cukα radiation (0.154 nm), β is the full width half maximum (FWHM) of the peak and θ is Bragg's angle.

Upon increasing the temperature from 75 ^{o}C to 550 ^{o}C, the XRD results indicated that the grain size of nanoparticles increased. There was crystal growth along (001) and (201) planes between 250-350 ^{o}C and a further change in (100), (111) and (300) plane indexes from 450 ^{o}C to 550 ^{o}C. This could be attributed to the collapse of aggregate nanoparticles at higher temperature via inter and intra particle electrostatic attraction. The observed trend is similar to the findings of Lu *et al.* (2018) on the effect of sintering temperature on WO_3 prepared using sol-gel method. They noticed that the average grain size of pure WO_3 calcined at 300 ^{o}C, 500 ^{o}C and 700 ^{o}C were 235, 343 and 414 nm, respectively, indicating that calcination temperature enhanced its particle size. In this study, particle sizes of WO_3 calcined at different temperatures were found to be lower than the studies of Lu *et al.* (2018) and Tijani *et al.* (2019). The plausible reason could be linked to the method of synthesis, type of tungsten precursor and plant extract used as capping and stabilizing agent.

4.2.2 MgO nanoparticles

The XRD patterns of the MgO nanoparticles prepared via green route at pH 8, 9, 10 and 11 are show in Figure 4.2. It was noticed that the diffractions peaks at 2θ values of 36.80°, 42.82°, 62.17°, 74.52° and 78.44° correspond to the miller indices (hkl) (110), (200), (220), (311) and (111) planes matched with JCPDS Card No. 75-0447. This corresponds to pure faced centered cubic phase of as-synthesised MgO nanoparticles with average crystallite size of 10.01 nm at pH 8, 8.05 nm at pH 9, 9.54 nm at pH 10 and 9.41 nm at pH 11 using the Debye-Scherrer equation.

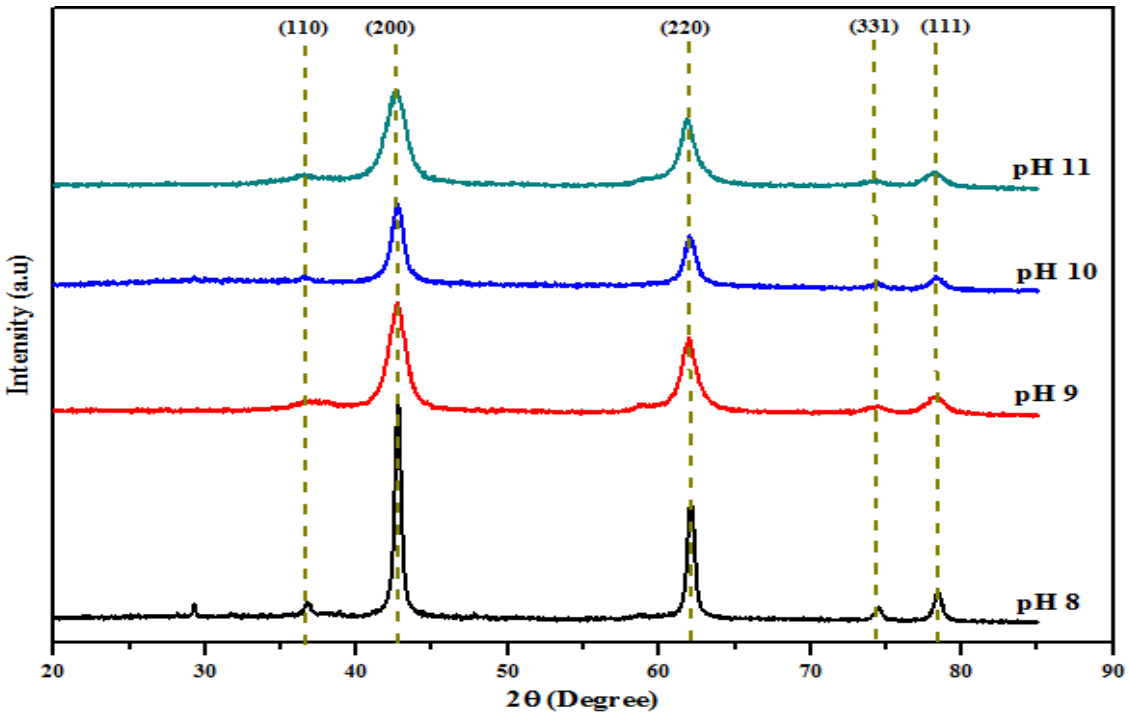

Figure 4.2: XRD analysis of MgO nanoparticles synthesised at different pH values

During the process of nanoparticles preparation using NaOH as a precipitating agent, conversion of magnesium salt used as precursor into MgO took place as represented in equation 4.1 to 4.3. Non-appearance of the diffraction peaks observed at 2θ value of 29.5° and 37.5° for MgO nanoparticles prepared at pH 9, 10 and 11 may be linked to the presence of more hydroxyl ion on the solution. The excessive amount of hydroxyl ions at these pH values aided the nucleation and growth of MgO nanoparticles compared to pH 8. All of the crystallite sizes obtained in this study were lower than 20.80 nm reported by

Fadil and Kareem (2020). It was noticed that as the pH of the nanoparticles increased, the width of the peaks increased leading to particle sizes reduction. The existence of sharp diffraction peaks in the XRD spectrum of MgO irrespective of pH confirmed the formation of crystalline MgO nanoparticles and solution pH did not distort the phase of MgO nanoparticles.

4.3 HRSEM/EDX Analysis

4.3.1 WO_3 nanoparticles

The structural morphologies of WO_3 nanoparticles calcined at 75 ^oC, 150 ^oC, 250 ^oC, 350 ^oC, 450 ^oC and 550 ^oC were observed using HRSEM and the corresponding micrographs are shown in Figure 4.3. HRSEM images of WO_3 calcined at 75 ^oC, 350 ^oC, 450 ^oC and 550 ^oC show that the nanoparticles appeared as discrete particles compared to HRSEM images of WO_3 nanoparticles calcined at 150 ^oC and 250 ^oC. During WO_3 calcination at 150 ^oC and 250 ^oC, they exhibit racemose structure with average diameters of 15.62±1.20 nm and 23.40±2.06 nm, respectively while HRSEM images of the synthesised WO_3 nanoparticles at 75 ^oC, 350 ^oC, 450 ^oC and 550 ^oC depict agglomerated spherical structure of size 12.08 nm, 21.90 nm, 23.36 nm and 24.10 nm, respectively. This shows that particle sizes increased with increasing calcination temperatures. According to the HRSEM images, noticeable changes were detected in morphology of WO_3 nanoparticles with increasing temperature. At higher temperature, agglomeration of particles leads to the formation of nucleation of nano-clusters and more particle growth. At this stage, agglomerated spherical shaped of nanoparticles accompanied the conventional mechanism of Ostwald ripening and oriented attachment (Mu *et al.* 2014). Mioduska *et al.* (2016) reported that the calcination temperature plays an important role in the morphological

formation of spherical WO_3 nanoparticles. Mioduska and colleagues observed an increased in crystallinity and crystal sizes of WO_3 nanoparticles due to increase in the calcination temperature. The calcination was found to be an important parameter in the final nano-structure which could lead to collapse of the mesoporous structure, agglomeration of the water-laden particles, and reduction in the surface area (Li *et al.*, 2019).

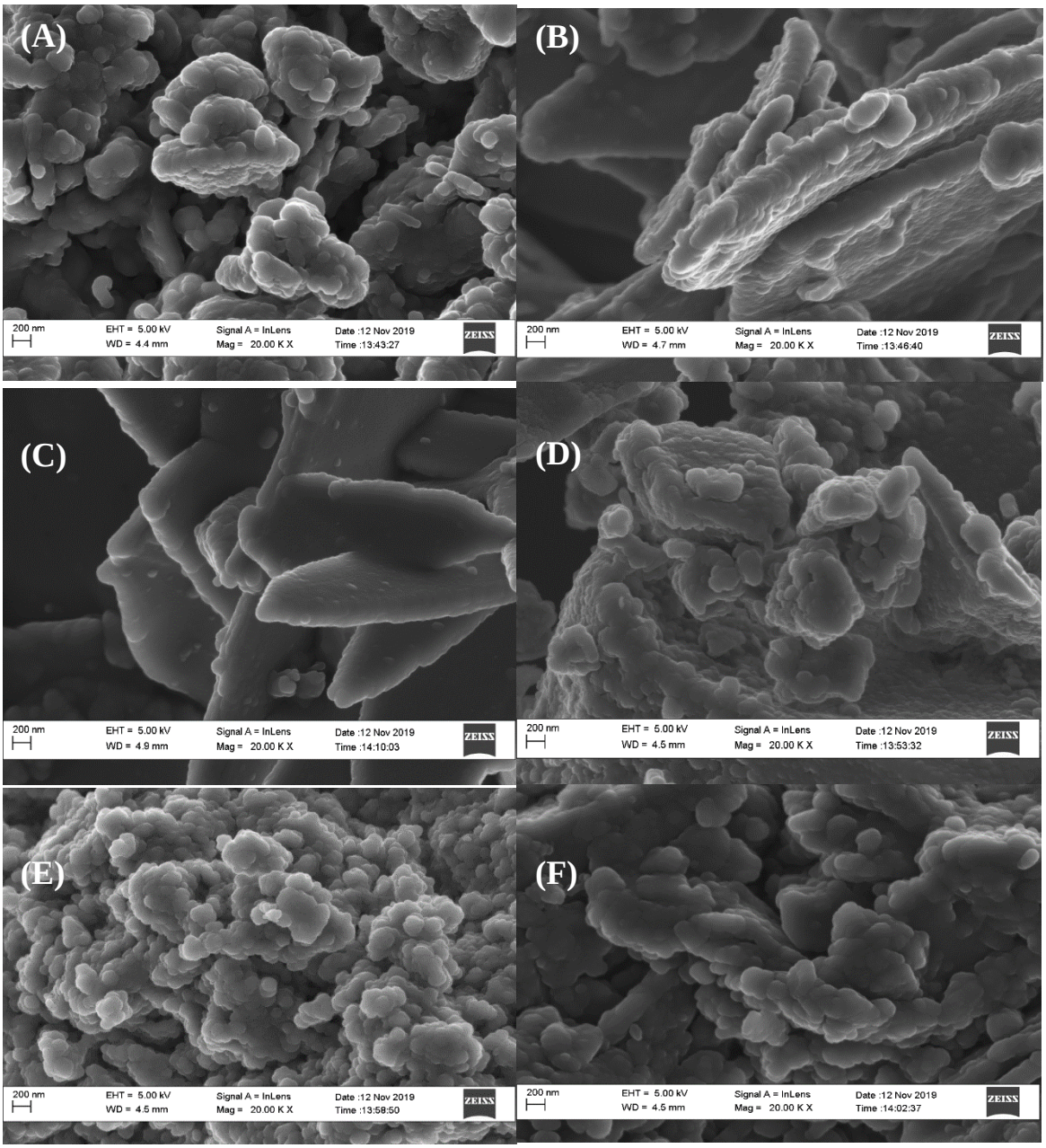

Figure 4.3: HRSEM images of WO_3 nanoparticles calcined at (A) 75 ^oC (B) 150 ^oC (C) 250 ^oC (D) 350 ^oC (E) 450 ^oC and (F) 550 ^oC)

The elemental composition were used to analyze the presence of W and O in the calcinated WO_3 nanoparticles (Figure 4.4). The W and O elements existed in the entire calcinated WO_3 nanoparticles. In particular, W is the major element in the WO_3 nanoparticles at 75 ^oC, 150 ^oC and 250 ^oC. At high calcination temperature above 250 ^oC, it was also observed that the solid state reaction between the mono oxide nanoparticles phase became reduced in W while O increased, thus this could be as a result of diffusional effect of W (0.062 nm) into O (0.14 nm) at the inner and outer shell of nanoparticles.

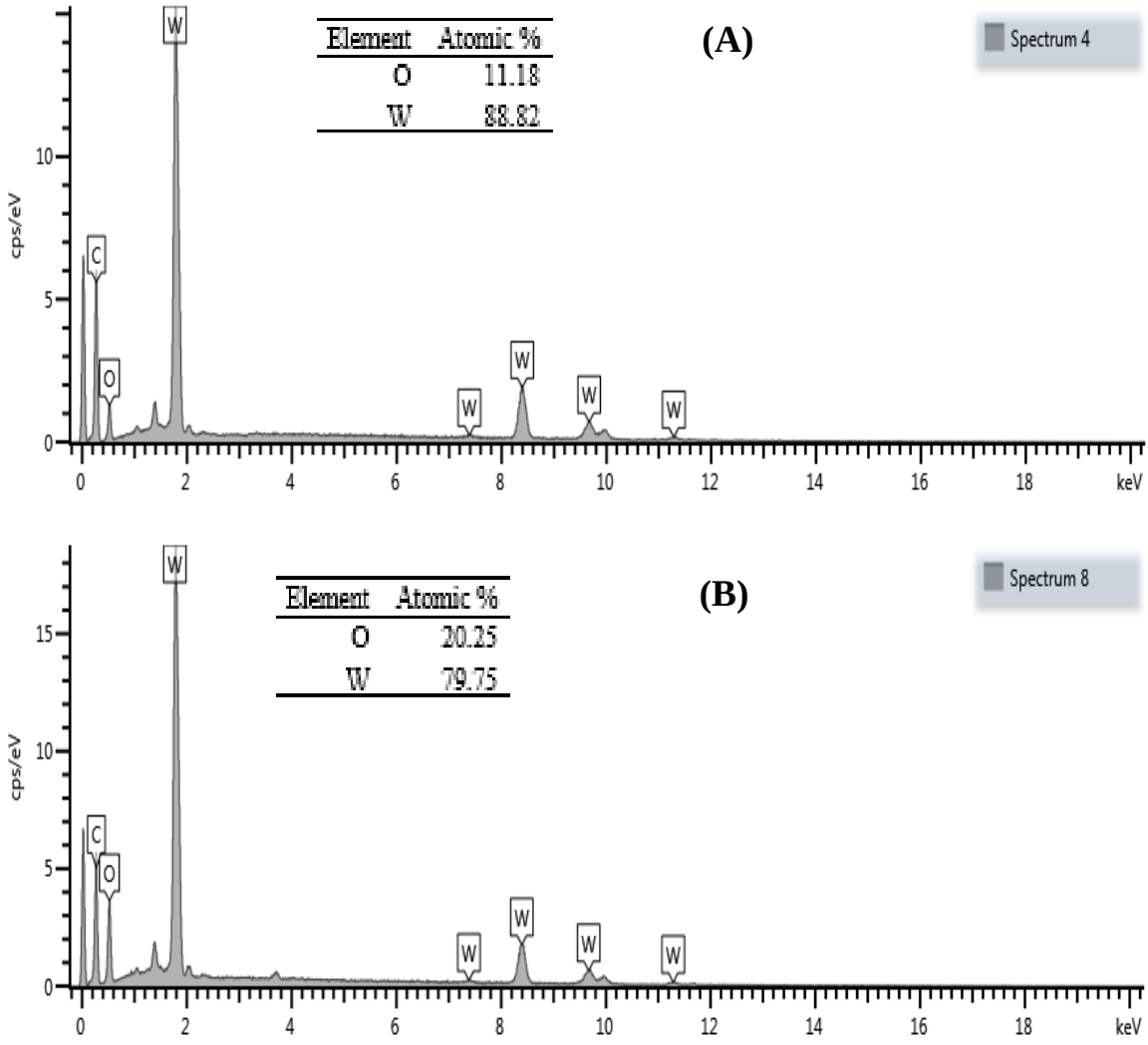

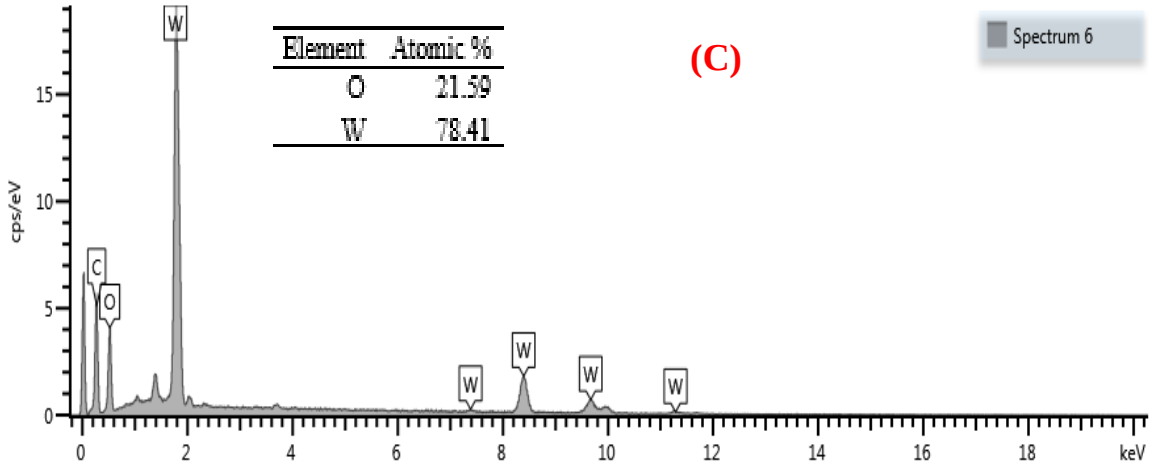
Element Atomic %
O 21.59
W 78.41
Spectrum 6
cps/eV
keV
C
O
W

(C)

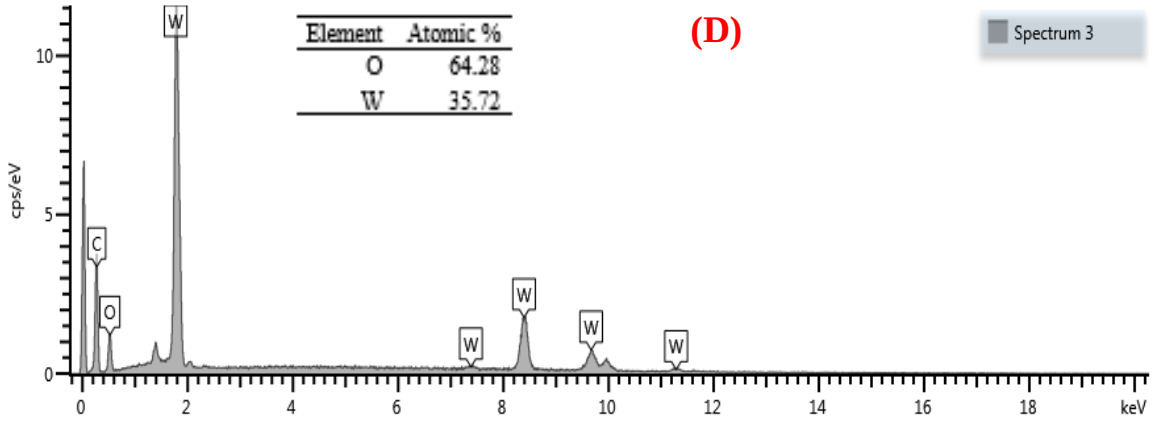
Element Atomic %
O 64.28
W 35.72
Spectrum 3
cps/eV
keV
C
O
W

(D)

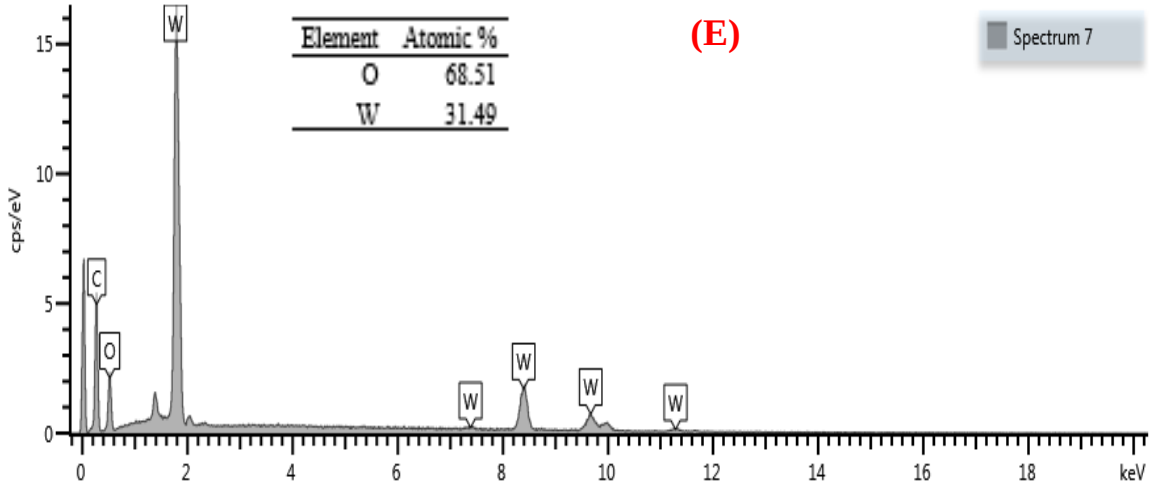
Element Atomic %
O 68.51
W 31.49
Spectrum 7
cps/eV
keV
C
O
W

(E)

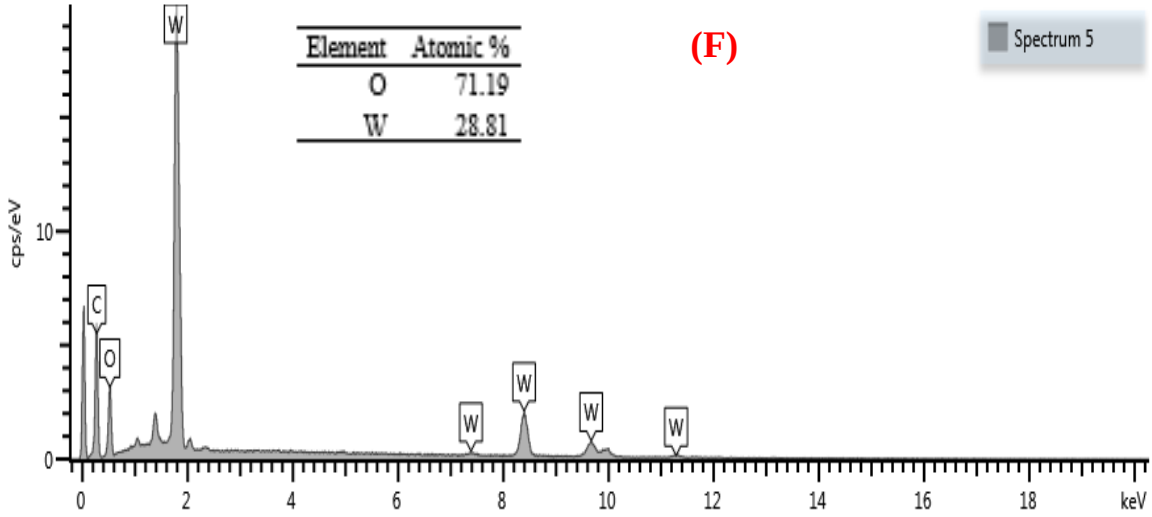

Figure 4.4: EDX results of synthesised WO_3 calcined at (A) 75 ^oC (B) 150 ^oC (C) 250 ^oC (D) 350 ^oC (E) 450 ^oC and (F) 550 ^oC

4.3.2 MgO nanoparticles

The HRSEM was used to investigate the surface morphologies of MgO nanoparticles synthesised at pH 8, 9, 10 and 11 and their corresponding images are shown in Figure 4.5 calcined at 450 ^oC.

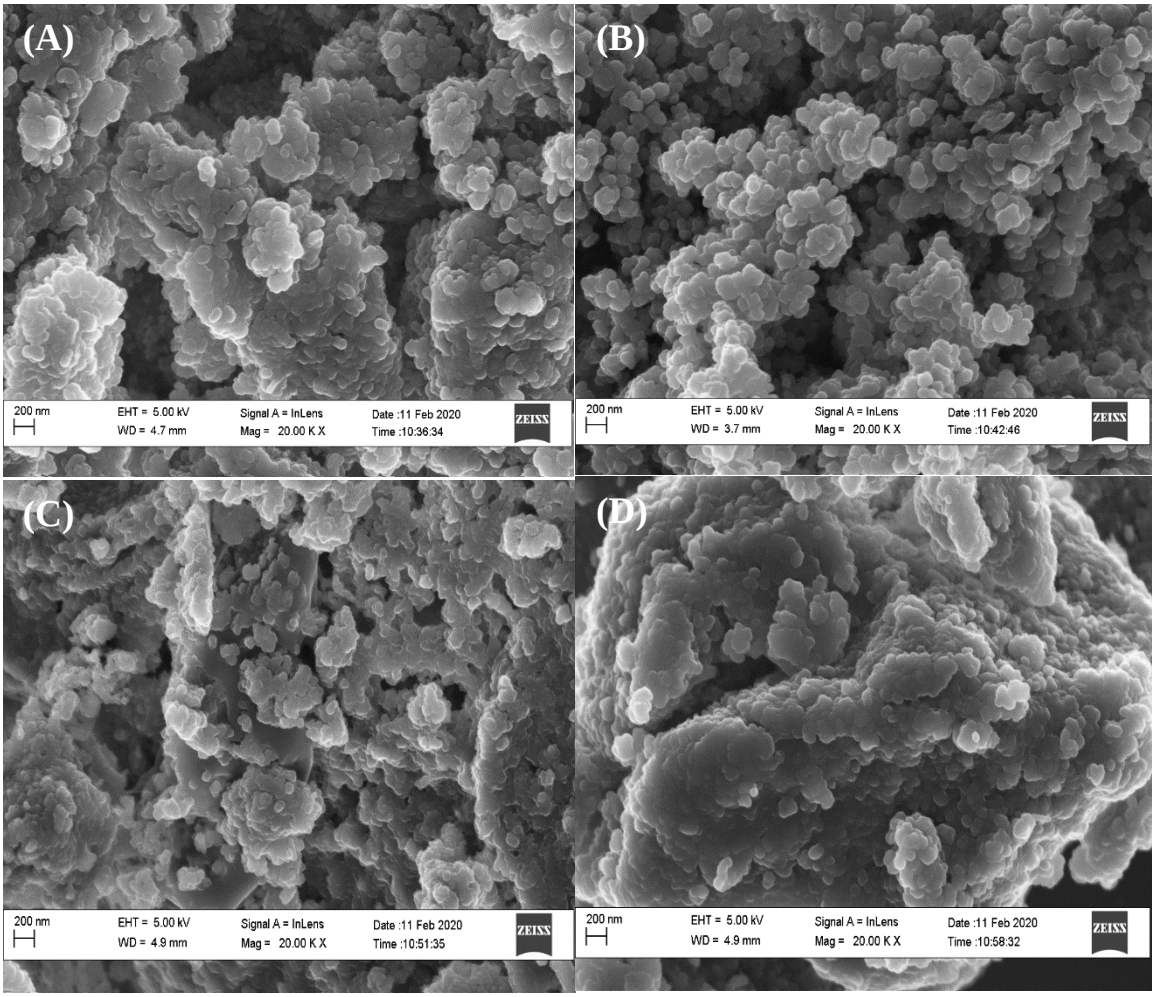

Figure 4.5: HRSEM results of synthesised MgO nanoparticles at (A) pH 8 (B) pH 9 (C) pH 10 (D) pH 11

It was observed that the as-synthesised nanoparticles are well distributed and agglomerated into clusters. The morphologies of the MgO nanoparticles at pH 8, 9, 10 and 11 show particles of average sizes 15.94, 14.50 nm, 11.90 and 9.36 nm, respectively, with high degree of agglomeration. Herein, the MgO nanoparticles prepared at pH 11 exhibited spherical particles-like shapes with porous network coupled with less agglomeration, and the particle size was in the range of 8.80 to 10.30 nm. This degree of agglomeration could be due to attractive forces between the phytochemical constituents in the plant extracts and magnesium salt precursor. In the basic solutions, the particles exhibited negative surface charge based on the interactions between the ions in the solutions and the positive

charges on the surface material (Cai *et al.*, 2018). The hydroxyl ions give rise to nucleation and growth of MgO and the formation of particles.

The EDX spectra revealed the presence of Mg, Cl, Na and O in MgO nanoparticles prepared at pH 8, 9 and 10 except for pH 11 as presented in Figure 4.6. The presence of Na and Cl which serve as an impurities could be from the precipitating agent and the plant extract which occurred from incomplete washing of the solution. It was confirmed from the EDX results that synthesised MgO nanoparticles at pH 11 is composed of Mg and O, indicating that the nanoparticles is pure MgO nanoparticles.

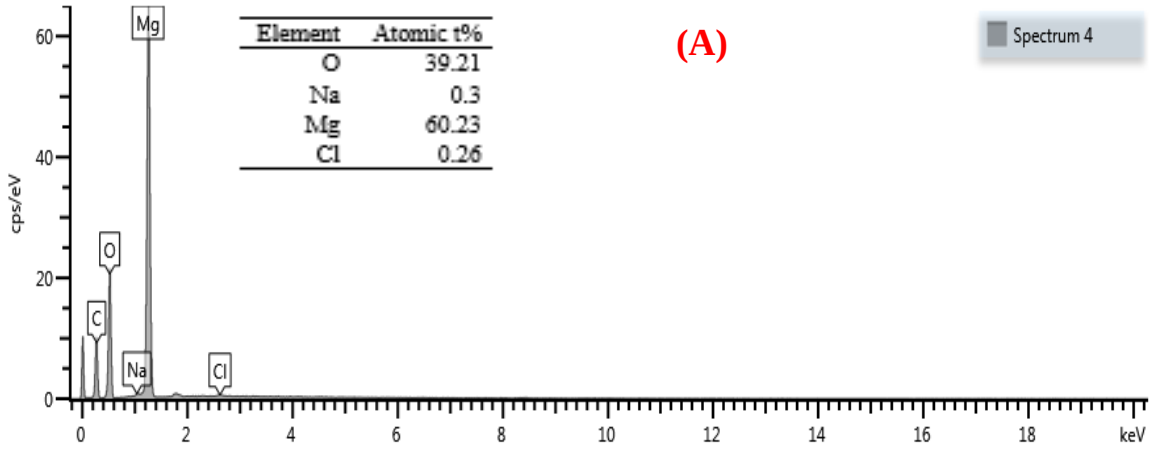

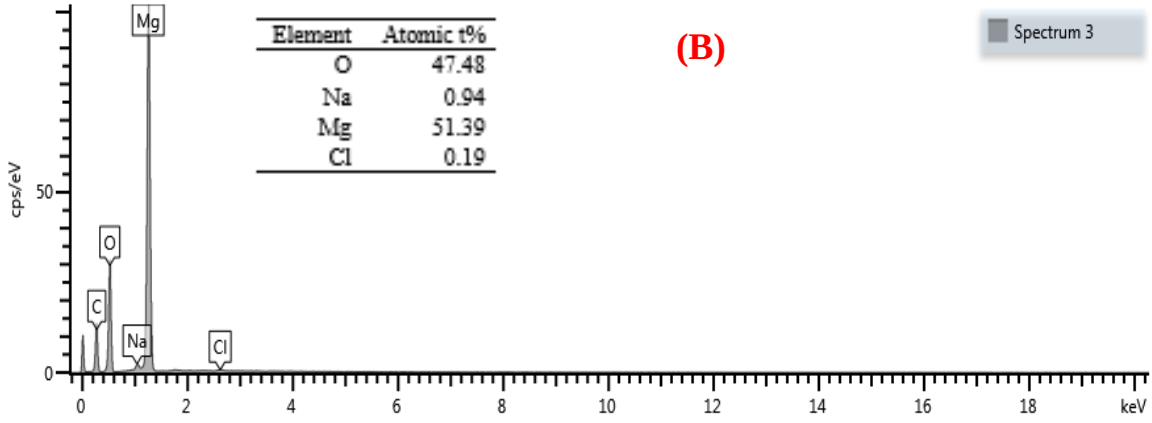

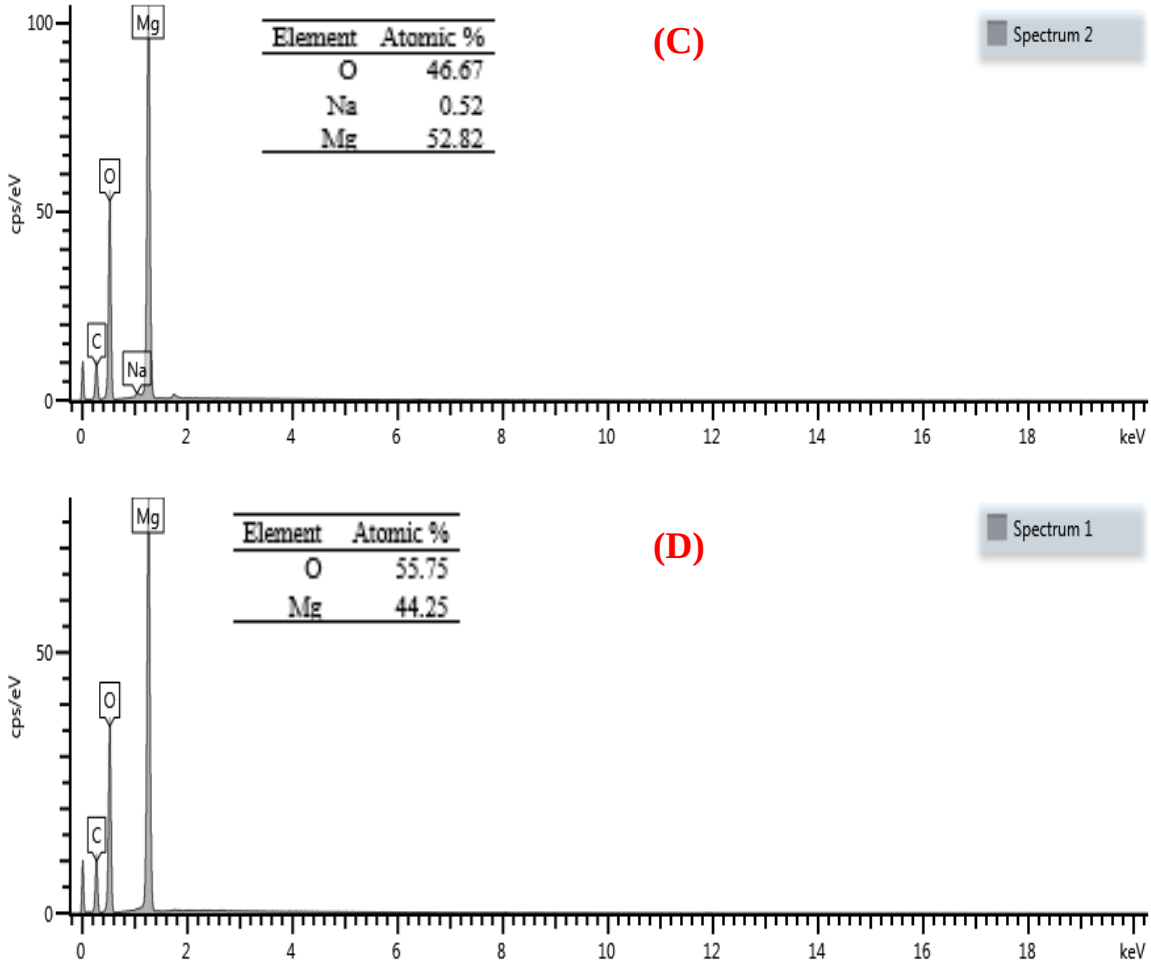

Figure 4.6: EDX analysis of synthesised MgO nanoparticles at pH (A) 8 (B) 9 (C) 10 and (D) 11

4.4 MgO/WO_3 Nanocomposites

4.4.1 XRD analysis

The XRD patterns of different ratios of as-prepared MgO/WO_3 nanocomposites calcined at 450 ^oC are shown in Figure 4.7. The Figure shows that the MgO and WO_3 peaks appeared in the samples after proportional mixture of the nanocomposites at different ratios. Figure 4.7 (a-d) designates the intense diffraction peaks of MgO at 2θ of 42.82^o, 62.17^o and 78.74^o that correspond to (200), (220) and (111) planes, respectively. Figure. 4.7 (e) revealed that high intensity of XRD of WO_3 nanoparticles compared to MgO nanoparticles in the composite sample. This indicates that the peak intensity of WO_3 rises and MgO reduces with increasing WO_3 concentration in the nanocomposites. Therefore,

the intensities of MgO and WO_3 nanoparticles are depended on the MgO:WO_3. It was cleared from the Figure 4.5 that the diffraction peaks of MgO and WO_3 appeared in the nanocomposites MgO/WO_3 are owing to the occurrence of MgO and WO_3. The average crystallite size of the nanoparticles in the samples varied as the temperature was increased. The average crystallite size of MgO and WO_3 of the mixed samples were 13.40 and 15.01 nm at 1:1, 10.62 and 13.70 nm at 2:1, 12.50 and 12.94 nm at 1:2, 9.47 and 11.42 nm at 4:1 and 15.08 and 13.02 nm at 1:4, respectively. The calcination temperature of 450 ^{o}C used in this study has an adequate thermal energy to activate the phase transformation between the MgO and WO_3 nanoparticles. The XRD results of all the nanocomposite samples revealed the diffraction peaks of $MgWO_4$, suggesting strong chemical reactions between MgO and WO_3 during the development of composites. The formation of magnesium tungstate ($MgWO_4$) can be explained as follows;

$$Na_2WO_4.2H_2O + 2HCl \rightarrow H_2WO_4.2H_2O + 2NaCl \quad (4.2)$$

$$2(H_2WO_4 2H_2O) \rightarrow 2WO_3 + 6H_2O \quad (4.3)$$

$$2Mg(NO_3)_2.6H_2O \rightarrow 2MgO + 4NO_2 + O_2 + 12H_2O \quad (4.4)$$

$$WO_3 + MgO \rightarrow MgWO_4 \quad (4.5)$$

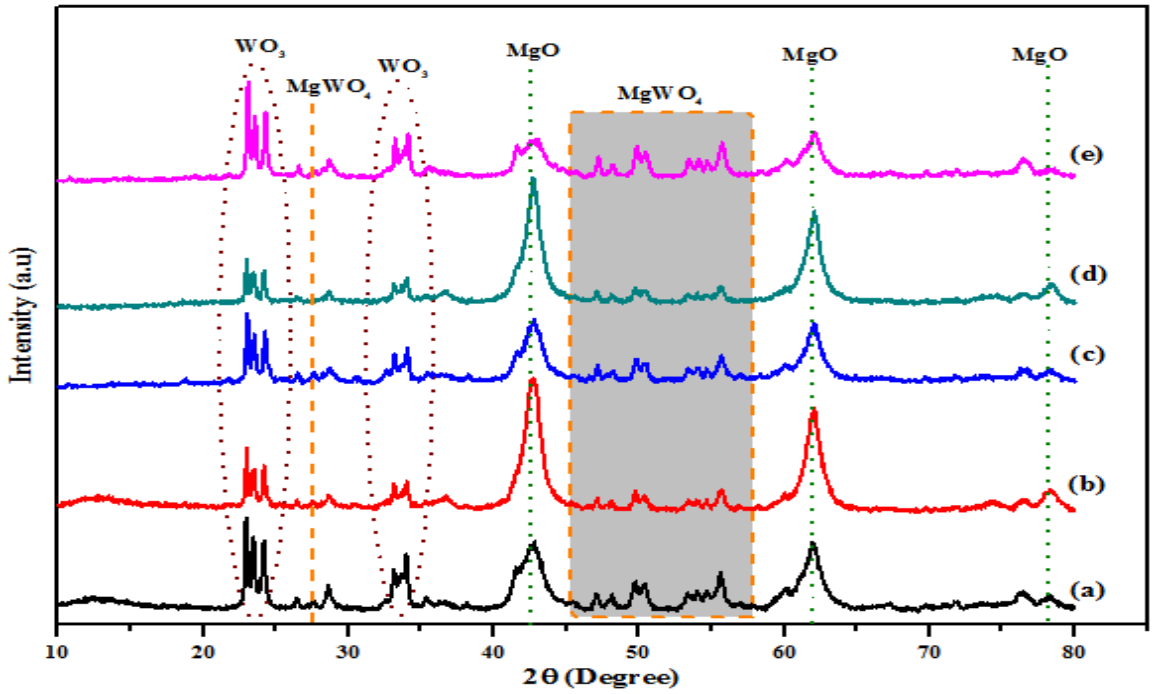

Figure 4.7: XRD results of synthesised MgO/WO_3 nanocomposites at (A) 1:1 (B) 2:1 (C) 1:2 (D) 4:1 and (E) 1:4

4.4.2 HRSEM analysis

Figure 4.8 presents HRSEM images of as-synthesised MgO/WO_3 nanocomposites using different ratios of MgO and WO_3. The MgO nanoparticles were agglomerated in the composites ratios except for MgO/WO_3 at 4:1 (as seen in Figure 4.8 d). When the mixing ratio of MgO/WO_3 is 4:1, MgO/WO_3 nanocomposites shape was flake-like. This shape confirmed the existence of MgO nanoparticles in the morphology of MgO/WO_3 nanocomposites changed the particles shape. It was revealed that the shape and size of MgO/WO_3 nanocomposites depend on the composition ratios. For instance, a dense and less agglomerated spherical particles were observed at different mixing ratio as presented in Figure 4.8. This can be linked to substitutional effect of oxygen by magnesium based on ionic radius mechanism. The ionic radius of Mg (0.072 nm) is lower than that of O (0.14 nm); thus Mg can easily diffuse onto the inner pore of W by displacing O with greater ionic radius. It could be concluded that this preparation technique was suitable for

the synthesis of MgO/WO_3 nanocomposites at different ratios to ensure the interaction between MgO and WO_3 nanoparticles.

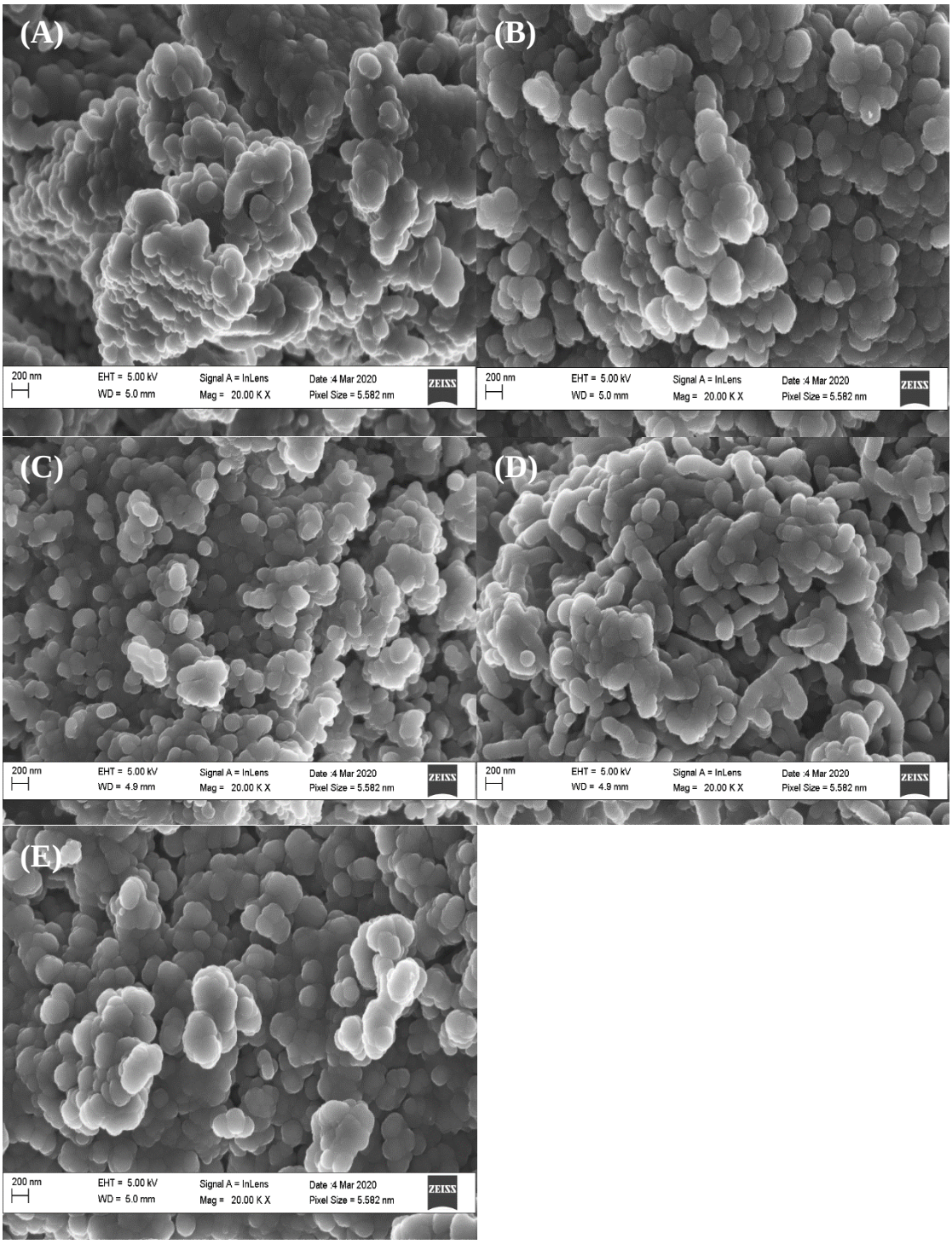

Figure 4.8: HRSEM results of synthesised MgO/WO_3 nanocomposites at (A) 1:1 (B) 2:1 (C) 1:2 (D) 4:1 and (E) 1:4

4.4.3 EDX analysis

Elemental distributions of the nanocomposites were examined using EDX analysis as depicted in Figure 4.9. The EDX results show the presence of three elements namely; Mg, W and O within MgO/WO_3. The analysis confirmed the presence of these elements in all MgO/WO_3 nanocomposite however with different atomic percentage due to the proportional mixture of MgO and WO_3 nanoparticles in the materials. The nanocomposites did not indicate any other peaks of other elements in the spectrum, suggesting the formation of pure MgO/WO_3.

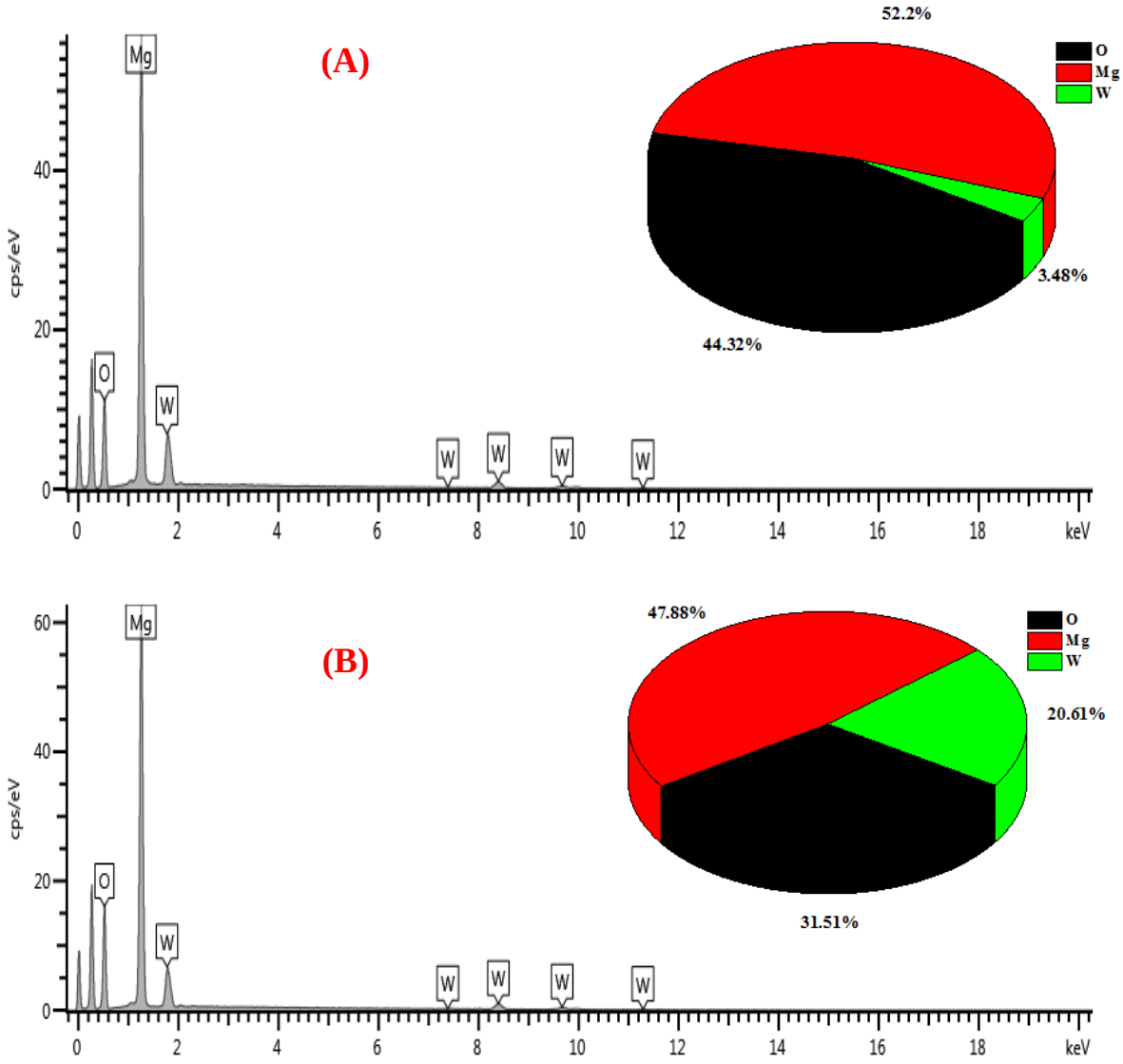

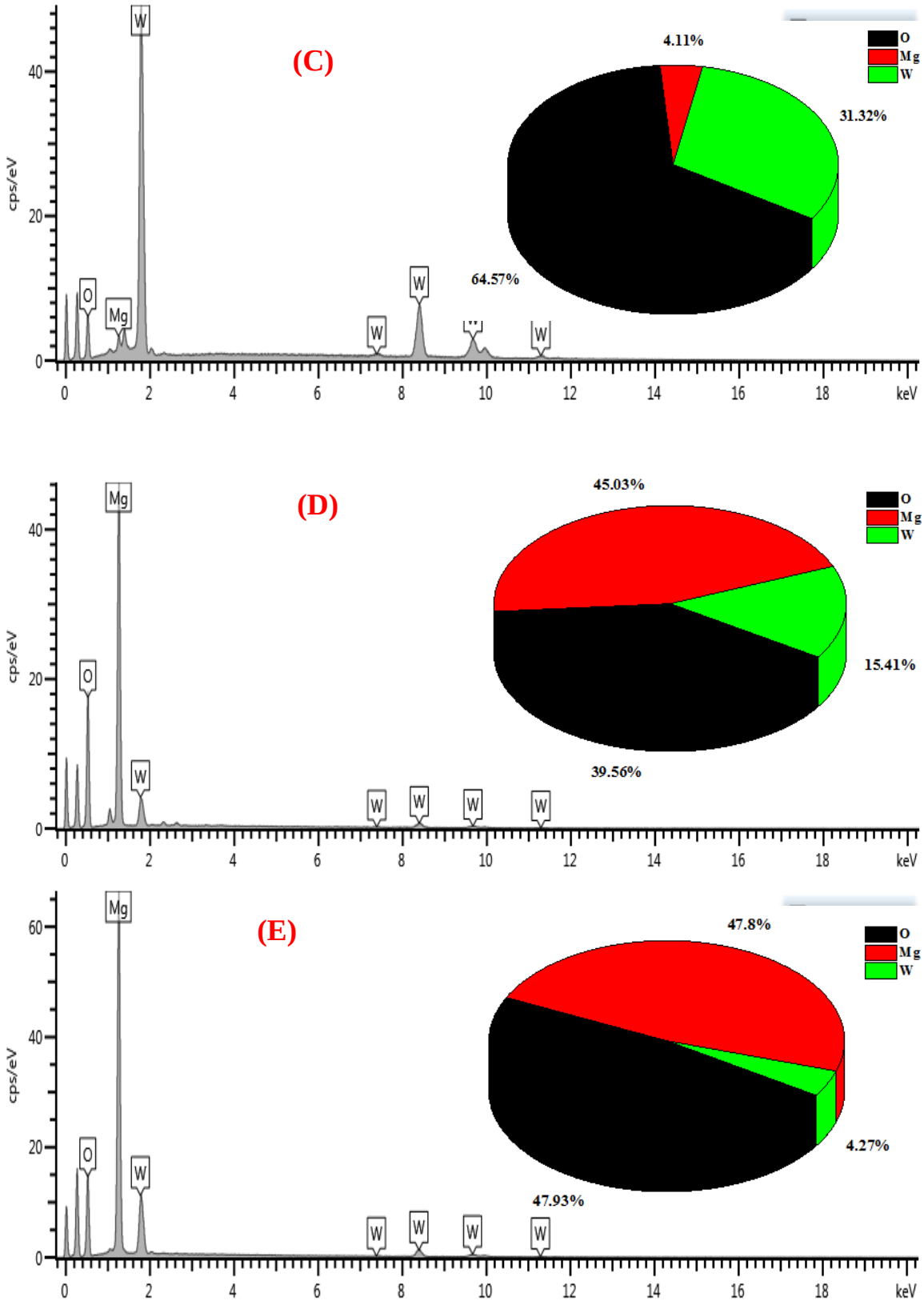

Figure 4.9: EDX analysis of synthesised MgO/WO_3 nanocomposites at (A) 1:1 (B) 2:1 (C) 1:2 (D) 4:1 and (E) 1:4

4.4.4 HRTEM analysis

Figure 4.10 shows low and high magnification HRTEM of MgO/WO_3 nanocomposites prepared at different ratios with their corresponding SAED patterns. The nanocomposites exhibited uneven surface distribution of the mixed nanoparticles and this could be attributed to the different mixing ratios of the nanoparticles. Figure 4.10 (b) demonstrated rod-like structure of MgO/WO_3 composites. The flake like structure covered the surface of the image, also forming an interface between the WO_3 flake like structure and MgO layer. In contrast, Figure 4.10 (c) revealed dark spots and spherical nanoscale bumps on the surface of the nanocomposites. This could be attributed to sputtering growth of binary oxide of the nanoparticles to form agglomerated like crystals on the heterogeneous surfaces. In Figure 4.10 (d and e), the growth of WO_3 nanostructures onto the surface of the MgO, nanoparticles caused homogenous crystal growth to form WO_3 on the MgO nanoparticles, vis-à-vis for MgO to WO_3 ratio. This study corresponds to the finding of Zhang *et al.* (2018) on formation of Cr_2O_3/WO_3 nanostructure. They inferred that MgO nanoparticles appeared on the surface of WO_3 nanostructures and the surface of WO_3 surface also synchronously increase with the increase of atom (W/Cr) at WO_3/Cr_2O_3 nanocomposites 10:1. The lattice spacing of MgO and WO_3 nanostructures appeared on Figure 4.10 (a-e), which agreed with the XRD results. Notably, dominance lattice fringes of 0.362 nm which correspond to the (200) plane of WO_3 and 0.25 nm for (111) crystallographic plane of MgO were found in Figure 4.8 (d and e), respectively which were in accordance of the XRD results. Similarly, Lei *et al.* (2018) noticed that after impregnation of ZnO on the surface of WO_3 nanoparticles, the WO_3 nanoparticles exhibited the crystallographic orientation and lattice spacing of the nanoparticles. The corresponding SAED patterns were shown on Figure 4.8 (a-e) for the nanocomposites, their concentric patterns indicate the polycrystalline nature of the MgO/WO_3 structure.

Furthermore, the diffraction rings were clear and sharp in Figure 4.10 (b) and (c), indicating the crystalline grains are tiny in Figure 4.8 (b) and evenly scattered in Figure 4.10 (e). The EDX results indicated that the as-prepared nanocomposites composed of O, Mg and W (Figure 4.9). This confirmed the pure formation of oxide of Mg and W. The atomic ratios of Mg and Win the EDX results varied depending on the mixing components (MgO and WO_3). Thus, this study confirmed the variations and successful incorporation of these nanoparticles to form bimetallic nanocomposites.

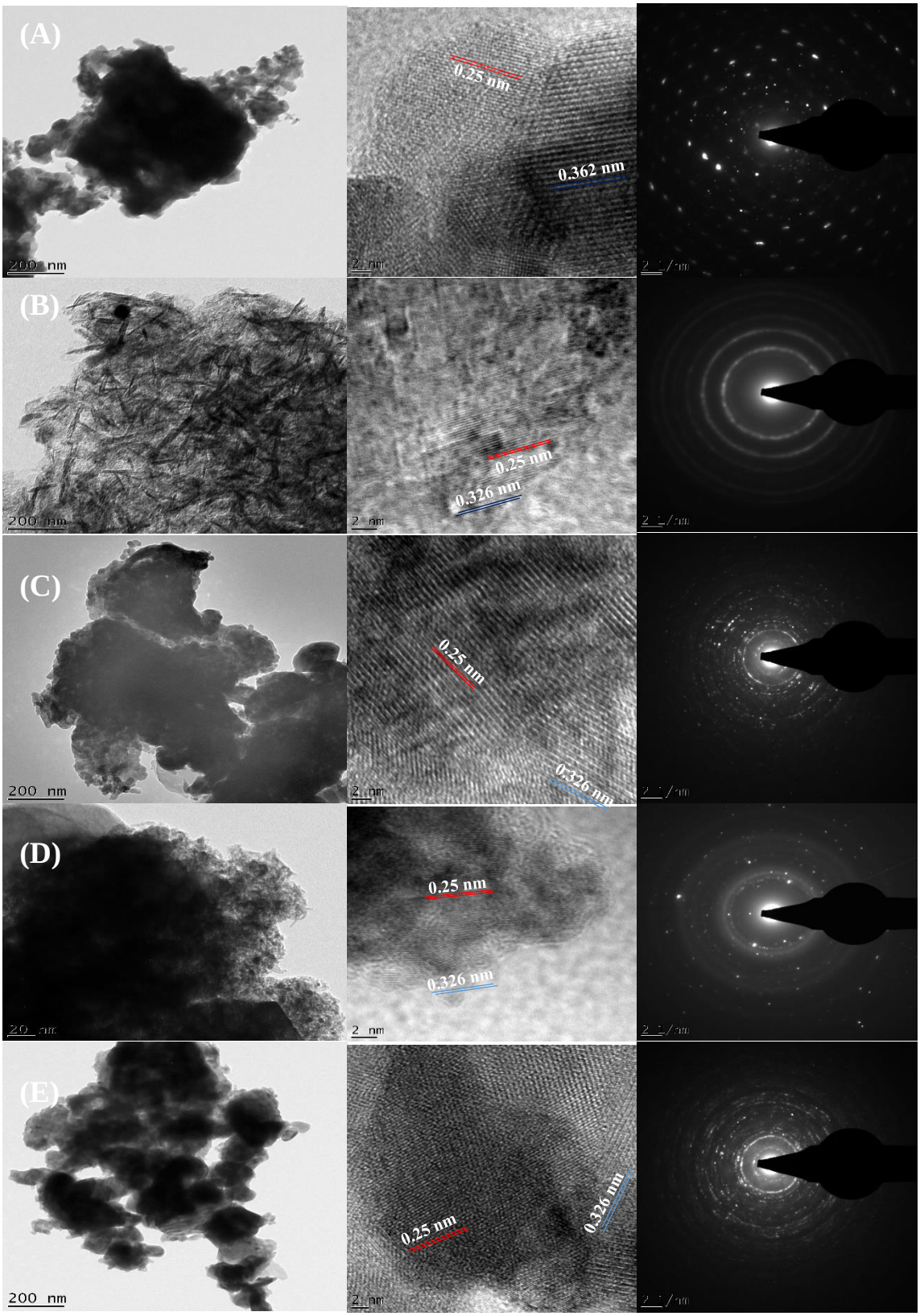

Figure 4.10: HRTEM images (low and high) magnification and SAED patterns of MgO/WO_3 at different mixing ratios (A) 1:1 (B) 1:2 (C) 2:1 (D) 4:1 and (E) 1:4

4.4.3 BET analysis

The N_2 adsorption-desorption isotherm results of WO_3 and MgO/WO_3 nanocomposites prepared at ratios 1:1, 2:1, 1:2, 1:4 and 4:1 are presented in Table 4.2. The specific surface areas of the MgO/WO_3 nanocomposites at 1:1, 1:2, 2:1, 1:4 and 4:1 were 29.97, 45.28, 60.42, 93.58, and 104.16 m^2/g, respectively. In this study, it was observed that the pore volume of MgO/WO_3 nanocomposite samples became reduced with an increase in surface area for the nanocomposites at ratios 1:4 (0.071 cc/g) and 4:1 (0.054 cc/g). The specific surface area of the nanocomposites in this study were higher than the specific area of MgO/Fe_3O_4 nanocomposite of 75.21 m^2/g reported by Abshirini *et al.* (2019). The difference in the surface area could be linked to amount of nanoparticles mixing ratio, calcination temperature with respect to time used in this study.

Table 4.2: The specific surface area, pore size and pore volume of MgO/WO_3 nanocomposites at different ratios

Adsorbent	Surface area (m^2/g)	Pore diameter (nm)	Pore volume (cc/g)
WO_3	22.49	2.42	0.130
MgO/WO_3 (1:1)	29.97	2.16	0.127
MgO/WO_3 (2:1)	60.42	2.14	0.105
MgO/WO_3 (1:2)	45.28	2.13	0.094
MgO/WO_3 (4:1)	104.16	2.11	0.054
MgO/WO_3 (1:4)	93.58	2.10	0.071

From Table 4.1, it was found that the BET specific surface area according to Barrette-Joyner-Halenda (BJH) method increase due to addition of MgO nanoparticles. This implies that the incorporated MgO nanoparticles widen the inner and outer pores of WO_3 nanoparticles. The whole nanocomposites correspond to mesoporous because the pore

sizes were greater than 2 nm but less than 50 nm. The pore size distributions of nanocomposites at 1:1, 2:1, 1:2, 1:4 and 4:1 were 2.16, 2.13, 2.14, 2.11 and 2.10 nm, respectively. The reduction in the pore sizes with an increase in MgO and WO_3 nanoparticles in the mixing validate the successful incorporation of these nanoparticles in the samples, thereby responsible for the increase in the surface area. The MgO/WO_3 nanocomposites (4:1) with the highest surface area could rapidly adsorbed pollutants on the surface of the nanoadsorbent, thereby promoting the adsorption process.

4.5 Physicochemical Properties of Local dyeing Wastewater

The results of the physicochemical analysis of local dyeing wastewater is shown in Table 4.3. High pH values in wastewater may increase the chance of solubilization of main essential elements if released in natural water bodies that affects the aquatic life. In Table 4.2, the pH value was found to be 9.98. The wastewater from the local dyeing Centre is alkaline in nature due to the presence of scouring and bleaching agents like chemicals such as sodium hypochlorite, sodium hydroxide, surfactants and sodium phosphate used during mercerizing of the fabric. The pH influences the plant growth, survival of aquatic animals and activity of useful microorganisms (Naik *et al.,* 2019). This parameter alter the soil permeability which results from underground water contamination. Colour has been prescribed as one of the major problems in the wastewater of the local dyeing industries which depends on the industrial processes. The colour of the wastewater as shown in Table 4.2 is blue measured using the UV-visible spectrometer at the wavelength of 625 nm was ascribed to Remazol brilliant blue R (RBBR) as presented in Figure. 4.11.

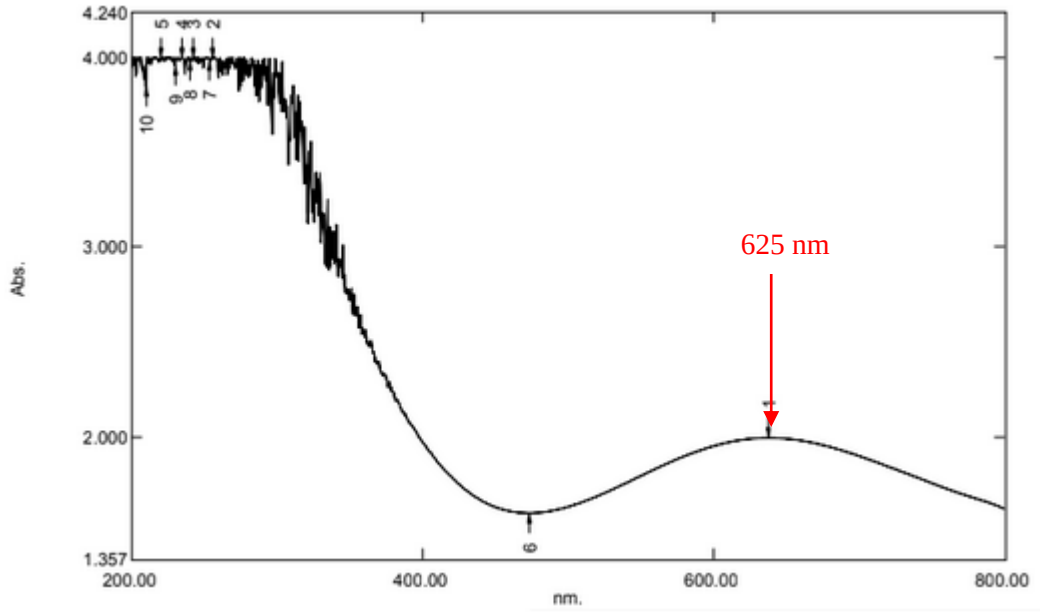

Figure 4.11: UV-vis absorption spectra of local dyeing wastewater

TDS measures the total organic and inorganic substances in water which includes the presence of soluble salts (Simeon *et al.*, 2019). These dissolved salts in water cause skin dehydration in animals and give a laxative effect and unpleasant mineral taste to water. TDS increases the osmotic pressure of soil water that leads to increase in respiration rate and reduction in the growth and yield of most plants (Hafez *et al.*, 2020). The wastewater showed a high level of TDS (1845.60 mg/dm^3) as presented in Table 4.2. The level of TDS could be as a result of the discharge of chemical agents used in various stages of the dyeing operation. TSS indicates the organic and mineral particles in wastewater that comprises carbonates, bicarbonates, chlorides, phosphates among others (Chockalingam *et al.*, 2019). The values of TSS value in the wastewater was 504.90 mg/dm^3 as depicted in Table 4.3. The concentration of TSS often influences sedimentation rates and turbidity in the wastewater, and increases the oxygen demand, pathogens and contaminants. The amount of chloride in dye wastewater has been linked to hydrochloric acid and chlorine gas used during bleaching, washing and disinfection processes in the dye processes. The level of chloride was of 6508.30 mg/dm^3 in the wastewater and that affect agricultural crops, kills the microorganisms in water, and increases corrosiveness with resultant

adverse health effects on humans. Chloride influences the level of electrical conductivity, alkalinity, TSS, TDS and sulphate in wastewater.

Table 4.3: Physicochemical Properties of Local Dyeing Wastewater

Parameter	Recorded value	WHO (2007)	NIS (2007)
Colour	Blue	-	-
Odour	Objectionable	-	-
pH	9.98±0.19	5-5.9	6.5-8.5
Chemical oxygen demand (COD) (mg/dm^3)	2016.80±0.45	250	60
Biological oxygen demand (BOD) (mg/dm^3)	750.20±0.80	30	30
Electrical conductivity (µS/cm)	1809.20±0.80	1200	1000
Chloride (mg/dm^3)	6508.30±1.20	1000	250
Nitrate (mg/dm^3)	98.60±0.30	-	-
Sulphate (mg/dm^3)	2067.80±0.70	-	-
Total suspended solids (TSS) (mg/dm^3)	504.90±0.80	60	150
Total dissolved solids (TDS) (mg/dm^3)	1845.60±0.23	-	500
Nitrite (mg/dm^3)	46.50±1.60	3	0.5
Total organic carbon (TOC) (%)	2.15±1.02	-	-
Copper (mg/dm^3)	6.03±0.48	0.1	1.0
Chromium (mg/dm^3)	8.15±0.31	2	0.05
Iron (mg/dm^3)	5.95±0.20	10	0.01

Key: WHO (World Health Organization, 2007); NIS (Nigerian Industrial Standard, 2007)

Total organic carbon was 2.15 mg/dm^3 in the dye wastewater as seen in Table 4.3. This pollutant measures the amount of organic substances in the wastewater sample. The quantity of the demand for oxygen of oxidizable pollutants in wastewater is described as COD. This parameter shows the level of toxicity and the presence of biological resistant

substances in water. According to Table 4.3, the amount of COD in the wastewater sample was 2016.80 mg/dm^3 (above the tolerance values of WHO, (2007) and NIS, (2007). The high value of COD in this study indicates the toxicity of the wastewater and it could be due to the presence of non-biodegradable dyeing chemicals, softeners and detergents used during the dyeing process (Pensupa *et al.,* 2017). The BOD measures the quantity of oxygen required by bacteria in the wastewater to breakdown the organic matter present. The dye wastewater sample collected showed BOD value of 750.20 mg/dm^3 as seen in Table 4.3. In this study, the recorded value of BOD was found to be higher than the WHO (2007) and NIS (2007) standards. The high values of BOD indicates the water pollution strength, indicating that less oxygen is available for the living organisms in the wastewater, thus leading to increasing the anaerobic properties of water. Thus, the wastewater needs to be treated to support the survival of aquatic living organisms.

4.6 Adsorption Studies

4.6.1 Effect of contact time

The influence of contact time is an essential optimizing factor used to determine the extent of adsorption process as it establish the plateau time for sorbent-sorbate system to reach equilibrium time. Therefore, the determination of contact time signifies the removal efficiency of sorbent in the sequesteration of pollutant in dyeing wastewater. The contact time for adsorption studies on MgO, WO_3 and MgO/WO_3 nanoadsorbents for the removal of selected heavy metals and other indicator parameters from dyeing wastewater were between for 0 to 20 min as depicted in Figure 4.12 to 4.17. In this study, the removal efficiencies of the pollutants rapidly increased during the initial concentration stage and the equilibrium times were reached. The maximum percentage removal of pollutants which justify the equilibrium time of Cu(II), Fe(II), Cr(VI), TOC, BOD and COD onto

MgO nanoadsorbent was 54.25, 59.51, 72.01, 55.75, 62.3 and 70.5 % at optimum time of 12, 12, 14, 10, 8 and 10 min, respectively. For WO_3 nanoadsorbent, the removal efficiency of Cu(II), Fe(II), Cr(VI), TOC, BOD and COD was 63.04, 64.20, 74.60, 64.20, 66.50 and 69.80 % at equilibrium time of 12, 12, 12, 12, 10 and 8 min, respectively. Also, the nanocomposites (MgO/WO_3) exhibited maximum adsorption removal of Cu (69.42 %), Fe (71.03 %), Cr (82.92 %), TOC (78.20 %), BOD (70.09 %) and COD (71.20 %) optimum time of 10, 14, 14, 12, 10 and 10 min, respectively. The rapid adsorption of these pollutants before equilibrium time could be attributed the large availability of vacant active sites on the nanoadsorbents surfaces. Thus, beyond the contact time increased, the number of vacant active sites on the nanoadsorbent reduced, leading to desorption stage. A similar finding was noticed by Chowdhury *et al.* (2016) and Madzokere and Karthigeyan (2017) on the removal of Pb(II) and Cu(II) on mesoporous MgO nanostructure and adsorption of Cu(II) by nano-MgO, respectively. They observed that initial rapid rate of adsorption was as a result of abundant sites on the surface of MgO nanoadsorbent. It was also observed that among selected metal ions adsorbed onto the nanoadsorbents, Cr(VI) ion had highest percentage removal rate from the dyeing wastewater. This behaviour could be associated to ionic radii of the interested removal of metal ions in the dyeing wastewater. The order of removal of heavy metals from local dyeing wastewater follow the order; Cr>Fe>Cu. In addition, it was observed that MgO/WO_3 nanoadsorbent showed the best removal efficacy of the whole pollutants from the wastewater, indicating that binary adsorbent is better the individual MgO and WO_3 nanoadsorbent. This could be attributed to the highest specific surface area exhibited by MgO/WO_3 nanocomposites.

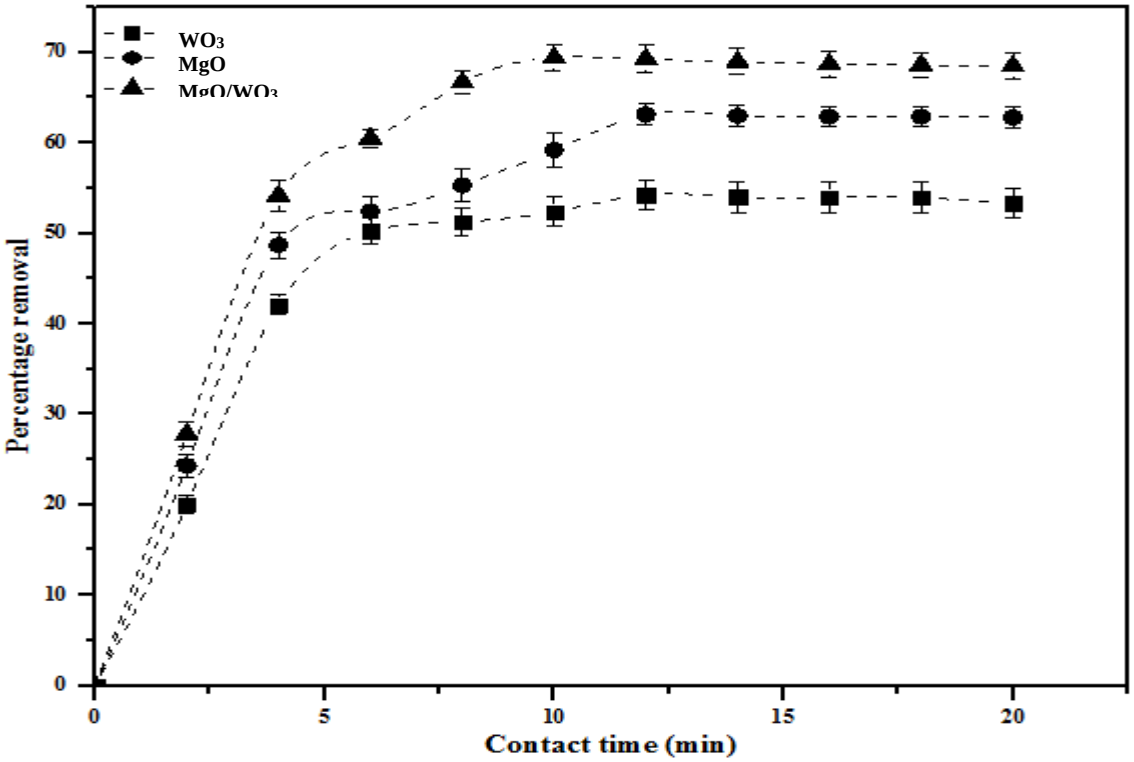

Figure 4.12: Effect of contact time on the removal of Cu(II) (dosage 0.1, agitation speed 150 rpm, temperature 28 ^{o}C)

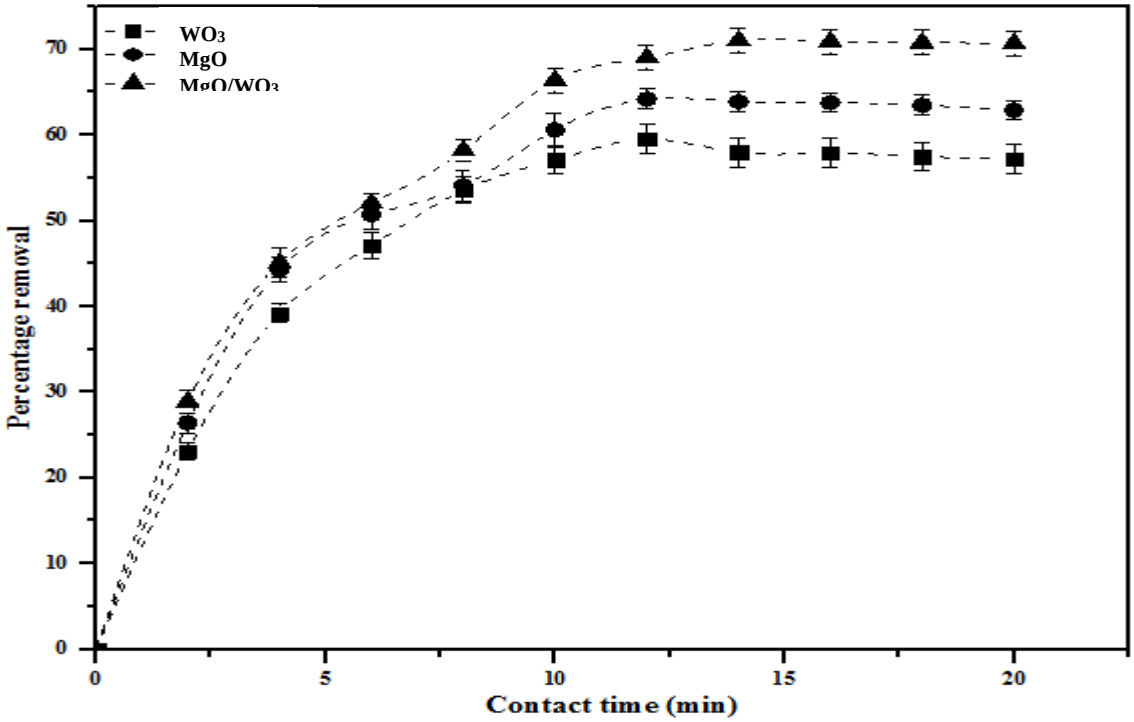

Figure 4.13: Effect of contact time on the removal of Fe(II) (dosage 0.1, agitation speed 150 rpm, temperature 28 ^{o}C)

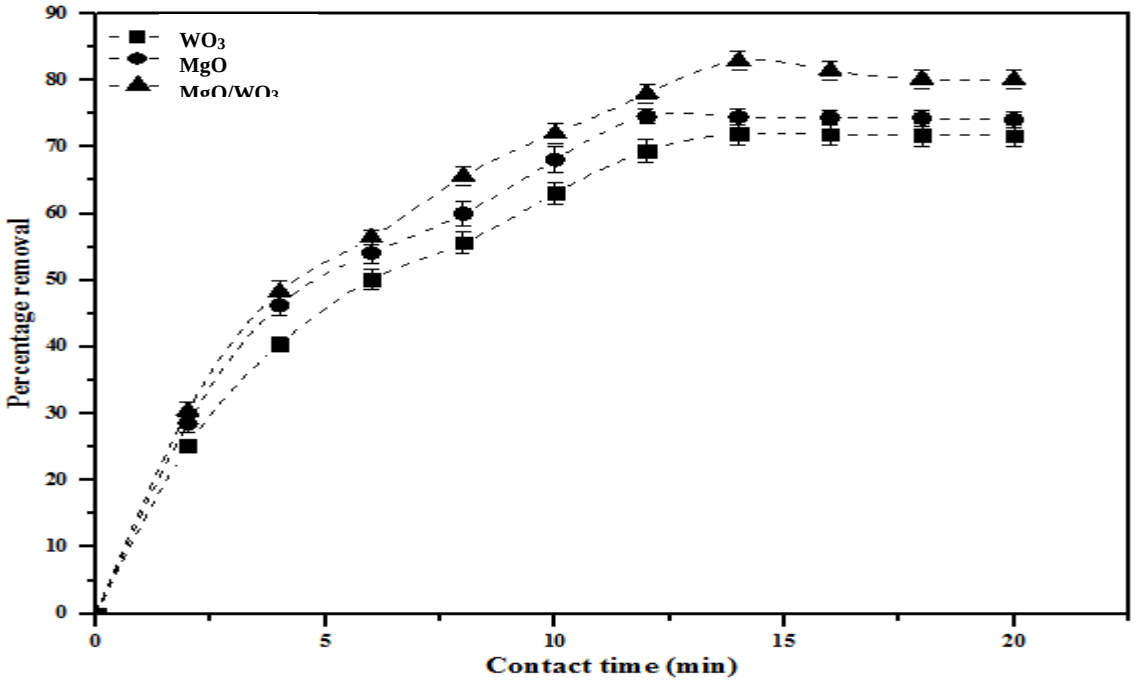

Figure 4.14: Effect of contact time on the removal of Cr(VI) (dosage 0.1, agitation speed 150 rpm, temperature 28 ^{o}C)

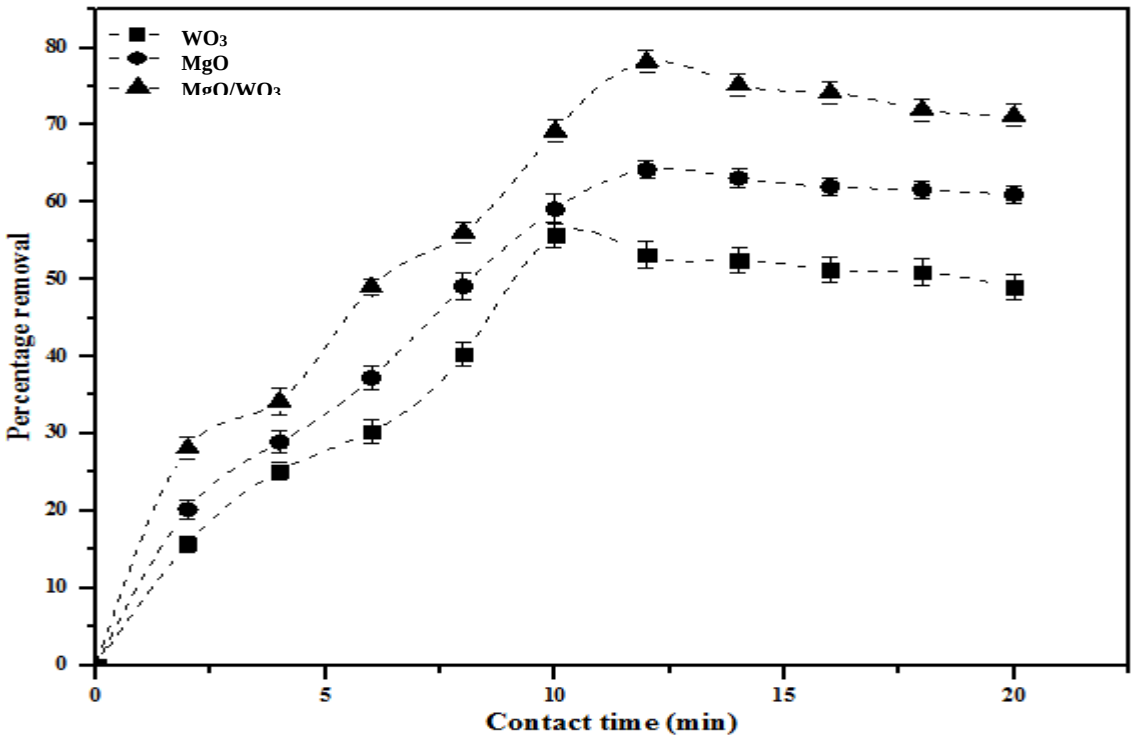

Figure 4.15: Effect of contact time on the removal of TOC (dosage 0.1, agitation speed 150 rpm, temperature 28 ^{o}C)

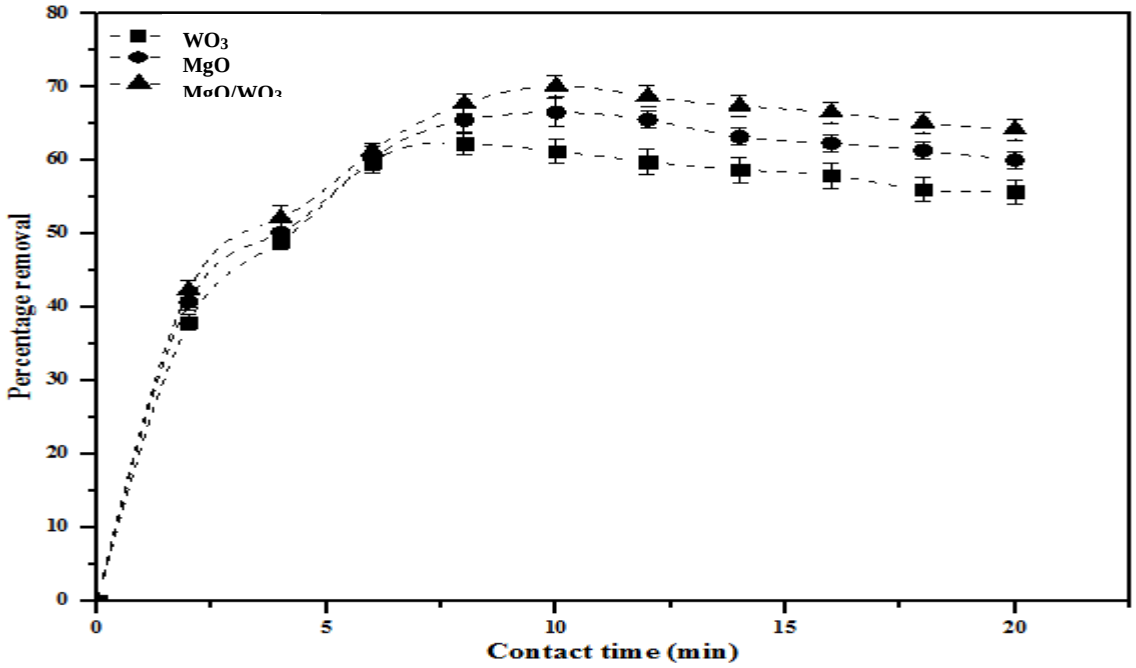

Figure 4.16: Effect of contact time on the reduction of BOD (dosage 0.1, agitation speed 150 rpm, temperature 28 ^{o}C)

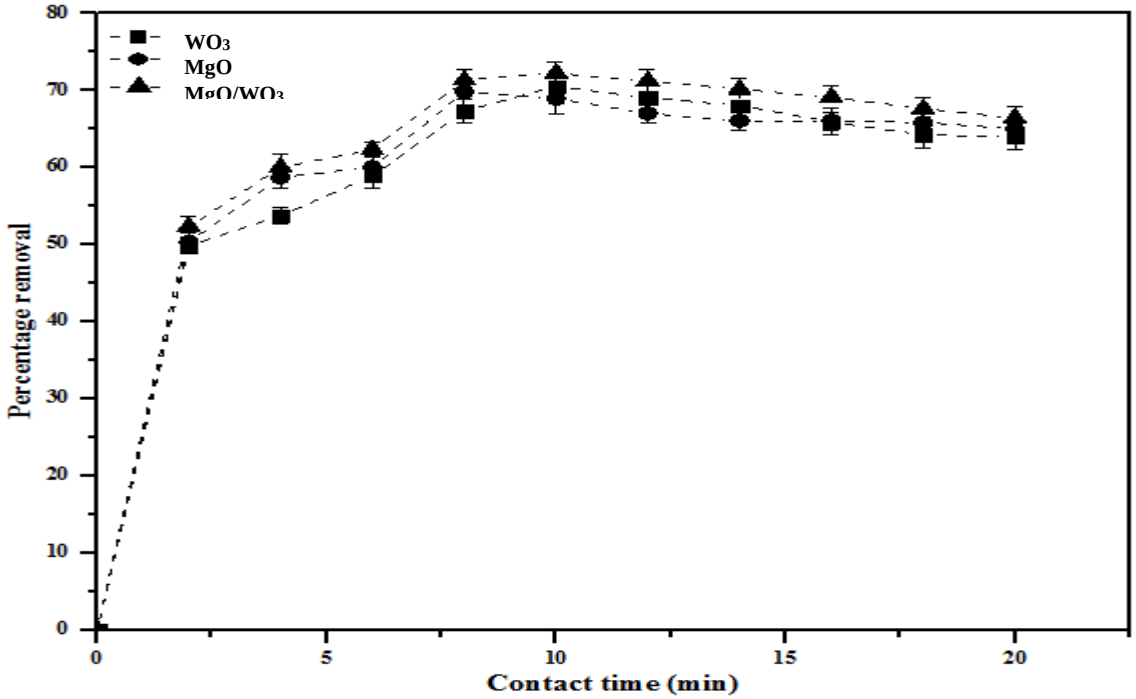

Figure 4.17: Effect of contact time on the reduction of COD (dosage 0.1, agitation speed 150 rpm, temperature 28 ^{o}C)

4.6.2 Effect of adsorbent dosage

The adsorbent dosage is a significant parameter in the removal of pollutants in wastewater and the effect of adsorbent dosage ranging from 0.2 to 1.0 g on the percentage removal of Cu(II), Cr(VI), Fe(II), TOC, BOD and COD are presented in Figure 4.18 to 4.23. As can be seen in the adsorption of pollutants, the removal percentage increased with increasing amount of nanoadsorbent dosage. The removal efficiencies of Cu(II) increased from 38.1 to 92.1 %, 43.2 to 84.6 % and 45.7 to 98.1 %; Fe(II) from 40.45 to 94.05 %, 44.6 to 99.5 % and 49.8 and 100 %; Cr(VI) from 42.5 to 95.1 %, 47.4 to 99.01, 51.03 to 100 %; TOC from 48.1 to 100 %, 56.9 to 100 % and 67.2 to 100 %; BOD from 39.01 to 90.23 %, 41.2 to 92.3 % and 45.35 to 94.2 % and COD from 37.5 to 85.3 %, 40.4 to 88.6 % and 43.2 to 89.8 % for WO_3, MgO and MgO/WO_3 nanoadsorbents, respectively At lower adsorbent dosage, the slow adsorption rate was enhanced by small surface adsorption site on the nanoadsorbent while the increase in adsorption with the dose could be attributed to availability of more adsorption sites and surface area of the material. Cr(VI) (0.052 nm) with the smallest ionic radius and highest electronegativity removed more than Cu(II) (0.073 nm) and Fe(II) (0.0645 nm) with higher ionic radii. Thus, the adsorption efficiency of the heavy metals followed this order: Cr > Fe >Cu. This implies that the smaller the ionic radii, the faster the rate of diffusion and removal efficiency. This is in agreement with the reports of Egbosiuba *et al.* (2020) and Mustapha *et al.* (2021). The author emphasized that the differences in adsorption was based on ionic radii, suggesting that large ionic radii induced fast on the adsorption site due to steric and overcrowding on the surface of adsorbent than metal with smaller ionic radius.

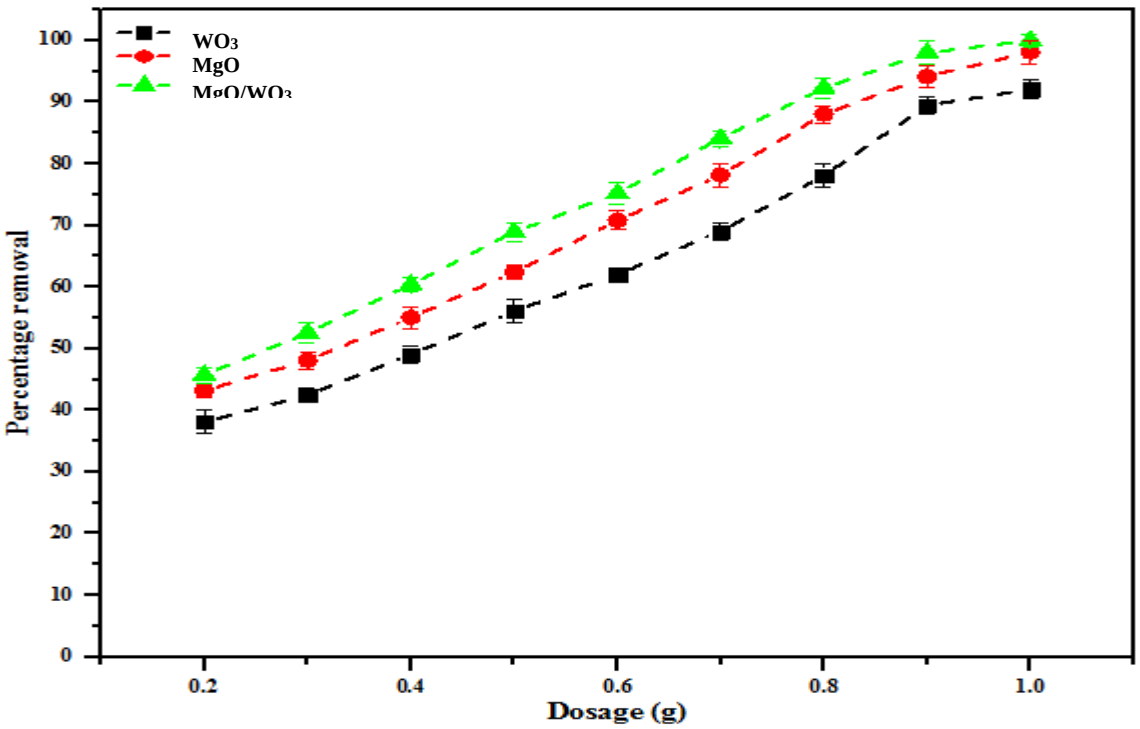

Figure 4.18: Effect of dosage on the removal of Cu(II) (optimum time, agitation speed 150 rpm, temperature 28 ^{o}C)

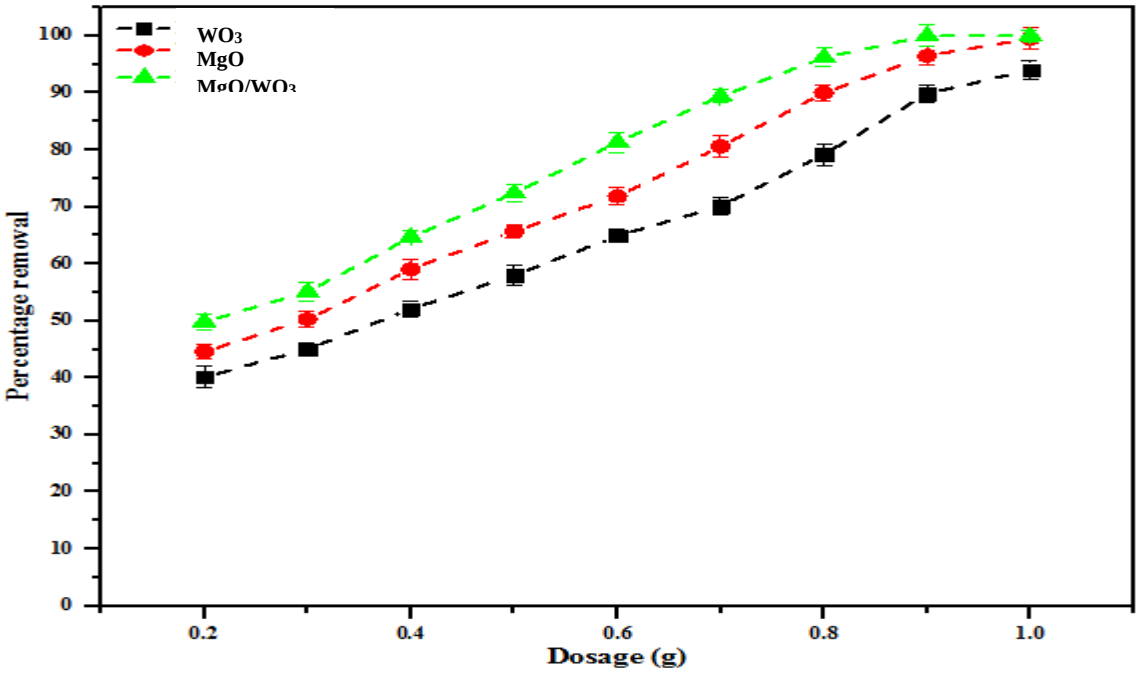

Figure 4.19: Effect of dosage on the removal of Fe(II) (optimum time, agitation speed 150 rpm, temperature 28 ^{o}C)

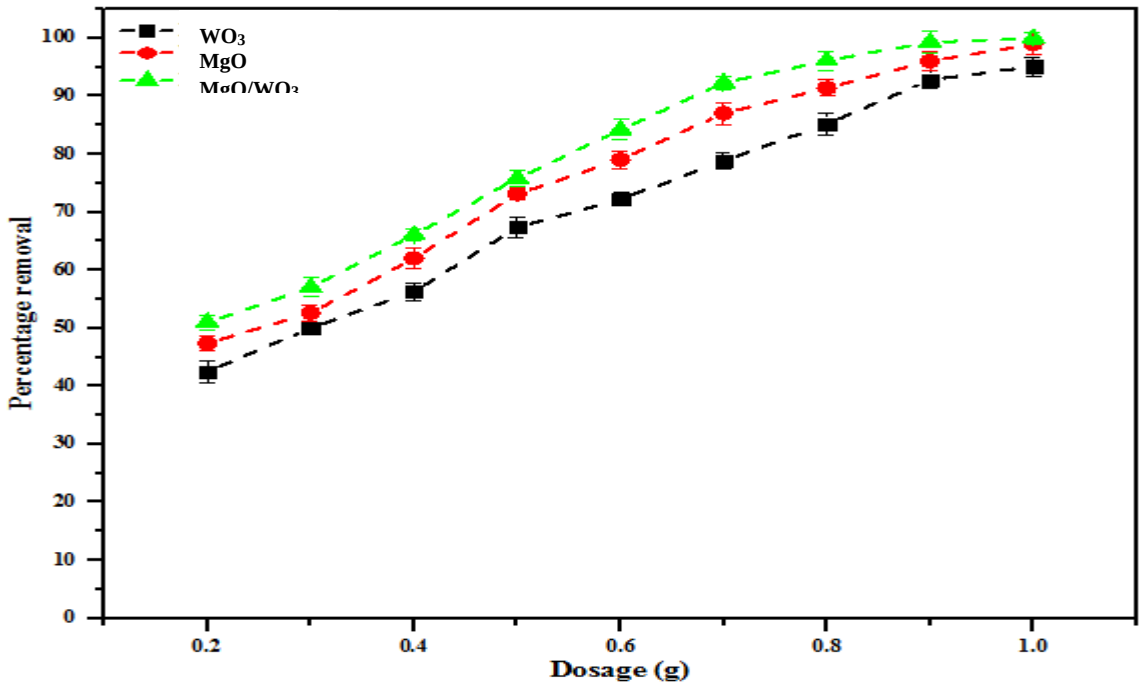

Figure 4.20: Effect of dosage on the removal of Cr(VI) (optimum time, agitation speed 150 rpm, temperature 28 ^{o}C)

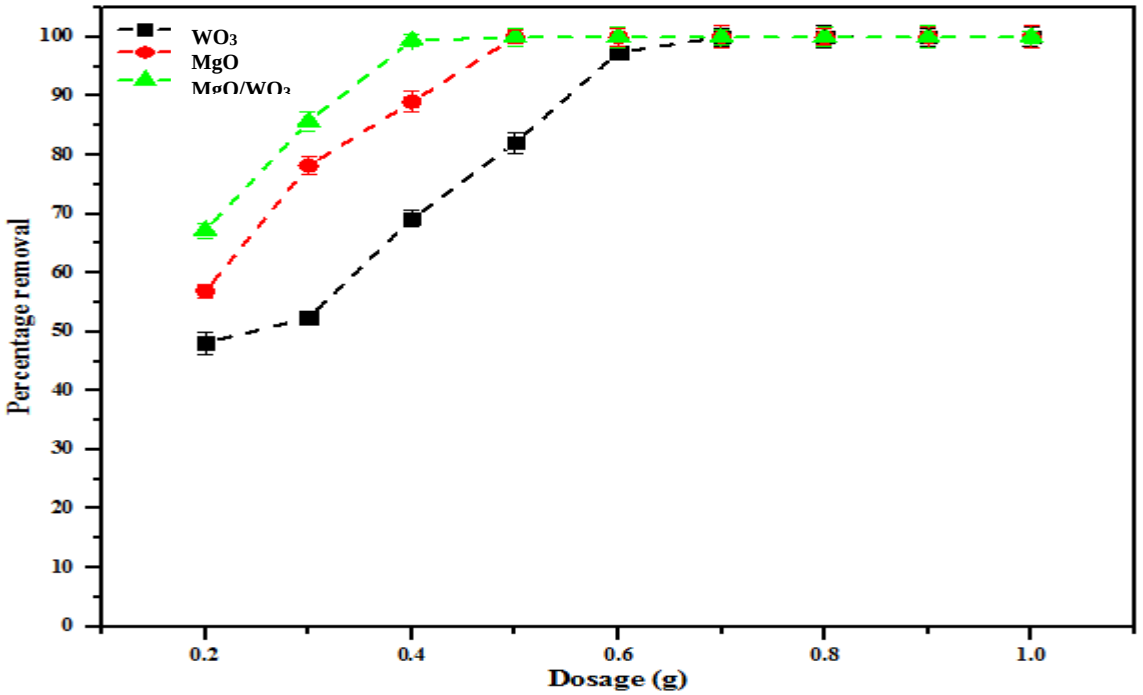

Figure 4.21: Effect of dosage on the removal of TOC (optimum time, agitation speed 150 rpm, temperature 28 ^{o}C)

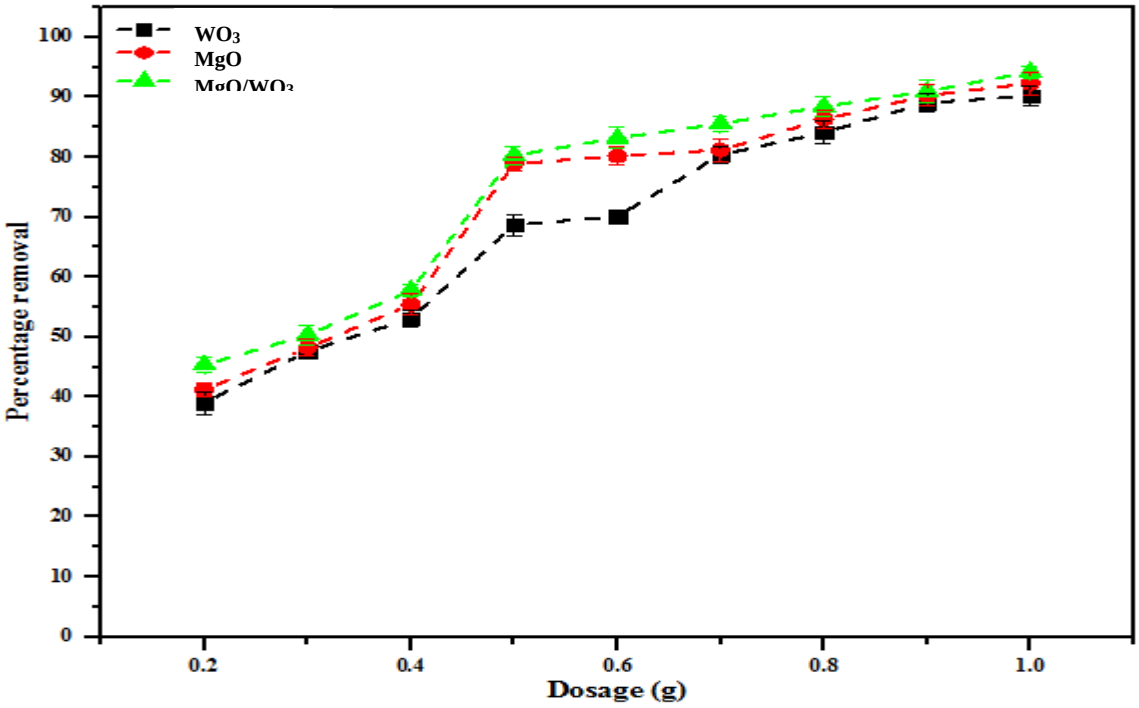

Figure 4.22: Effect of dosage on the reduction of BOD (optimum time, agitation speed 150 rpm, temperature 28 ^{o}C)

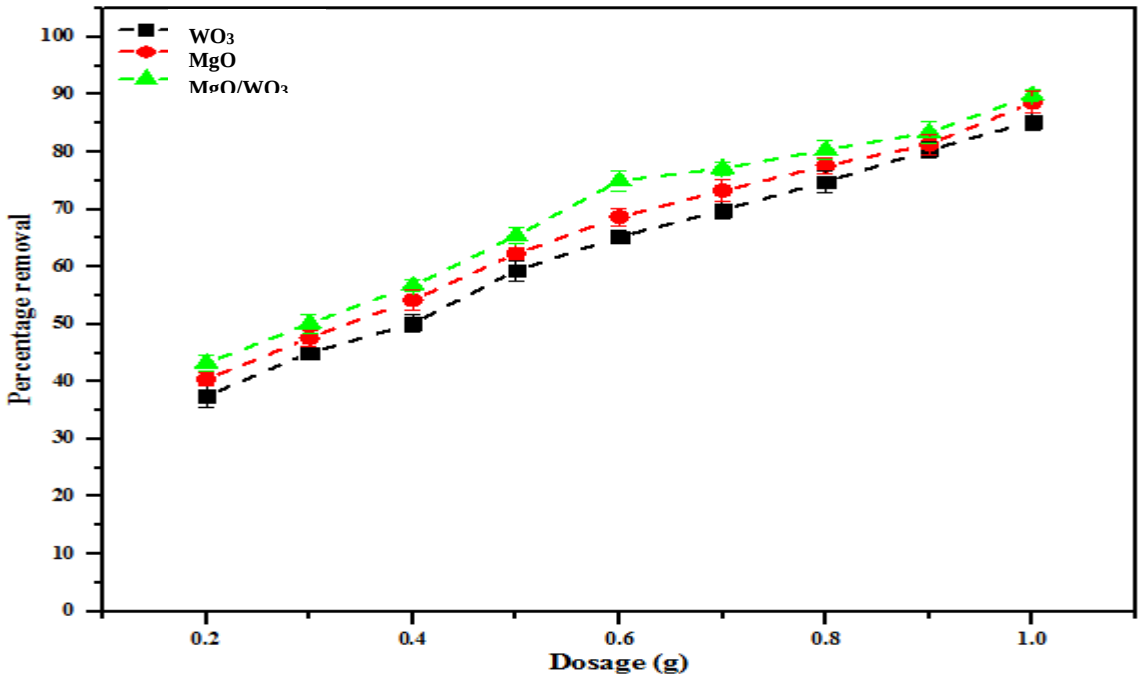

Figure 4.23: Effect of dosage on the reduction of COD (optimum time, agitation speed 150 rpm, temperature 28 ^{o}C)

4.6.3 Effect of temperature

Temperature affects the equilibrium capacity of adsorbent for adsorbate and also enhances diffusion rate of adsorbate across the external boundary and internal pores of adsorbent particles (Miyah *et al.*, 2018). The effect of temperature on the removal of Cu(II), Fe(II), Cr(VI), TOC, BOD and COD at temperature ranging from 30 to 80 ^{o}C were investigated and presented in Figure 4.24 to 4.29. It was observed that adsorption of heavy metals and other indicators parameters increased with temperature. This could be due to increase mobility of the adsorbate onto the active sites of the nanoadsorbents. This statement affirms the endothermic behaviour of the adsorbed pollutants on MgO, WO_3 and MgO/WO_3 nanoadsorbents. Similar observation reported by Kumar *et al. (*2018). In addition, high temperature increases the movement of pollutants from the bulk of the liquid to the surface of the nanoadsorbent, thus leading to the formation of new effective sites. This effect could be characterised as chemical reaction or bond formation between the adsorbent and the adsorbate. The complete removal of Fe(II), Cu(II) and Cr(VI) were not achieved including TOC, BOD and COD. This is due to the strong competition for the adsorption sites by other interfering TDS and ions in the aqueous media with metal ions and indicator parameters of interest, respectively.

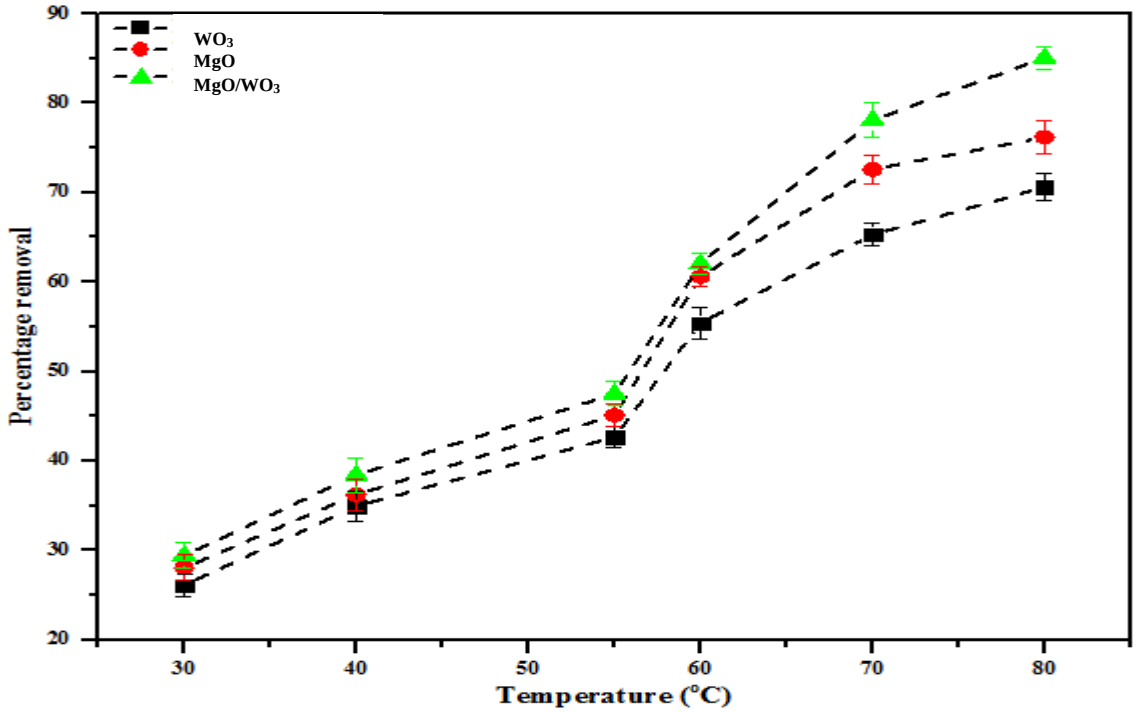

Figure 4.24: Effect of temperature on the removal of Cu(II) (optimum time, dosage 0.1 g, agitation speed 150 rpm)

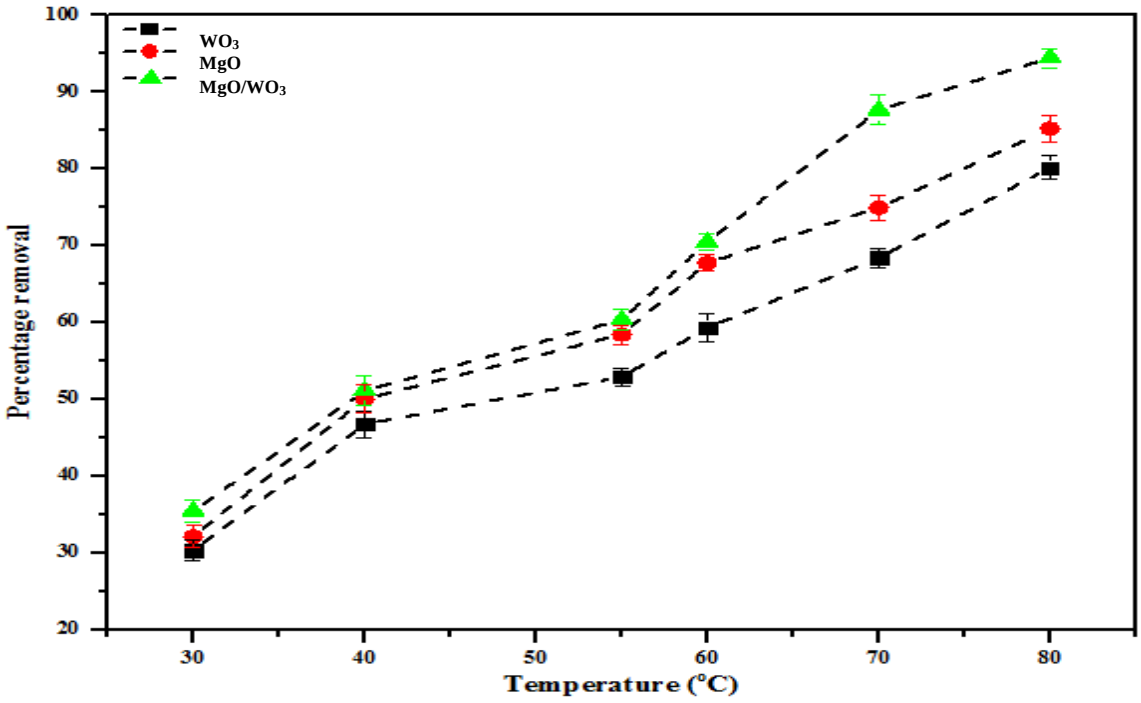

Figure 4.25: Effect of temperature on the removal of Fe(II) (optimum time, dosage 0.1 g, agitation speed 150 rpm)

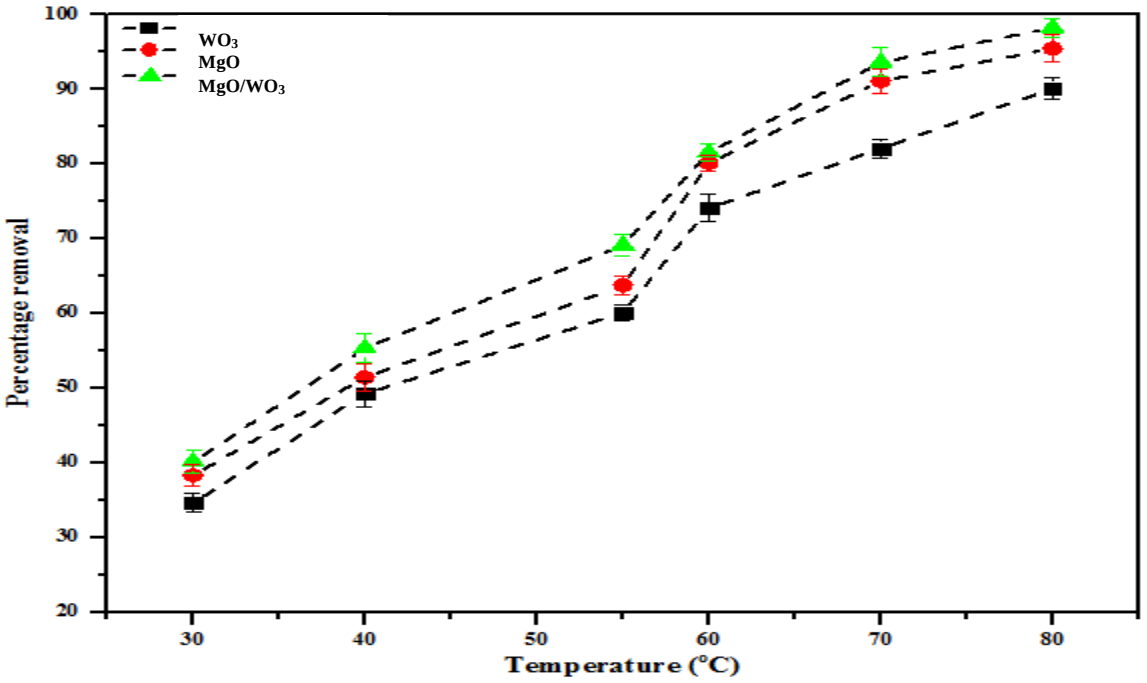

Figure 4.26: Effect of temperature on the removal of Cr(VI) (optimum time, dosage 0.1 g, agitation speed 150 rpm)

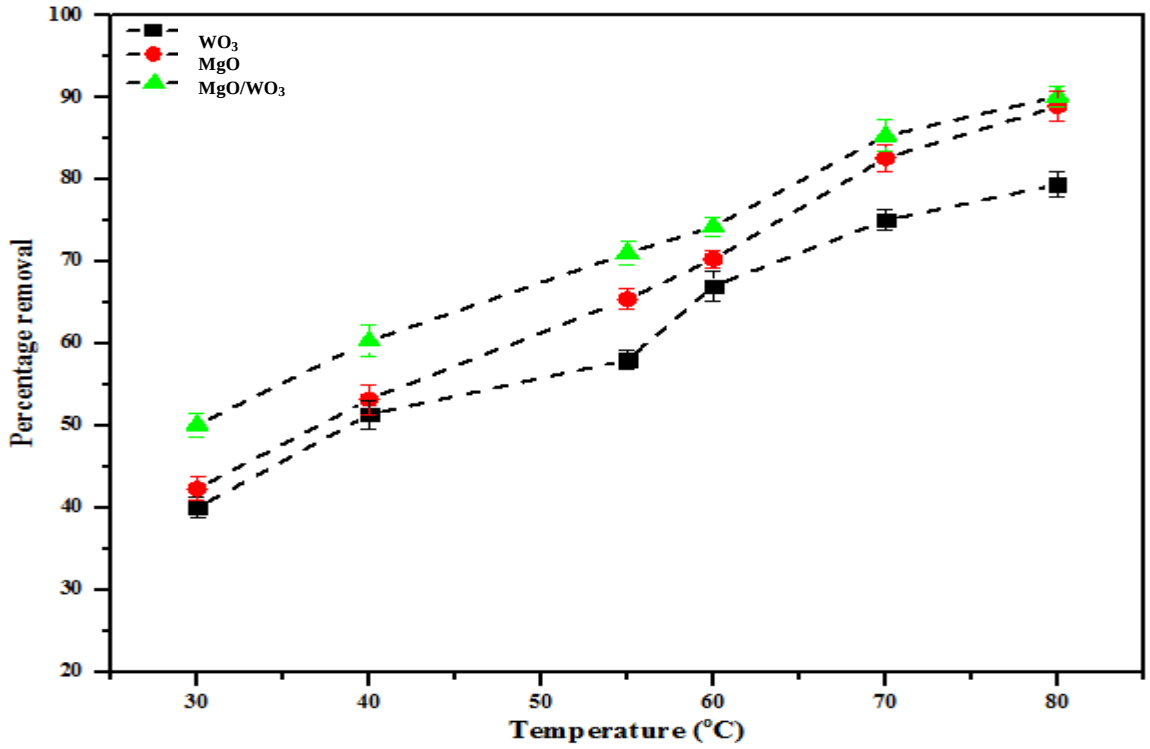

Figure 4.27: Effect of temperature on the removal of TOC (optimum time, dosage 0.1 g, agitation speed 150 rpm)

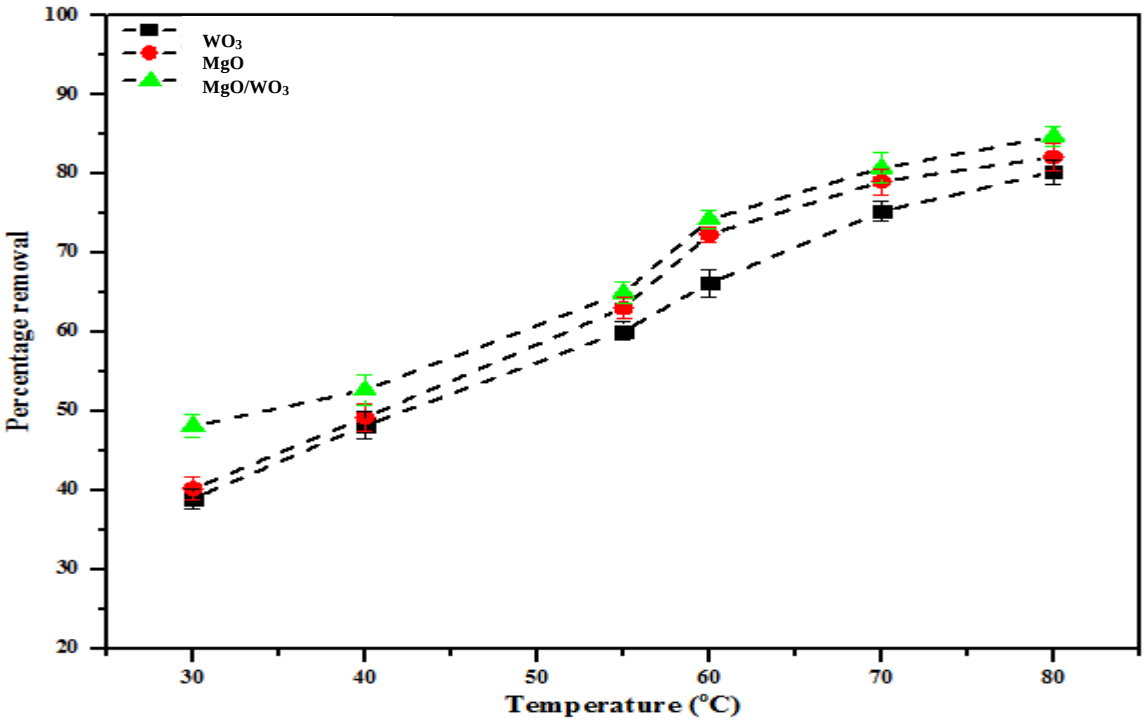

Figure 4.28: Effect of temperature on the reduction of BOD (optimum time, dosage 0.1 g, agitation speed 150 rpm)

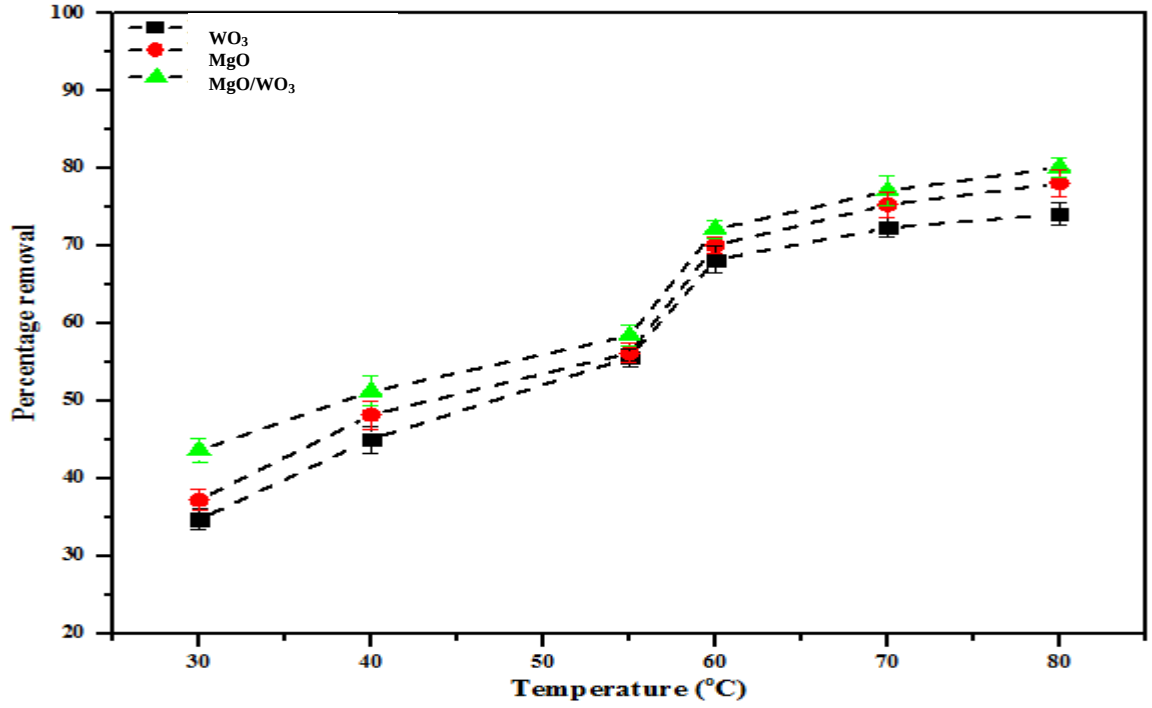

Figure 4.29: Effect of temperature on the reduction of COD (optimum time, dosage 0.1 g, agitation speed 150 rpm)

4.7 Adsorption Isotherm Models

Adsorption isotherms of Cu(II), Fe(II), Cr(VI), TOC, BOD and COD were obtained from the equilibrium adsorption experiment investigated at temperature ranging from 30-80 ^{o}C by MgO, WO_3 and MgO/WO_3 nanoadsorbents. The experimental data were fitted using linearized regression co-efficient according to the Freundlich, Langmuir and Elovich isotherm models as presented in Table 4.4 and 4.5. The fitted linear plots in Appendices suggested that adsorption rate increased with an increase in temperature. The fitness of the experimental data was determined with the regression correlation coefficient. It was found that the Langmuir model is the most suited model compared to Freundlich and Elovich isotherm. The fitted parameters in Table 4.4 and 4.5 showed that highest correlation coefficients were ascribed by Langmuir model. The maximum adsorption capacities of Cu(II), Fe(II) and Cr(VI) using the nanoadsorbents as presented in Table 4.6 were compared with the adsorption capacities of previously prepared adsorbents. It was shown that as-prepared MgO/WO_3 had the highest adsorption capacity in comparison to the earlier reported adsorbents. This can be attributed to the higher specific surface area of the as-synthesised MgO/WO_3 nanocomposites and the mesoporosity nature of the material. This implies that binary metal oxides removed more pollutants from wastewater than individual metal oxide. The Langmuir model explains the homogeneous active surface site. Herein, the pollutants were adsorbed with homogeneous binding sites and the results are in agreement with the finding of Xu *et al.* (2020). The adsorption intensity (n) values in Freundlich model for the pollutants lies between 2 and 10, indicating the nanoadsorbents are good for removal of the pollutants. With regards to the correlation coefficient, this isotherm model did not fit well on the experimental data. In addition it is also stated that the use of these isotherms could tacitly change the error variance and normality assumption of standard least squares. For authenticity of the fitness of isotherm

models, the fitness of equation to the experimental data error function were evaluated. In this work, Chi-square (χ^2) and sum of square error (SSE) tests were used to buttress the best isotherm model as presented in Table 4.4 and 4.5. The lower the error function, the better the isotherm model used for the adsorption of pollutant on to the nanoadsorbents. As can be seen from Table 4.4 and 4.5, the Langmuir isotherm has the least error function values, showing that the adsorption of the pollutant from dyeing wastewater strictly follows Langmuir model. Overall observation on the three isotherm model employed in terms of correlation coefficient and error analysis revealed that this study follows this trend: Langmuir > Elovich > Freundlcih.

Table 4.4: Adsorption isotherm parameters of Cu(II), Fe(II) and Cr(VI) from local dyeing wastewater

Isotherm	Parameter	Cu(II)			Fe(II)			Cr(VI)		
		WO_3	MgO	MgO/WO_3	WO_3	MgO	MgO/WO_3	WO_3	MgO	MgO/WO_3
Langmuir	Q_m	120.31	125.39	128.82	128.65	132.03	135.76	157.73	162.04	165.95
	K_L	4.05×10^{-3}	3.98×10^{-3}	3.92×10^{-3}	3.99×10^{-3}	3.96×10^{-3}	4.12×10^{-3}	1.46×10^{-2}	1.54×10^{-2}	1.59×10^{-2}
	R^2	0.99183	0.99483	0.99662	0.98838	0.98868	0.99453	0.99269	0.99356	0.99799
	SSE	21.09	17.30	13.60	32.17	28.80	19.03	14.09	9.65	5.072
	χ^2	10.54	6.74	4.32	8.11	5.62	2.31	6.04	4.01	2.06
Freundlich	K_F	0.083	0.091	0.099	0.096	0.103	0.117	0.0785	0.086	0.089
	n	1.48×10^{-4}	3.31×10^{-4}	7.19×10^{-4}	6.39×10^{-4}	1.051×10^{-3}	2.718×10^{-3}	1.370×10^{-3}	2.96×10^{-3}	7.20×10^{-3}
	R^2	0.98808	0.98954	0.99043	0.96096	0.98698	0.98625	0.98650	0.99111	0.99052
	SSE	25.70	19.99	17.05	38.56	34.38	27.22	21.08	16.59	15.03
	χ^2	16.64	15.01	12.88	12.90	10.53	8.39	8.97	7.50	5.16
Elovich	B_T	5.450	5.035	4.636	4.831	4.562	4.038	4.238	3.895	3.772
	A_T	0.126	0.127	0.129	0.132	0.133	0.135	0.0544	0.0564	0.0566
	R^2	0.98666	0.99099	0.99185	0.98106	0.98587	0.98882	0.98923	0.99139	0.99196
	SSE	23.05	16.60	14.22	34.52	31.08	23.45	16.63	10.81	8.03
	χ^2	12.09	8.11	7.70	9.08	6.44	3.54	5.27	5.02	3.75

Table 4.5: Adsorption isotherm parameters of TOC, BOD and COD from local dyeing wastewater

Isotherm	Parameter	TOC			BOD			COD		
		WO_3	MgO	MgO/WO_3	WO_3	MgO	MgO/WO_3	WO_3	MgO	MgO/WO_3
Langmuir	Q_m	191.69	193.164	194.73	251.79	287.94	292.02	242.04	296.10	301.52
	K_L	1.80×10^{-3}	1.90×10^{-3}	1.91×10^{-3}	2.09×10^{-4}	1.77×10^{-4}	1.62×10^{-3}	1.42×10^{-3}	1.38×10^{-3}	1.26×10^{-3}
	R^2	0.99396	0.99485	0.99904	0.99585	0.99680	0.99890	0.99532	0.99601	0.99814
	SSE	21.09	15.43	12.82	18.10	17.60	13.52	11.44	9.43	5.05
	χ^2	10.88	7.80	6.03	9.47	8.70	7.14	6.38	5.80	5.30
Freundlich	K_F	0.376	0.432	0.481	0.780	0.800	0.860	0.964	0.980	1.203
	n	5.98×10^{-4}	6.36×10^{-4}	7.48×10^{-4}	4.571	5.259	6.091	7.90	9.120	10.090
	R^2	0.98808	0.97624	0.99043	0.98338	0.98587	0.98625	0.98923	0.99111	0.99052
	SSE	25.22	21.06	19.30	26.07	21.10	17.52	15.11	12.30	10.19
	χ^2	12.41	10.01	9.12	11.81	9.01	8.13	7.70	6.56	6.04
Elovich	B_T	4.290	3.940	3.637	4.339	4.210	3.859	4.704	4.437	4.102
	A_T	0.610	0.617	0.629	0.510	0.580	0.669	0.747	0.856	0.977
	R^2	0.99485	0.98954	0.99610	0.99481	0.99586	0.99759	0.99501	0.99514	0.99714
	SSE	24.15	18.70	15.51	24.20	19.30	16.40	13.06	10.11	7.60
	χ^2	11.02	8.22	7.82	10.60	8.98	7.69	7.45	6.01	5.34

Table 4.6: Comparison of adsorption capacity of MgO/WO_3 adsorbent for metal ion removal with previous literature.

Adsorbent	Adsorption capacity (mg/g)	Metal ion	Experimental condition	Surface area (m^2/g)	Reference
Fe_3O_4/Activated carbon	3.2	Cu	Contact time 3 h, shaking speed 180 rpm, pH 2, Temperature 25 ^oC	51.1	Juang *et al.* (2018)
$MnFe_2O_4$	91.24	Cr	Dosage 1.0 g/L, pH 2	100.62	Bhowinik *et al.* (2017)
EDTA/Bentonite	27	Cu	Contact time 120 min, Temperature 30 ^oC		De-castro *et al.* (2018)
Feo/Rubber seed shell	48.18	Cu	Contact time 30 min, pH 6, Dosage 3 g/L, Temperature 30 ^oC		Prasu *et al.* (2017)
Nanoperlite	16.67	Fe	Dosage 0.15 g, pH 3.2, Concentration 50 mg/L		Seifpanahi *et al.* (2017)
Cus/*Phyllostachys pubescens*	52.30	Cr	Contact time 2 h, Dosage 2 g/L, pH 6.1, Temperature 25 ^oC		Ai *et al.* (2018)
Waste glass	10.31	Fe	Contact time 45 min, Dosage 1.5 g/L, Temperature 25 ^oC	13.33	Nageeb *et al.* (2018)
Graphene oxide	60	Cu	Contact time 20 min		Galumin *et al.* (2018)
Activated carbon	7.76	Fe	Contact time 60 min, Dosage 0.1 g, Temperature 25.15 ^oC, Pressure 101 kPa		Maneechakr and Karnjanakom (2017)
Nickel ferrite/Graphene oxide	20.58	Cr	Contact time 30 min, pH 4, Temperature 25-55 ^oC	80	Linganidinne *et al.* (2017)
MgO/WO_3	128.82	Cu(II)	Contact time 10 min, pH 9.98, Dosage 0.1 g, Temperature 30-80	104.16	This study

			^{o}C		
MgO/WO_3	135.76	Fe(II)	Contact time 15 min, pH 9.98, Dosage 0.1 g, Temperature 30-80 ^{o}C	104.16	This study
MgO/WO_3	165.95	Cr(VI)	Contact time 15 min, pH 9.98, Dosage 0.1 g, Temperature 30-80 ^{o}C	104.16	This study

4.8 Adsorption Kinetic Models

Adsorption studies were conducted on Cu(II), Fe(II), Cr(VI), TOC, BOD and COD removal using MgO, WO_3 and MgO/WO_3 nanoadsorbents. The adsorption data on the removal of pollutants from dyeing wastewater were subjected to kinetic analysis and the results were presented in Table 4.7 and 4.8. From the tables, the kinetic models parameters for adsorption of pollutants were fitted by pseudo-first-order, pseudo-second-order models and intra-particle diffusion. The correlation coefficient of the pseudo-second-order model described the data better, suggesting that the reaction depends on the nanoadsorbents dosage and the concentrations of the pollutants in the wastewater. This suggest that chemisorption played a significant role in the adsorption process. Additionally, the chemisorption process could be linked to exchange of electrons between functional groups on the adsorbent and target metal ions or other pollutants in the medium. Noticeability, the calculated k_2 value was highest for Cr(VI) ions followed by Fe(II) and Cu(II) ions, which was based on the ionic radius mechanism of the adsorbed metal ions on the nanoadsorbents. This confirmed with the report of Mustapha *et al.* (2021) who stated that the less the hydrated ionic radius the high is the rate constant value of the pseudo-second-order.

Table 4.7: Adsorption kinetic parameters of Cu(II), Fe(II) and Cr(VI) from local dyeing wastewater

Pollutant	Adsorbent	First-order					Second-order					Intra-particle diffusion				
		k_1	q_e	R^2	SSE	χ^2	k_2	q_e	R^2	SSE	χ^2	K_i	I	R^2	SSE	χ^2
Cu(II)	WO_3	0.103	0.245	0.5233	102.12	14.01	0.712	1.334	0.9810	91.81	8.20	0.0102	0.162	0.7810	95.05	11.19
	MgO	0.162	0.387	0.5818	88.09	10.02	0.851	1.561	0.9940	75.20	7.65	0.0151	0.240	0.7922	82.31	8.35
	MgO/WO_3	0.180	0.407	0.6551	81.09	7.90	0.910	1.938	0.9920	72.52	5.44	0.0184	0.284	0.8051	75.74	6.53
Fe(II)	WO_3	0.275	0.598	0.5520	98.81	12.60	0.612	1.302	0.9620	73.46	8.09	0.0098	0.158	0.6410	79.03	10.28
	MgO	0.306	0.740	0.6466	80.63	9.31	0.701	1.510	0.9770	69.50	7.29	0.0110	0.213	0.6876	78.01	8.92
	MgO/WO_3	0.494	0.862	0.6951	74.23	7.24	0.821	1.640	0.9800	62.72	4.12	0.0163	0.275	0.7081	70.71	5.15
Cr(VI)	WO_3	0.580	1.227	0.6607	74.18	5.96	0.925	2.329	0.9903	63.26	4.33	0.0175	0.189	0.7984	68.41	5.81
	MgO	0.774	1.387	0.6718	72.32	4.99	1.012	2.420	0.9920	60.12	4.03	0.0240	0.261	0.8449	66.35	4.53
	MgO/WO_3	0.864	1.965	0.6979	67.45	3.97	1.260	2.617	0.9990	58.47	2.10	0.0287	0.290	0.9039	63.86	3.80

Table 4.8: Adsorption kinetic parameters of TOC, BOD and COD from local dyeing wastewater

Pollutant	Adsorbent	First-order					Second-order					Intra-particle diffusion				
		k_1	q_e	R^2	SSE	χ^2	k_2	q_e	R^2	SSE	χ^2	K_i	I	R^2	SSE	χ^2
TOC	WO_3	0.244	0.146	0.7381	80.81	7.47	0.420	0.921	0.9920	72.99	6.34	0.088	0.358	0.8723	74.70	6.37
	MgO	0.362	0.175	0.8832	76.62	6.91	0.513	0.938	0.9938	62.48	5.39	0.093	0.401	0.9023	70.19	6.10
	MgO/WO_3	0.398	0.267	0.8884	64.22	5.88	0.620	0.954	0.9950	53.62	4.32	0.112	0.520	0.9146	59.25	5.11
BOD	WO_3	0.539	104.303	0.8791	74.07	6.02	4.203	152.16	0.9943	64.95	4.15	4.875	93.81	0.9063	70.98	5.39
	MgO	0.887	182.160	0.8962	69.13	5.79	5.102	172.76	0.9952	52.77	3.20	7.106	112.68	0.9110	55.93	4.49
	MgO/WO_3	1.002	272.760	0.9007	60.84	4.10	6.215	190.42	0.9982	50.19	2.99	10.467	130.20	0.9162	58.92	3.73
COD	WO_3	0.741	203.56	0.7064	68.82	3.22	5.042	510.20	0.9980	54.90	2.14	8.506	290.84	0.9219	61.59	3.02
	MgO	0.881	243.67	0.8957	62.10	2.28	6.920	530.76	0.9983	47.83	1.89	14.39	321.96	0.9230	57.24	2.01
	MgO/WO_3	1.385	267.76	0.9106	59.17	2.06	8.430	563.67	0.9998	42.52	1.06	20.44	331.74	0.9308	53.38	1.85

4.9 Thermodynamic Study

The adsorption studies of Cu(II), Fe(II), Cr(VI), TOC, BOD and COD were examined at 30-80 ºC. The values of change in enthalpy, change in entropy and change in free Gibb's energy were determined and presented in Table 4.9 and 4.10. The values of ΔH° were positive and the positive values of ΔS° confirmed the increase in disorderliness and randomness of the adsorbate-nanoadsorbent interface during the adsorption of the pollutants. The positive values of ΔH° revealed that adsorption process was endothermic in nature. The ΔG° for the adsorption of pollutants onto nanoadsorbents indicated that the adsorption of pollutants was thermodynamically spontaneous and feasible. Similar observations on the adsorption of Pb(II) and Cu(II) onto SiO_2/MgO nanofibers. They found that ΔG° at all temperatures for the adsorption of metals were positive and spontaneous. Therefore, it can be inferred that at higher temperature, adsorption process increased resulting to high adsorption capacity.

Table 4.9: Thermodynamic parameters of Cu, Fe and Cr onto MgO, WO_3 and MgO/WO_3 nanoadsorbents from local dyeing wastewater

Pollutant	Adsorbent				ΔG (kJ/mol)					
		ΔH (kJ/mol	ΔS(J/mol/K	R^2	303K	313K	323K	333K	343K	353K
Cu(II)	MgO	20.00	73.32	0.9187	-2.22	-2.95	-3.68	-4.42	-5.15	-5.88
	WO_3	34.89	114.34	0.9678	0.25	-0.90	-2.04	-3.19	-4.33	-5.47
	MgO/WO_3	21.22	76.48	0.9740	-1.95	-2.72	-3.48	-4.25	-5.01	-5.78
Fe(II)	MgO	24.77	82.13	0.8574	-0.11	-0.94	-1.76	-2.58	-3.40	-4.22
	WO_3	17.11	62.92	0.8700	-1.96	-2.58	-3.21	-3.84	-4.47	-5.10
	MgO/WO_3	18.73	67.16	0.9330	-1.62	-2.29	-2.96	-3.63	-4.31	-4.98
Cr(VI)	MgO	24.51	81.71	0.9441	-0.25	-1.07	-.188	-2.70	-3.52	-4.33
	WO_3	17.48	65.76	0.8926	-2.45	-3.10	-3.76	-4.42	-5.08	-5.73
	MgO/WO_3	16.80	63.28	0.8877	-2.38	-3.01	-3.64	-4.27	-4.91	-5.54

Table 4.10: Thermodynamic parameters of TOC, BOD and COD onto MgO, WO_3 and MgO/WO_3 nanoadsorbents from local dyeing wastewater

Pollutant	Adsorbent				ΔG (kJ/mol)					
		ΔH (kJ/mol	ΔS(J/mol/K	R^2	303K	313K	323K	333K	343K	353K
TOC	MgO	19.42	64.18	0.8709	-0.027	-0.67	-1.31	-1.95	-2.59	-3.24
	WO_3	8.71	29.29	0.8747	-0.17	-0.46	-0.75	-1.04	-1.34	-1.63
	MgO/WO_3	9.35	31.11	0.9257	-0.076	-0.39	-0.70	-1.01	-1.32	-1.63
BOD	MgO	20.22	66.91	0.8530	-0.054	-0.72	-1.39	-2.06	-2.73	-3.40
	WO_3	24.65	89.92	0.8671	-0.60	-1.50	-2.39	-3.29	-4.19	-5.09
	MgO/WO_3	23.54	82.99	0.9046	-1.43	-2.44	-3.27	-4.10	-4.93	-5.76
COD	MgO	25.70	86.52	0.8225	-0.52	-1.38	-2.25	-3.11	-3.98	-4.84
	WO_3	29.92	99.46	0.8624	-0.22	-1.21	-2.21	-3.20	-4.20	-5.19
	MgO/WO_3	27.03	93.23	0.8873	-1.22	-2.15	-3.08	-4.02	-4.95	-5.88

4.10 Regeneration Study

The regeneration studies were evaluated to determine the reusability of the nanoadsorbents. The regeneration experiments of MgO, WO_3 and MgO/WO_3 nanoadsorbents were investigated and the percentage removal of the adsorbents cycles after each is presented in Figure 4.30 (A-B). The results showed that the MgO/WO_3 nanocomposites have the highest adsorption capacities for Cu(II), Fe(II) and Cr(VI) ions even after 5 repeated cycles. The percentage removal for MgO and WO_3 nanoparticles were still high at cycle 3, but subsequently dropped as the number of cycles increased. This implies that the two materials cannot be used repeatedly beyond 3 cycles. This further suggests total collapse of the inner and outer pores or gradual blockage of the active sites by the pollutants. The adsorption capacity of the MgO/WO_3 nanocomposites did not indicate any significant decrease in adsorption of Cr(VI), Fe(II) and Cu(II) ion even after regeneration cycle of 5. The value of cycles corresponds to the results of BET analysis and adsorption capacities of factor influencing the adsorption previously mentioned. The stability of the nanocomposites demonstrated that the nanoadsorbent could offer high adsorption property for removal of pollutants. It was also revealed that the nanoadsorbent gave an insight on further application of nanoadsorbent by desorption of the adsorbed metal ions in the reuse of the nanomaterials. The regenerated adsorbents may be employed for industrial applications.

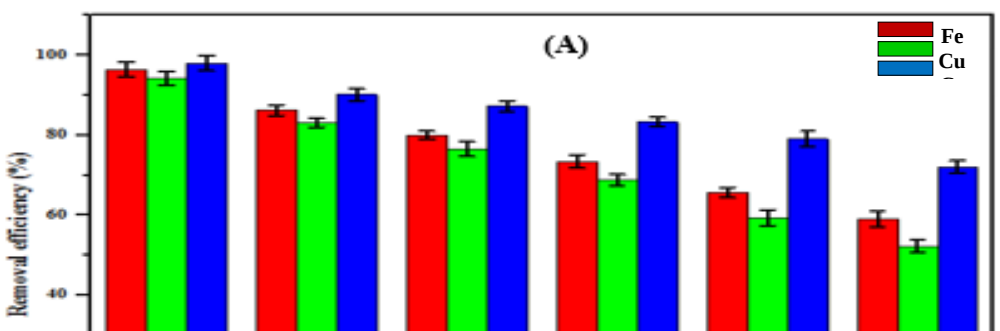

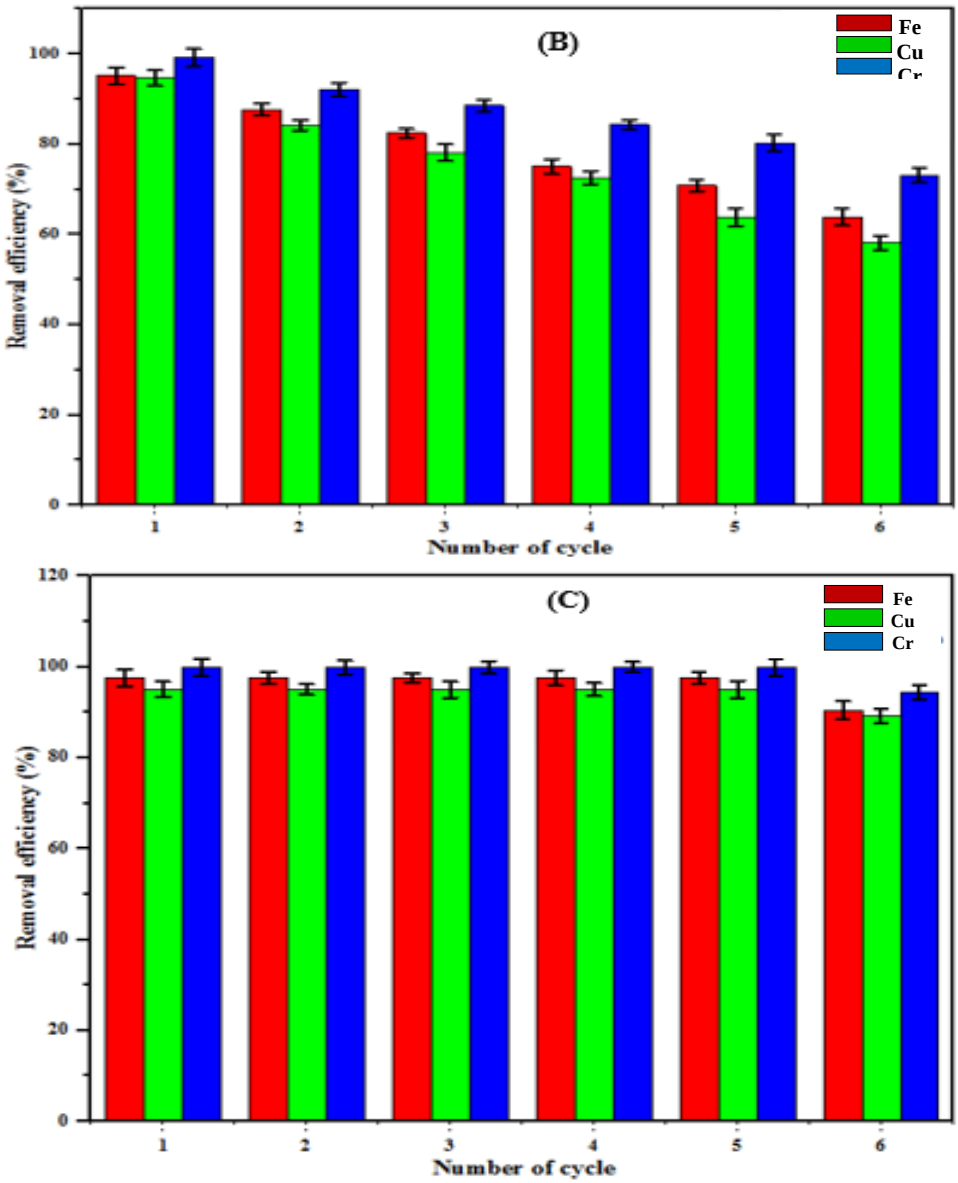

Figure 4.30: Reusability cycles using (A) MgO (B) WO_3 and (C) MgO/WO_3 for Fe(II), Cu(II) and Cr(VI) removal

CHAPTER FIVE

5.0 CONCLUSION AND RECOMMENDATIOS

5.1 Conclusion

The synthesis, characterisation and application of biosynthesised MgO/WO_3 nanocomposites for the treatment of dyeing wastewater were examined. The as-prepared MgO, WO_3 and MgO/WO_3 nanoadsorbents were used for the adsorption of TOC, BOD, COD and some heavy metals in dyeing wastewater. Adsorption experiments were investigated under the influence of contact time, nanoadsorbent dosage and temperature. The isotherm, kinetic and regeneration studies were described in this study. The following conclusions were drawn based on the results obtained;

a) The nanoadsorbents were synthesised using green method, which showed monoclinic crystalline phase of WO_3, face centered cubic phase of MgO nanoparticles, the existence of chemical reactions between MgO and WO_3 nanocomposites leading to the formation of a new material $MgWO_4$.

b) The HRSEM, HRTEM, BET, EDX and SAED revealed the presences of MgO and WO_3 nanoparticles in their composites at different mixing ratios. The EDX results showed that the synthesised nanocomposites composed of O, Mg and W which confirmed the pure formations of oxide of Mg and W. However, the XRD showed the formation of $MgWO_4$ nanoparticles irrespective of the mixing ratios.

c) The adsorption studies were performed under different conditions such as contact time, dosage and temperature. It was deduced that the adsorption process was dosage and temperature dependent. The maximum removal efficiency of Cu(II), Fe(II) and Cr(VI) at optimum contact time, and dosage 1.0 g, are 98.1 %, 100 % and 100 %, respectively.

d) The adsorption of the pollutants from dyeing wastewater followed Langmuir isotherm model and pseudo-second-order kinetic model.

e) Thermodynamic study described the adsorption as endothermic and spontaneous in nature.

f) Regeneration study showed that the adsorption of Cr(VI), Fe(II) and Cu(II) ions using MgO/WO_3 nanocomposite from local dyeing wastewater after six consecutive cycles did not change from the initial amount removed. This suggested the suitability of MgO/WO_3 nanocomposite for repeated application in wastewater treatment technology.

5.2 Recommendations

Based on the results of the analysis, the following recommendations are made.

- Optimization of other synthesis parameters such as reaction time, stirring speed, reaction temperature, and concentration of the metal salt precursors should be carried out on the preparation of MgO, WO_3 and $MgWO_4$.
- Annealing of $MgWO_4$ produced at different temperatures as well as investigation of its adsorption potential should be carried out.
- Fixed column adsorption studies using the prepared MgO, WO_3 and MgO/WO_3 for the removal of selected heavy metals and other indicator parameters in local dyeing wastewater should be investigated.

5.3 Contribution to Knowledge

The characterisation of the synthesised nanocomposite of MgO/WO_3 using XRD, EDX, HRSEM, HRTEM, SAED and BET confirmed the successful incorporation of MgO and WO_3 nanaparticles leading to the formation of a bimetallic nanocomposite.

The existence of strong chemical reaction between MgO and WO_3 nanaparticles in the synthesis process irrespective of the mixing ratio led to the formation of a new novel material magnesium tungstate ($MgWO_4$) as revealed from the XRD result.

The application of the MgO/WO_3 nanocomposite for the removal of selected heavy metals in local dyeing wastewater was successfully carried out and maximum removal efficiency of Cu, Fe and Cr at optimum contact time of 10m, 15m and 15m and dosage are 98.1%, 100% and 100% respectively.

REFERENCES

Abdelnaeim, M. Y., El Sherif, I. Y., Attia, A. A., Fathy, N. A., & El-Shahat, M. F. (2016). Impact of chemical activation on the adsorption performance of common reed towards Cu (II) and Cd (II). *International Journal of Mineral Processing*, *157*, 80-88.

Abdullahi, A., Hostert, M., & Pascoli, S. (2021). A dark seesaw solution to low energy anomalies: MiniBooNE, the muon (g− 2), and BaBar. *Physics Letters B*, *820*, 136531.

Abinaya, S., Kavitha, H. P., Prakash, M., & Muthukrishnaraj, A. (2021). Green synthesis of magnesium oxide nanoparticles and its applications: A review. *Sustainable Chemistry and Pharmacy*, 19, 100368.

Abshirini, Y., Esmaeili, H., & Foroutan, R. (2019). Enhancement removal of Cr (VI) ion using magnetically modified MgO nanoparticles. *Materials Research Express*, 6(12), 125513

Ahmad, T., Aadil, R. M., Ahmed, H., ur Rahman, U., Soares, B. C., Souza, S. L. Pimentel, T.C., Scudino, H., Guimarães, J.T., Esmerino, E.A. & Cruz, A. G. (2019). Treatment and utilization of dairy industrial waste: A review. *Trends in Food Science & Technology*, 88, 361-372.

Ahmadifard, T., Heydari, R., Tarrahi, M. J., & Khorramabadi, G. S. (2019). Photocatalytic degradation of diazinon in aqueous solutions using immobilized MgO nanoparticles on concrete. *International Journal of Chemical Reactor Engineering*, *17*(9).

Ahmed, S., Chaudhry, S. A., & Ikram, S. (2017). A review on biogenic synthesis of ZnO nanoparticles using plant extracts and microbes: a prospect towards green chemistry. *Journal of Photochemistry and Photobiology B: Biology*, *166*, 272-284.

Ama, O. M., & Arotiba, O. A. (2017). Exfoliated graphite/titanium dioxide for enhanced photoelectrochemical degradation of methylene blue dye under simulated visible light irradiation. *Journal of Electroanalytical Chemistry*, *803*, 157-164.

American Public Health Association (APHA), (2017). Standard Methods for the Examination of Water and Wastewater, 21st ed., APHA American Public Health Association, Washington, D.C., 2005.

Amrane, A., Rajendran, S., Nguyen, T. A., Sharoba, A. M., & Assadi, A. A. (Eds.). (2020). *Nanotechnology in the Beverage Industry: Fundamentals and Applications*. Elsevier.

Arya, S., Mahajan, P., Mahajan, S., Khosla, A., Datt, R., Gupta, V., Young, S.J. & Oruganti, S. K. (2021). Influence of processing parameters to control morphology and optical properties of Sol-Gel synthesized ZnO nanoparticles. *ECS Journal of Solid State Science and Technology*, 10(2), 023002.

Asha, S., Asha, A., & Rajeshkumar, S. (2017). Evaluation of phytochemical constituents and antimicrobial activity of silver nanoparticle synthesized ipomoea nil against selected pathogens. *Asian Journal of Pharmaceutical and Clinical Research*, 10, 183-7.

Awwad, N. S., El-Zahhar, A. A., & Alasmary, J. A. (2020). Removal of Methylene Blue Dyes from Aqueous System Using Composite Polymeric-Apatite Resins. In *Chemistry and Technology of Natural and Synthetic Dyes and Pigments*. IntechOpen. pp. 1-21.

Azari, A., Nabizadeh, R., Nasseri, S., Mahvi, A. H., & Mesdaghinia, A. R. (2020). Comprehensive systematic review and meta-analysis of dyes adsorption by carbon-based adsorbent materials: Classification and analysis of last decade studies. *Chemosphere*, 250, 126238.

Azeem, A., Ashraf, M., Munir, U., Sarwar, Z., Abid, S., & Iqbal, N. (2016). Synthesis of tungsten oxide nanorod, its application on textile material, and study of its functional properties. *Journal of Nanotechnology*, *2016*.

Aziz, B. K., & Karim, M. A. (2019). Efficient catalytic photodegradation of methylene blue from medical lab wastewater using MgO nanoparticles synthesized by direct

precipitation method. *Reaction Kinetics, Mechanisms and Catalysis*, *128*(2), 1127-1139.

Bhatia, D., Sharma, N. R., Kanwar, R., & Singh, J. (2018). Physicochemical assessment of industrial textile effluents of Punjab (India). *Applied Water Science*, 8(3), 1-12.

Bouabidi, Z. B., El-Naas, M. H., Cortes, D., & McKay, G. (2018). Steel-making dust as a potential adsorbent for the removal of lead (II) from an aqueous solution. *Chemical Engineering Journal*, *334*, 837-844.

Cañas-Carrell, J. E., Li, S., Parra, A. M., & Shrestha, B. (2014). Metal oxide nanomaterials: health and environmental effects. In *Health and Environmental Safety of Nanomaterials* (pp. 200-221). Woodhead Publishing.

Chai, W. S., Cheun, J. Y., Kumar, P. S., Mubashir, M., Majeed, Z., Banat, F., Ho, S.H. & Show, P. L. (2021). A review on conventional and novel materials towards heavy metal adsorption in wastewater treatment application. *Journal of Cleaner Production*, 126589.

Chen, D., Cheng, Y., Zhou, N., Chen, P., Wang, Y., Li, K., & Ruan, R. (2020). Photocatalytic degradation of organic pollutants using TiO2-based photocatalysts: A review. *Journal of Cleaner Production*, *268*, 121725.

Chen, L. C., Zhu, Y., Papandreou, G., Schroff, F., & Adam, H. (2018). Encoder-decoder with atrous separable convolution for semantic image segmentation. In *Proceedings of the European conference on computer vision (ECCV)* (pp. 801-818).

Chockalingam, N., Banerjee, S., & Muruhan, S. (2019). Characterization of physicochemical parameters of textile effluents and its impacts on environment. *Environment and Natural Resources Journal*, 17(2), 41-53.

Chowdhury, I. H., Chowdhury, A. H., Bose, P., Mandal, S., & Naskar, M. K. (2016). Effect of anion type on the synthesis of mesoporous nanostructured MgO, and its excellent adsorption capacity for the removal of toxic heavy metal ions from water. *RSC Advances*, 6(8), 6038-6047.

Colpani, G. L., Dal'Toé, A. T. O., Zanetti, M., Zeferino, R. C. F., Silva, L. L., de Mello, J. M. M., & Fiori, M. A. (2018). Photocatalytic Adsorbents Nanoparticles. In *Advanced Sorption Process Applications*. IntechOpen. pp. 63-85.

Crini, G., Lichtfouse, E., Wilson, L. D., & Morin-Crini, N. (2019). Conventional and non-conventional adsorbents for wastewater treatment. *Environmental Chemistry Letters*, 17(1), 195-213.

Daneshvar, E., Zarrinmehr, M.J., Kousha, M., Hashtjin, A.M., Saratale, G.D., Maiti, A., Vithanage, M. and Bhatnagar, A., (2019). Hexavalent chromium removal from water by microalgal-based materials: Adsorption, desorption and recovery studies. *Bioresource Technology*, 293, 122064.

Dobrota, A. S., & Pašti, I. A. (2020). Chemisorption as the essential step in electrochemical energy conversion. *Journal of Electrochemical Science and Engineering*, 10(2), 141-159.

Durotoye, T. O., Adeyemi, A. A., Omole, D. O., & Onakunle, O. (2018). Impact assessment of wastewater discharge from a textile industry in Lagos, Nigeria. *Cogent Engineering*, *5*(1), 1531687.

Dursun, S., Koyuncu, S. N., Kaya, İ. C., Kaya, G. G., Kalem, V., & Akyildiz, H. (2020). Production of CuO–WO3 hybrids and their dye removal capacity/performance from wastewater by adsorption/photocatalysis. *Journal of Water Process Engineering*, *36*, 101390

Edokpayi, J. N., Odiyo, J. O., & Durowoju, O. S. (2017). Impact of wastewater on surface water quality in developing countries: a case study of South Africa. *Water Quality*, 401-416.

Egbosiuba, T. C., Abdulkareem, A. S., Kovo, A. S., Afolabi, E. A., Tijani, J. O., Auta, M., & Roos, W. D. (2020). Ultrasonic enhanced adsorption of methylene blue onto the optimized surface area of activated carbon: Adsorption isotherm, kinetics and thermodynamics. *Chemical Engineering Research and Design*, 153, 315-336.

El-Gendy, N. S., & Nassar, H. N. (2020). Sustainable Photo-and Bio-Catalysts for Wastewater Treatment. *Photocatalysts in Advanced Oxidation Processes for Wastewater Treatment*, 1, 139-165.

Epp, J. (2016). X-ray diffraction (XRD) techniques for materials characterization. In *Materials characterization using nondestructive evaluation (NDE) methods* (pp. 81-124). Woodhead Publishing.

Esposito, S. (2019). "Traditional" sol-gel chemistry as a powerful tool for the preparation of supported metal and metal oxide catalysts. *Materials*, 12(4), 668.

Fakhri, A., & Behrouz, S. (2015). Comparison studies of adsorption properties of MgO nanoparticles and ZnO–MgO nanocomposites for linezolid antibiotic removal from aqueous solution using response surface methodology. *Process Safety and Environmental Protection*, *94*, 37-43.

Fakhri, A., & Behrouz, S. (2015). Photocatalytic properties of tungsten trioxide (WO_3) nanoparticles for degradation of Lidocaine under visible and sunlight irradiation. *Solar Energy*, *112*, 163-168

Farner, J. M., De Tommaso, J., Mantel, H., Cheong, R. S., & Tufenkji, N. (2020). Effect of freeze/thaw on aggregation and transport of nano-TiO_2 in saturated porous media. *Environmental Science: Nano*. 7(6), 1781-1793.

Fathi, E., Derakhshanfard, F., Gharbani, P., & Tabatabaei, Z. G. (2020). Facile Synthesis of MgO/C_3N_4 Nanocomposite for Removal of Reactive Orange 16 under Visible Light. *Journal of Inorganic and Organometallic Polymers and Materials*, *30*(6), 2234-2240.

Fenta, M.M. (2014). Heavy Metals Concentration in Effluents of Textile Industry, Tikur Wuha River and Milk of Cows Watering on this Water Source, Hawassa, Southern Ethiopia. *Research Journal of Environmental Sciences*, 8, 422-434.

Ghaly, A.E., Ananthashankar, R., Alhattab, M. & Ramakrishna, V.V. (2014). Production, Characterization and Treatment of Textile Effluents: A Critical Review. *Journal of Chemical Engineering and Process Technology*, 5(1), 1-18.

Ghasemi, L., & Jafari, H. (2017). Morphological characterization of tungsten trioxide nanopowders synthesized by sol-gel modified Pechini's method. *Materials Research*, *20*(6), 1713-1721.

Girish, C. R. (2017). Various isotherm models for multicomponent adsorption: a review. *International Journal of Civil Engineering and Technology*, 8(10), 80-86.

Girish, K. (2019). Chapter-3 Microbial Decolourization of Textile Dyes and Biodegradation of Textile Industry Effluent. *Advances IN*, pp. 37-67.

Gnanamuthu, S. J., Vijayapriya, J., Parasuraman, K., Ali, T. M., & Ebinezar, I. J. D. (2019). Photocatalytic Activity of Undoped WO_3 Nano Particles Prepared by Hydrothermal Method. *International Journal of Research and Analytical Reviews*, 6(1), 934-941.

Gürses, A., Açıkyıldız, M., Güneş, K., & Gürses, M. S. (2016). Colorants in health and environmental aspects. In *Dyes and Pigments* (pp. 69-83). Springer, Cham.

Hafez, M., Popov, A. I., & Rashad, M. (2020). A novel environmental additives to decrease nitrate level in agriculture wastewater and enhancement nutrient status under greenhouse plant growth in calcareous soil. *Plant Arch*, 20, 3165-72.

Hassaan, M. A., & El Nemr, A. (2017). Health and environmental impacts of dyes: mini review. *American Journal of Environmental Science and Engineering*, 1(3), 64-67.

Holkar, C. R., Jadhav, A. J., Pinjari, D. V., Mahamuni, N. M., & Pandit, A. B. (2016). A critical review on textile wastewater treatments: possible approaches. *Journal of environmental management*, *182*, 351-366.

Homaeigohar, S. (2020). The nanosized dye adsorbents for water treatment. *Nanomaterials*, 10(2), 295-336.

Homagai, P. L. (2018). Studies on the development of natural cation exchanger for heavy metals removal (Doctoral dissertation).

Hossain, L., Sarker, S. K., & Khan, M. S. (2018). Evaluation of present and future wastewater impacts of textile dyeing industries in Bangladesh. *Environmental Development*, *26*, 23-33.

Ibrahim, R. K., Hayyan, M., AlSaadi, M. A., Hayyan, A., & Ibrahim, S. (2016). Environmental application of nanotechnology: air, soil, and water. *Environmental Science and Pollution Research*, 23(14), 13754-13788.

Inkson, B. J. (2016). Scanning electron microscopy (SEM) and transmission electron microscopy (TEM) for materials characterization. In *Materials characterization using nondestructive evaluation (NDE) methods* (pp. 17-43).

Inyinbor Adejumoke, A., Adebesin Babatunde, O., Oluyori Abimbola, P., Adelani Akande Tabitha, A., Dada Adewumi, O., & Oreofe Toyin, A. (2018). Water pollution: effects, prevention, and climatic impact. *Water Challenges of an Urbanizing World*, 33.

Islam, S. Z., Nagpure, S., Kim, D. Y., & Rankin, S. E. (2017). Synthesis and catalytic applications of non-metal doped mesoporous titania. *Inorganics*, 5(1), 15.

Ismail, M., Akhtar, K., Khan, M.I., Kamal, T., Khan, M.A., M Asiri, A., Seo, J. and Khan, S.B., 2019. Pollution, toxicity and carcinogenicity of organic dyes and their catalytic bio-remediation. *Current Pharmaceutical Design*, 25(34), 3645-3663.

Jamee, R., & Siddique, R. (2019). Biodegradation of synthetic dyes of textile effluent by microorganisms: an environmentally and economically sustainable approach. *European Journal of Microbiology and Immunology*, 9(4), 114-118.

Jeevanandam, J., Barhoum, A., Chan, Y. S., Dufresne, A., & Danquah, M. K. (2018). Review on nanoparticles and nanostructured materials: history, sources, toxicity and regulations. *Beilstein Journal of Nanotechnology*, 9(1), 1050-1074.

Joshi, S., & Srivastava, R. K. (2019). Adsorptive removal of lead (Pb), copper (Cu), nickel (Ni) and mercury (Hg) ions from water using chitosan silica gel composite. *Environmental monitoring and assessment*, 191(10), 1-9.

Juang, R. S., Yei, Y. C., Liao, C. S., Lin, K. S., Lu, H. C., Wang, S. F., & Sun, A. C. (2018). Synthesis of magnetic Fe3O4/activated carbon nanocomposites with high surface area as recoverable adsorbents. *Journal of the Taiwan Institute of Chemical Engineers*, *90*, 51-60.

Kajjumba, G. W., Emik, S., Öngen, A., Özcan, H. K., & Aydın, S. (2018). Modelling of adsorption kinetic processes-errors, theory and application. In *Advanced sorption process applications*. IntechOpen. pp. 187-205.

Kandisa, R. V., Narayana Saibaba, K. V., Shaik, K. B., & Gopinath, R. (2016). Dye removal by adsorption: a review. *Journal of Bioremedation and Biodegradation*, 7(6), 317-321.

Karimi-Maleh, H., Orooji, Y., Ayati, A., Qanbari, S., Tanhaei, B., Karimi, F., Alizadeh, M., Rouhi, J., Fu, L. & Sillanpää, M. (2020). Recent advances in removal techniques of Cr (VI) toxic ion from aqueous solution: A comprehensive review. *Journal of Molecular Liquids*, 392, 115062.

Karthik, K., Dhanuskodi, S., Gobinath, C., Prabukumar, S., & Sivaramakrishnan, S. (2019). Ultrasonic-assisted CdO–MgO nanocomposite for multifunctional applications. *Materials Technology*, 34(7), 403-414.

Karthik, K., Dhanuskodi, S., Gobinath, C., Prabukumar, S., & Sivaramakrishnan, S. (2019). Fabrication of MgO nanostructures and its efficient photocatalytic, antibacterial and anticancer performance. *Journal of Photochemistry and Photobiology B: Biology*, *190*, 8-20.

khamis Soliman, N., Moustafa, A. F., Aboud, A. A., & Halim, K. S. A. (2019). Effective utilization of Moringa seeds waste as a new green environmental adsorbent for removal of industrial toxic dyes. *Journal of Materials Research and Technology*, 8(2), 1798-1808.

Khan, F.S.A., Mubarak, N.M., Tan, Y.H., Khalid, M., Karri, R.R., Walvekar, R., Abdullah, E.C., Nizamuddin, S. & Mazari, S.A. (2021). A comprehensive review on magnetic carbon nanotubes and carbon nanotube-based buckypaper-heavy metal and dyes removal. *Journal of Hazardous Materials*, 413, 125375.

Khan, I., Saeed, K., & Khan, I. (2019). Nanoparticles: Properties, applications and toxicities. *Arabian Journal of Chemistry*, 12(7), 908-931.

Khan, S., & Malik, A. (2014). Environmental and health effects of textile industry wastewater. In *Environmental deterioration and human health* (pp. 55-71). Springer, Dordrecht.

Kumar, D., Pandit, P. D., Patel, Z., Bhairappanavar, S. B., & Das, J. (2019). Perspectives, Scope, Advancements, and Challenges of Microbial Technologies Treating Textile Industry Effluents. In *Microbial Wastewater Treatment* (pp. 237-260). Elsevier.

Kumar, K.V., Gadipelli, S., Wood, B., Ramisetty, K.A., Stewart, A.A., Howard, C.A., Brett, D.J. & Rodriguez-Reinoso, F. (2019). Characterization of the adsorption site energies and heterogeneous surfaces of porous materials. *Journal of Materials Chemistry A*, 7(17), 10104-10137.

Kumar, S., Bhushan, P., & Bhattacharya, S. (2018). Fabrication of nanostructures with bottom-up approach and their utility in diagnostics, therapeutics, and others. In *Environmental, Chemical and Medical Sensors* (pp. 167-198). Springer, Singapore.

Kumar, T. V., Sivasankar, V., Fayoud, N., Abou Oualid, H., & Sundramoorthy, A. K. (2018). Synthesis and characterization of coral-like hierarchical MgO incorporated fly ash composite for the effective adsorption of azo dye from aqueous solution. *Applied Surface Science*, 449, 719-728.

Lai, C. W. (2015). WO_3 nanoplates film: formation and photocatalytic oxidation studies. *Journal of Nanomaterials*, 1-8.

Lei, R., Zhang, H., Ni, H., Chen, R., Gu, H., & Zhang, B. (2018). Novel ZnO nanoparticles modified WO_3 nanosheet arrays for enhanced photocatalytic properties under solar light illumination. *Applied Surface Science*, 463, 363-373.

Lellis, B., Fávaro-Polonio, C. Z., Pamphile, J. A., & Polonio, J. C. (2019). Effects of textile dyes on health and the environment and bioremediation potential of living organisms. *Biotechnology Research and Innovation*, 3(2), 275-290.

Li, Y., Zhou, X., Luo, W., Cheng, X., Zhu, Y., El-Toni, A. M. Khan, A., Deng, Y. & Zhao, D. (2019). Pore enÜineering of mesoporous tungsten oxides for ultrasensitive gas sensing. *Advanced Materials Interfaces*, 6(1), 1801269.

Lu, F., & Astruc, D. (2020). Nanocatalysts and other nanomaterials for water remediation from organic pollutants. *Coordination Chemistry Reviews*, 408, 213180.

Madhav, S., Ahamad, A., Singh, P., & Mishra, P. K. (2018). A review of textile industry: Wet processing, environmental impacts, and effluent treatment methods. *Environmental Quality Management*, 27(3), 31-41.

Madzokere, T. C., & Karthigeyan, A. (2017). Heavy Metal Ion Effluent Discharge Containment Using Magnesium Oxide (MgO) Nanoparticles. *Materials Today: Proceedings*, 4(1), 9-18.

Maharana, M., Manna, M., Sardar, M., & Sen, S. (2021). Heavy Metal Removal by Low-Cost Adsorbents. In *Green Adsorbents to Remove Metals, Dyes and Boron from Polluted Water* (pp. 245-272). Springer, Cham.

Mani, S., Chowdhary, P., & Bharagava, R. N. (2019). Textile wastewater dyes: toxicity profile and treatment approaches. In *Emerging and eco-friendly approaches for waste management* (pp. 219-244). Springer, Singapore.

Markandeya, S., Shukla, P., & Mohan, D. (2017). Toxicity of disperse dyes and its removal from wastewater using various adsorbents: A review. *Research Journal of Environmental Toxicology*, 11, 72-89.

Masindi, V., & Muedi, K. L. (2018). Environmental contamination by heavy metals. *Heavy Metals*, IntechOpen. pp. 115-132.

Methneni, N., González, J. A. M., Jaziri, A., Mansour, H. B., & Fernandez-Serrano, M. (2021). Persistent organic and inorganic pollutants in the effluents from the textile dyeing industries: Ecotoxicology Appraisal via a battery of Biotests. *Environmental Research*, 196, 110956.

Mioduska, J., Zielińska-Jurek, A., Janczarek, M., & Hupka, J. (2016). The effect of calcination temperature on structure and photocatalytic properties of WO_3/TiO_2 nanocomposites. *Journal of Nanomaterials*, *2016*.

Mishra, S., Bharagava, R. N., More, N., Yadav, A., Zainith, S., Mani, S., & Chowdhary, P. (2019). Heavy metal contamination: an alarming threat to environment and human health. In *Environmental biotechnology: For sustainable future* (pp. 103-125). Springer, Singapore.

Miyah, Y., Lahrichi, A., Idrissi, M., Khalil, A., & Zerrouq, F. (2018). Adsorption of methylene blue dye from aqueous solutions onto walnut shells powder: equilibrium and kinetic studies. *Surfaces and Interfaces*, 11, 74-81.

Mourdikoudis, S., Pallares, R. M., & Thanh, N. T. (2018). Characterization techniques for nanoparticles: comparison and complementarity upon studying nanoparticle properties. *Nanoscale*, 10(27), 12871-12934.

Moustafa, I. M. I., Saleh, I. A., & Abdelhami, M. R. (2017). Synthesis of MgO nanoparticles from different organic precursors: catalytic decontamination of organic pollutants and antitumor activity. *Journal of Material Science and Engineering*, 6(4), 1-8.

Munagapati, V. S., & Kim, D. S. (2017). Equilibrium isotherms, kinetics, and thermodynamics studies for congo red adsorption using calcium alginate beads impregnated with nano-goethite. *Ecotoxicology and environmental safety*, *141*, 226-234.

Mustapha, S., Ndamitso, M. M., Abdulkareem, A. S., Tijani, J. O., Shuaib, D. T., Ajala, A. O., & Mohammed, A. K. (2020). Application of TiO_2 and ZnO nanoparticles immobilized on clay in wastewater treatment: a review. *Applied Water Science*, 10(1), 1-36.

Mustapha, S., Tijani, J. O., Ndamitso, M. M., Abdulkareem, A. S., Shuaib, D. T., & Mohammed, A. K. (2021). Adsorptive removal of pollutants from industrial wastewater using mesoporous kaolin and kaolin/TiO2 nanoadsorbents. *Environmental Nanotechnology, Monitoring & Management*, 15, 100414.

Nagarjuna, R., Challagulla, S., Sahu, P., Roy, S., & Ganesan, R. (2017). Polymerizable sol–gel synthesis of nano-crystalline WO3 and its photocatalytic Cr (VI) reduction under visible light. *Advanced Powder Technology*, *28*(12), 3265-3273.

Naik, K., Mishra, S., Srichandan, H., Singh, P. K., & Sarangi, P. K. (2019). Plant growth promoting microbes: Potential link to sustainable agriculture and environment. *Biocatalysis and Agricultural Biotechnology*, 21, 101326.

Nigerian Industrial Standard (NIS), (2007). Nigerian Standard for Drinking Water Quality. NIS554, Standard Organization of Nigeria, 2007, p.1-30.

Noori, A. J., & Kareem, F. A. (2020). Setting time, mechanical and adhesive properties of magnesium oxide nanoparticles modified glass-ionomer cement. *Journal of Materials Research and Technology*, *9*(2), 1809-1818.

Padmaja, K., Cherukuri, J., & Reddy, M. A. (2014). Conventional to cutting edge technologies in Drinking Water Purification–a REVIEW. *International Journal of Innovative Research in Science, Engineering and Technology*, *3*(2), 9375-9385.

Pasinszki, T., & Krebsz, M. (2020). Synthesis and application of zero-valent iron nanoparticles in water treatment, environmental remediation, catalysis, and their biological effects. *Nanomaterials*, 10(5), 917.

Pensupa, N., Leu, S. Y., Hu, Y., Du, C., Liu, H., Jing, H., Wang, H. & Lin, C. S. K. (2017). Recent trends in sustainable textile waste recycling methods: Current situation and future prospects. *Chemistry and Chemical Technologies in Waste Valorization*, pp. 189-228.

Rao, B. G., Mukherjee, D., & Reddy, B. M. (2017). Novel approaches for preparation of nanoparticles. In *Nanostructures for Novel Therapy* (1-36). Elsevier.

Rathi, B. S., Kumar, P. S., & Show, P. L. (2021). A review on effective removal of emerging contaminants from aquatic systems: Current trends and scope for further research. *Journal of Hazardous Materials*, 409, 124413.

Rawat, S., Pullagurala, V. L., Adisa, I. O., Wang, Y., Peralta-Videa, J. R., & Gardea-Torresdey, J. L. (2018). Factors affecting fate and transport of engineered

nanomaterials in terrestrial environments. *Current Opinion in Environmental Science & Health*, *6*, 47-53.

Rehman, K., Fatima, F., Waheed, I., & Akash, M. S. H. (2018). Prevalence of exposure of heavy metals and their impact on health consequences. *Journal of Cellular Biochemistry*, 119(1), 157-184.

Reid, K. (2018). Global water crisis: Facts, FAQs, and how to help. World vision. Online.

Rohini, C., Geetha, P. S., Vijayalakshmi, R., & Mini, M. L. (2021). Phytochemicals characterization of nutraceutical enriched fruits and nuts spread. *Journal of Applied and Natural Science*, *13*(SI), 124-129.

Roy, N. K., Foong, C. S., & Cullinan, M. A. (2018). Effect of size, morphology, and synthesis method on the thermal and sintering properties of copper nanoparticles for use in microscale additive manufacturing processes. *Additive Manufacturing*, 21, 17-29.

Sadegh, H., Ali, G.A., Gupta, V.K., Makhlouf, A.S.H., Shahryari-ghoshekandi, R., Nadagouda, M.N., Sillanpää, M. & Megiel, E. (2017). The role of nanomaterials as effective adsorbents and their applications in wastewater treatment. *Journal of Nanostructure in Chemistry*, 7(1), 1-14.

Salem, A. N. M., Ahmed, M. A., & El-Shahat, M. F. (2016). Selective adsorption of amaranth dye on Fe_3O_4/MgO nanoparticles. *Journal of Molecular Liquids*, *219*, 780-788.

Salem, S. S., & Fouda, A. (2021). Green synthesis of metallic nanoparticles and their prospective biotechnological applications: an overview. *Biological Trace Element Research*, 199(1), 344-370.

Samer, M. (2015). Biological and chemical wastewater treatment processes. *Wastewater Treatment Engineering*, pp. 1-50.

Shalla, A. H., Bhat, M. A., & Yaseen, Z. (2018). Hydrogels for removal of recalcitrant organic dyes: A conceptual overview. *Journal of Environmental Chemical Engineering*, 6(5), 5938-5949.

Sharma, S., & Bhattacharya, A. (2017). Drinking water contamination and treatment techniques. *Applied Water Science*, 7(3), 1043-1067.

Sherlala, A. I. A., Raman, A. A. A., Bello, M. M., & Asghar, A. (2018). A review of the applications of organo-functionalized magnetic graphene oxide nanocomposites for heavy metal adsorption. *Chemosphere*, *193*, 1004-1017.

Simeon, E. O., Idomo, K. B. S., & Chioma, F. (2019). Physicochemical Characteristics of Surface Water and Sediment of Silver River, Southern Ijaw, Bayelsa State, Niger Delta, Nigeria. *American Journal of Environmental Science and Engineering*, 3(2), 39-46.

Simonazzi, A., Cid, A. G., Villegas, M., Romero, A. I., Palma, S. D., & Bermúdez, J. M. (2018). Nanotechnology applications in drug controlled release. In *Drug Targeting and Stimuli Sensitive Drug Delivery Systems*, (pp. 81-116).

Sivaram, N. M., Gopal, P. M., & Barik, D. (2019). Toxic Waste from Textile Industries. In *Energy from Toxic Organic Waste for Heat and Power Generation*, (Pp. 43-54).

Srivastava, R., & Sofi, I. R. (2020). Impact of Synthetic Dyes on Human Health and Environment. In *Impact of Textile Dyes on Public Health and the Environment* (pp. 146-161). IGI Global.

Stavrinou, A., Aggelopoulos, C. A., & Tsakiroglou, C. D. (2018). Exploring the adsorption mechanisms of cationic and anionic dyes onto agricultural waste peels of banana, cucumber and potato: adsorption kinetics and equilibrium isotherms as a tool. *Journal of Environmental Chemical Engineering*, 6(6), 6958-6970.

Stidworthy, M. F., & Denk, D. (2018). Sphenisciformes, Gaviiformes, Podicipediformes, Procellariiformes, and Pelecaniformes. In *Pathology of Wildlife and Zoo Animals* (pp. 653-686).

Subramani, S. E., & Thinakaran, N. (2017). Isotherm, kinetic and thermodynamic studies on the adsorption behaviour of textile dyes onto chitosan. *Process Safety and Environmental Protection*, *106*, 1-10.

Tahir, M. B., Nabi, G., Rafique, M., & Khalid, N. R. (2017). Nanostructured-based WO_3 photocatalysts: recent development, activity enhancement, perspectives and applications for wastewater treatment. *International Journal of Environmental Science and Technology*, 14(11), 2519-2542.

Taka, A. L., Fosso-Kankeu, E., Pillay, K., & Mbianda, X. Y. (2018). Removal of cobalt and lead ions from wastewater samples using an insoluble nanosponge biopolymer composite: adsorption isotherm, kinetic, thermodynamic, and regeneration studies. *Environmental Science and Pollution Research*, 25(22), 21752-21767.

Thiagarajan, S., Sanmugam, A., & Vikraman, D. (2017). Facile methodology of sol-gel synthesis for metal oxide nanostructures. *Recent Applications in Sol-Gel Synthesis*, IntechOpen, pp. 1-17.

Tijani, J. O., Ugochukwu, O., Fadipe, L. A., Bankole, M. T., Abdulkareem, A. S., & Roos, W. D. (2019). One-step green synthesis of WO_3 nanoparticles using Spondias mombin aqueous extract: effect of solution pH and calcination temperature. *Applied Physics A*, 125(3), 162-173.

Toprak, T., & Anis, P. (2017). Textile industry's environmental effects and approaching cleaner production and sustainability, an overview. *Journal of Textile Engineering and Fashion Technology*, 2(4), 429-442.

Vardhan, K. H., Kumar, P. S., & Panda, R. C. (2019). A review on heavy metal pollution, toxicity and remedial measures: Current trends and future perspectives. *Journal of Molecular Liquids*, *290*, 111197.

Wang, G. (2018). *Nanotechnology: The new features.* Cornell University, pp.1-20

Wang, L., Shi, C., Pan, L., Zhang, X., & Zou, J. J. (2020). Rational design, synthesis, adsorption principles and applications of metal oxide adsorbents: a review. *Nanoscale*, 12(8), 4790-4815.

Wang, M., Gao, B., & Tang, D. (2016). Review of key factors controlling engineered nanoparticle transport in porous media. *Journal of Hazardous Materials*, 318, 233-246.

Weerasooriya, R. R., Liyanage, L. P. K., Rathnappriya, R. H. K., Bandara, W. B. M. A. C., Perera, T. A. N. T., Gunarathna, M. H. J. P., & Jayasinghe, G. Y. (2021). Industrial water conservation by water footprint and sustainable development goals: a review. *Environment, Development and Sustainability*, 1-49.

Welegerima, T. (2018). *Evaluation of Sugarcane Bagasse as Bio Adsorbent In Textile Wastewater Treatment* (Doctoral dissertation, AAU).

World Health Organization, (2007). International Drinking Water Standards, 3rd ed., WHO, Geneva, 2007

World Health Organization. (2020). World malaria report 2020: 20 years of global progress and challenges.

Yang, J., Hou, B., Wang, J., Tian, B., Bi, J., Wang, N., Li, X. & Huang, X. (2019a). Nanomaterials for the removal of heavy metals from wastewater. *Nanomaterials*, 9(3), 424.

Yang, Z., Asoh, T. A., & Uyama, H. (2019b). Removal of cationic or anionic dyes from water using ion exchange cellulose monoliths as adsorbents. *Bulletin of the Chemical Society of Japan*, 92(9), 1453-1461.

Yang, Z., Dai, Z., Yang, Y., Carbonell, J., Salakhutdinov, R. R., & Le, Q. V. (2019). Xlnet: Generalized autoregressive pretraining for language understanding. *Advances in neural information processing systems*, *32*.

Yaseen, D. A., & Scholz, M. (2019). Textile dye wastewater characteristics and constituents of synthetic effluents: a critical review. *International Journal of Environmental Science and Technology*, 16(2), 1193-1226.

Yaya, S., Hudani, A., Udenigwe, O., Shah, V., Ekholuenetale, M., & Bishwajit, G. (2018). Improving water, sanitation and hygiene practices, and housing quality to prevent diarrhea among under-five children in Nigeria. *Tropical medicine and infectious disease*, *3*(2), 41.

Yemmireddy, V. K., & Hung, Y. C. (2017). Using photocatalyst metal oxides as antimicrobial surface coatings to ensure food safety-Opportunities and challenges. *Comprehensive Reviews in Food Science and Food Safety*, 16(4), 617-631.

Zare, K., Gupta, V.K., Moradi, O., Makhlouf, A.S.H., Sillanpää, M., Nadagouda, M.N., Sadegh, H., Shahryari-Ghoshekandi, R., Pal, A., Wang, Z.J. & Tyagi, I. (2015). A comparative study on the basis of adsorption capacity between CNTs and activated carbon as adsorbents for removal of noxious synthetic dyes: a review. *Journal of Nanostructure in Chemistry*, 5(2), 227-236.

Zhou, F., Yan, C., Wang, H., Zhou, S., & Komarneni, S. (2017). Sepiolite-TiO_2 nanocomposites for photocatalysis: Synthesis by microwave hydrothermal treatment versus calcination. *Applied Clay Science*, 146, 246-253.